

Steady-state theory of interdigitated array of electrodes in confined spaces: Case of pure diffusion and reversible electrode reactions

Cristian F. GUAJARDO YÉVENES

Biological Engineering Program and

Pilot Plant Development and Training Institute

King Mongkut's University of Technology Thonburi, Thailand

`cristian.gua@kmutt.ac.th`

Werasak SURAREUNGCHAI

School of Bioresources and Technology and

Nanoscience & Nanotechnology Graduate Program

King Mongkut's University of Technology Thonburi, Thailand

`werasak.sur@kmutt.ac.th`

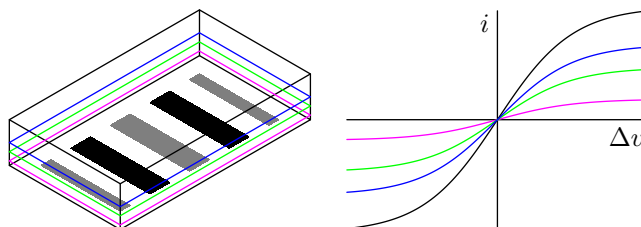
March 6, 2019

Abstract

Analytical equations were found for interdigitated electrodes, which considered reversible electrode reactions and pure diffusion within confined spaces. A conformal transformation, obtained by the use of Jacobian elliptic functions, was applied to solve the diffusion equation in steady state. The obtained steady-state current depends on the ratio of elliptic integrals of the first kind, in which their moduli are functions of the relative dimensions of the cell. The current is smaller for shallower cells, but approaches similar values to those of semi-infinite geometries when the cell is sufficiently tall. Approximations using trigonometric and hyperbolic expressions were also found for the steady-state current in the cases of shallow and tall cells respectively.

Keywords: confined cell, interdigitated array of electrodes, diffusion equation, steady state, voltammogram, current density, limiting current

Graphical abstract



Contents

1	Introduction	4
2	Theory	6
2.1	Definition of the problem	6
2.1.1	Description of the cell	6
2.1.2	Properties of initial and final conditions	7
2.1.3	Properties of boundary conditions	8
2.1.4	Problem reduced to diffusion in the unit cell	8
2.2	Exact solution in steady state	9
2.2.1	Transformation of the unit-cell domain	9
2.2.2	Concentration profile	12
2.2.3	Current density	13
2.2.4	Current per band	15
2.2.5	Voltammogram	15
2.3	Approximations for shallow and tall cells	18
2.3.1	Case of tall cells	20
2.3.2	Case of shallow cells	21
3	Results and discussion	22
3.1	Concentration profile	23
3.2	Current density	24
3.3	Current per band	25
3.3.1	Effect of the counter electrode in the collection efficiency	26
3.3.2	Influence of the cell geometry	26
3.4	Voltammogram shape	28
3.5	Approximations for shallow and tall cells	33
4	Conclusions	35

S1 Additional proofs	S1
S1.1 Transformation of the unit cell domain	S1
S1.1.1 From \mathbf{r} to \mathbf{v} domain	S1
S1.1.2 From \mathbf{v} to $\boldsymbol{\omega}$ domain	S2
S1.1.3 From $\boldsymbol{\omega}$ to $\boldsymbol{\rho}$ domain	S3
S1.1.4 Conformality of the transformation	S3
S1.2 Derivative of the domain transformation	S4
S1.3 Differences of concentrations when using internal counter electrode	S5
S1.3.1 Difference with respect to the average in the unit cell	S5
S1.3.2 Difference with respect to the average in the whole cell	S6
S1.3.3 Limits for the differences of concentration	S6
S1.4 Difference of potential (voltage) when using internal counter electrode	S7
S1.5 Approximations for k_ρ and k'_ρ	S8
S1.5.1 Case of tall cells	S8
S1.5.2 Case of shallow cells	S9
S2 Numerical calculations	S10
S2.1 Simulations in steady state	S10
S2.1.1 Implementation	S10
S2.1.2 Selection of the parameters for the exponential mesh	S11
S2.1.3 Simulation of concentration profile in Fig. 3	S14
S2.1.4 Exhaustive simulations	S18
S2.2 Direct evaluations and curve fitting	S21
S2.2.1 Voltammogram and potentials in Figs. 8a and 8b	S21
S2.2.2 Curve fitting in Fig. 9	S21
S2.2.3 Approximated normalized current in Figs. 10 and 11.	S21

1 Introduction

The use of microelectrodes has been in constant increase since approximately the beginning of 1980 [1–3], mainly due to the development of microfabrication techniques and because of the benefits of microelectrodes towards sensing: reduced ohmic potential drop, fast non-faradaic time constants, shorter diffusion times, fast establishment of steady-state signals and increased signal-to-noise ratio [4, 5].

There are several kinds of microelectrode configurations: disk, cylinder, disk array, microband array¹, interdigitated array², ring and recessed electrodes [4, 6]. Among all these configurations, interdigitated array of electrodes (IDAE) is a popular choice and has drawn great attention, because it can produce high currents from the redox cycling in between closely arranged generators and collectors [5, 6], apart from all the known advantages inherited from microelectrodes.

The use of simple mathematical models allows understanding, prediction of behavior and design of electrode configurations. In this way, the behavior of an IDAE can be prescribed, when its physical implementation is fabricated according to the constraints and assumptions imposed by its mathematical model. Among these models, pure diffusional transport and Nernstian boundary conditions are probably the most used for IDAEs, since they allow great simplifications.

Using this model, simulations have been performed to understand the time dependence of the current generated at IDAE [7]. Also, theoretical results have been obtained in [8–10] by analytically solving the diffusion equation in steady state. From these theoretical results, the work of Aoki stands out, due to the obtention of exact expressions for the current-potential curve and limiting current in steady state for reversible [8] and irreversible [9] electrode reactions.

These theoretical results consider that the IDAE is subject to semi-infinite geometry, that is, they consider that the IDAE is in contact with a large amount of solution around it, so that the diffusion layer is much smaller than the total size of the electrochemical cell. In practical terms, this is equivalent to say that the ratio between the “height of the cell” and the “center-to-center separation between adjacent electrodes” is very large.

This semi-infinite condition is in general not valid for every IDAE electrochemical cell. This can be seen particularly in the case of microfluidic devices, where the height of the microchannel is clearly finite, especially

¹composed of only anodes or only cathodes (all band electrodes at the same potential).

²composed of band electrodes organized as alternating anodes and cathodes.

when using low-cost fabrication techniques: softlithography, transparency-film masks, paper and screen-print to name a few [11–14]. Typical heights of microfluidic channels fabricated using softlithography depend on the thickness of the photoresist molds, which can range between $1\ \mu\text{m}$ to $200\ \mu\text{m}$ [11]. The width and gap of IDAE bands fabricated using photolithography is commonly constrained by the resolution of transparency-film masks, which can range between $20\ \mu\text{m}$ to $50\ \mu\text{m}$ for printers operating between 3380 dpi to 5080 dpi [11, 13]. Therefore, these fabrication techniques can produce microfluidic electrochemical cells where the ratio between “height of the cell” and “center-to-center separation between adjacent electrodes” is clearly finite and ranges between ~ 0.01 to 10. This implies that the equations obtained in [8, 9] may not be always applicable to IDAEs operating within microfluidic channels.

Currently, and due to the lack of analytical expressions for current and current-potential curves, experiments involving IDAE in microchannels are normally contrasted against simulations of its ideal behavior, namely, the diffusion equation subject to Nernstian boundary conditions [15, 16]. Despite this fact, these studies, together with pure experimental [17] and theoretical [18, 19] results, have contributed to reveal the behavior of IDAE in confined spaces with stagnant solutions. These results indicate that higher currents are obtained when using electrochemical cells with taller microchannels. In fact, the current approaches similar values to the case of semi-infinite cells, predicted by [8, 9], when the “height of the microchannel” H is larger than the “center-to-center separation between adjacent electrodes” W . According to [19], finite-height microfluidic cells can be regarded as semi-infinite cells, within 12% error in bulk concentration, when $H/W \gtrsim 1$.

Therefore, this work intends to elucidate the ideal behavior of IDAE in electrochemical cells within confined spaces, and replace the use of simulations, by obtaining analytical expressions for the current and voltammogram as a function of the dimensions of the IDAE and the geometry of the electrochemical cell. This model would enable the design of electrochemical cells that output the maximum current available given microfabrication constraints, and contrast their actual performance with their ideal behavior.

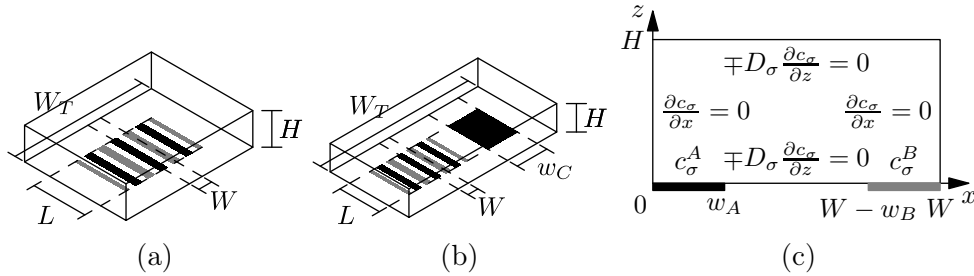


Figure 1: Sketch of an interdigitated array of electrodes (IDAE) in a cell of finite height H and total width W_T . (a) Case of one array used as counter electrode. (b) Case of external counter electrode coplanar to the IDAE. (c) 2D unit cell of height H , width W and half electrode bands A and B . Fig. (a) can be modeled exactly as an assembly of unit cells if the IDAE fits exactly in the cell. Fig. (a) and (b) can be modeled approximately as an assembly of unit cells provided that the number of electrode bands and the length L are large enough.

2 Theory

2.1 Definition of the problem

2.1.1 Description of the cell

Consider an electrochemical cell with an IDAE configuration, as shown in Fig. 1. The cell has a finite height H , total width W_T and it is surrounded by walls which behave as perfect insulators.

The IDAE is located at the floor of the cell and it is composed of two arrays of bands, A (black) and B (gray), of N_A and N_B bands respectively. Each band A and B has respectively a width of $2w_A$ and $2w_B$, a common length L , and they are placed alternately such that two consecutive bands have a center-to-center separation of W . Besides the IDAE, the cell may include a counter electrode C of width w_C and length L , which is assumed to lay on the same plane as the IDAE.

Inside the electrochemical cell there is an oxidated species O and a reduced species R , with diffusion coefficients D_O and D_R respectively. Both species are transported solely by diffusion and react at the surface of the electrodes according to



where n_e corresponds to the number of exchanged electrons. Here it is assumed that the charge transfer on the electrodes follows reversible electrode reactions, and therefore Nernst equation holds even when current flows [20,

Eq. (5:8:6)].

The IDAE is assumed to operate in dual mode, that is, different potentials are applied to each array of bands. If one array is potentiostated and its complementary array performs as counter electrode, then it is said that the IDAE operates with *internal counter electrode*. On the other hand, if both arrays are potentiostated independently, an additional counter electrode would be required, and the IDAE is said to operate with *external counter electrode*.

2.1.2 Properties of initial and final conditions

If the common length L of the electrodes is large enough, then the concentration profile of the electrochemical species σ doesn't change along the depth of the cell, and therefore, it can be reduced to two dimensions $c_\sigma(x, z, t)$. Here x and z are the horizontal and vertical coordinates respectively, and t corresponds to time.

In this case, the concentration profile of species $\sigma \in \{O, R\}$ is given initially by $c_\sigma(x, z, 0^-) = c_{\sigma,i}(x, z)$, and it is assumed to come from a previous steady state. Under this condition, the initial profile has an average (along any horizontal line spanning the whole cell) that is independent of z [19, Remark 2.2]

$$\bar{c}_{\sigma,i}^{\text{whole}} := \frac{1}{W_T} \int_{\text{whole}} c_{\sigma,i}(x, z) dx \quad (2.2a)$$

due to the fact that a coplanar counter electrode is included in the whole cell. Similarly, the weighted sum of initial concentrations is independent of (x, z) [19, Remark 2.1] and equals

$$D_O c_{O,i}(x, z) + D_R c_{R,i}(x, z) = D_O \bar{c}_{O,i}^{\text{whole}} + D_R \bar{c}_{R,i}^{\text{whole}} \quad (2.2b)$$

After the cell is potentiostated, the concentration profile is shifted out from its initial state, entering a new steady state $c_\sigma(x, z, +\infty) = c_{\sigma,f}(x, z)$ after a sufficiently long time compared with the characteristic time of the cell. In this final steady state, the average of concentration (along any horizontal line spanning the whole cell) remains independent of z and equals its initial counterpart $\bar{c}_{\sigma,i}^{\text{whole}}$ [19, Remark 2.2]

$$\frac{1}{W_T} \int_{\text{whole}} c_{\sigma,f}(x, z) dx = \bar{c}_{\sigma,i}^{\text{whole}} \quad (2.3a)$$

due to the fact that the whole cell includes a coplanar counter electrode. Similarly, the weighted sum of concentrations remains independent of (x, z) and equals its initial counterpart [19, Remark 2.1]

$$D_O c_{O,f}(x, z) + D_R c_{R,f}(x, z) = D_O \bar{c}_{O,i}^{\text{whole}} + D_R \bar{c}_{R,i}^{\text{whole}} \quad (2.3b)$$

2.1.3 Properties of boundary conditions

The final concentration $c_{\sigma,f}^E$ of species $\sigma \in \{O, R\}$, at the surface $E \in \{A, B, C\}$ of each band and the external counter electrode (if present), is governed by Nernst equation

$$\eta_f^E := \ln \left(\frac{c_{O,f}^E}{c_{R,f}^E} \right) = \frac{F n_e}{RT} (V_f^E - V^{o'}) \quad (2.4)$$

However, since the weighted sum of concentrations on the surface of E is related to the initial concentrations, due to Eq. (2.3b)

$$D_O c_{O,f}^E + D_R c_{R,f}^E = D_O \bar{c}_{O,i}^{\text{whole}} + D_R \bar{c}_{R,i}^{\text{whole}} \quad (2.5)$$

then the Nernst equation can be decoupled, leading to uniform concentrations on all electrodes $E \in \{A, B, C\}$

$$c_{O,f}^E = \frac{D_O \bar{c}_{O,i}^{\text{whole}} + D_R \bar{c}_{R,i}^{\text{whole}}}{D_O + D_R e^{-\eta_f^E}} = \frac{D_O \bar{c}_{O,i}^{\text{whole}} + D_R \bar{c}_{R,i}^{\text{whole}}}{D_O \bar{c}_{O,i}^{\text{whole}} + D_R \bar{c}_{R,i}^{\text{whole}} e^{-(\eta_f^E - \eta_{\text{null}})}} \bar{c}_{O,i}^{\text{whole}} \quad (2.6a)$$

$$c_{R,f}^E = \frac{D_R \bar{c}_{R,i}^{\text{whole}} + D_O \bar{c}_{O,i}^{\text{whole}}}{D_R + D_O e^{\eta_f^E}} = \frac{D_R \bar{c}_{R,i}^{\text{whole}} + D_O \bar{c}_{O,i}^{\text{whole}}}{D_R \bar{c}_{R,i}^{\text{whole}} + D_O \bar{c}_{O,i}^{\text{whole}} e^{(\eta_f^E - \eta_{\text{null}})}} \bar{c}_{R,i}^{\text{whole}} \quad (2.6b)$$

Here, η_f^E and V_f^E are the normalized and applied potentials at the electrode E in the final steady state, $V^{o'}$ is the formal potential of the redox couple, F is the Faraday constant, R is the universal gas constant and T is the temperature of the system.

Note that if the final concentrations on the electrodes satisfy $c_{\sigma,f}^A = c_{\sigma,f}^B = c_{\sigma,f}^C = \bar{c}_{\sigma,i}^{\text{whole}}$, then there is no gradient of concentration generated inside the cell, and therefore the current in the cell must equal zero. This corresponds to the case when the null potential V_{null} is applied to the electrodes $\eta_f^E = \eta_{\text{null}}$

$$\eta_{\text{null}} = \ln \left(\frac{\bar{c}_{O,i}^{\text{whole}}}{\bar{c}_{R,i}^{\text{whole}}} \right) = \frac{n_e F}{RT} (V_{\text{null}} - V^{o'}) \quad (2.7)$$

2.1.4 Problem reduced to diffusion in the unit cell

If the IDAE fits exactly within the cell, such that the bands at both ends of the IDAE have half width, then the cell in Fig. 1a can be modeled exactly as an assembly of two-dimensional unit cells, like the one shown in Fig. 1c. In case the IDAE doesn't fit exactly in the cell, the configurations in Figs. 1a,b still can be regarded as an assembly of two-dimensional unit cells provided the

following conditions: (i) The length L is large enough, so that the problem still can be reduced to two dimensions. (ii) The number of bands is so large that the edge effects at the ends of the IDAE are negligible, and it is still possible to consider symmetry boundary conditions for the unit cell [8, 271].

Under these conditions, the final concentration $c_{\sigma,f}(x, z)$ of the electrochemical species $\sigma \in \{O, R\}$ can be reduced to a problem of steady-state two-dimensional diffusion³ inside a representative unit cell

$$\frac{\partial^2 c_{\sigma,f}}{\partial x^2}(x, z) + \frac{\partial^2 c_{\sigma,f}}{\partial z^2}(x, z) = 0 \quad (2.8a)$$

$$\frac{\partial c_{\sigma,f}}{\partial x}(0, z) = \frac{\partial c_{\sigma,f}}{\partial x}(W, z) = 0, \forall z \in [0, H] \quad (2.8b)$$

$$\mp D_\sigma \frac{\partial c_{\sigma,f}}{\partial z}(x, H) = 0, \forall x \in [0, W] \quad (2.8c)$$

$$\mp D_\sigma \frac{\partial c_{\sigma,f}}{\partial z}(x, 0) = 0, \forall x \notin A \cup B \quad (2.8d)$$

$$c_{\sigma,f}(x, 0) = c_{\sigma,f}^A, \forall x \in A, \quad (2.8e)$$

$$c_{\sigma,f}(x, 0) = c_{\sigma,f}^B, \forall x \in B \quad (2.8f)$$

where D_σ is the diffusion coefficient of the species $\sigma \in \{O, R\}$, Eqs. (2.8b–2.8d) are symmetry/insulation boundary conditions, and $c_{\sigma,f}^A$ and $c_{\sigma,f}^B$ are the final concentrations at the surface of the bands A and B respectively, see Eqs. (2.6).

2.2 Exact solution in steady state

2.2.1 Transformation of the unit-cell domain

Alternated concentration and insulation boundary conditions at the bottom of the unit cell, Eqs. (2.8d–2.8f), make it difficult to obtain an analytical solution to Eqs. (2.8). Nevertheless, through domain transformations, it is possible to arrange these alternated boundary conditions, so they can be placed at different walls in a transformed cell.

One convenient way to obtain such transformation is through complex conformal mappings, since they leave the diffusion equation (in steady state), as well as the concentration and non-flux/insulation boundary conditions, invariant under domain changes [21, §5.7]. In particular, the complex Jacobian elliptic functions $\text{sn}()$ and $\text{cd}()$ are of interest, since they conformally map a square domain into the upper half-plane [21, §2.5] [22, §22.18.ii]. Also the

³ for \pm or \mp , the upper sign corresponds to $\sigma = O$, and the lower sign, to $\sigma = R$.

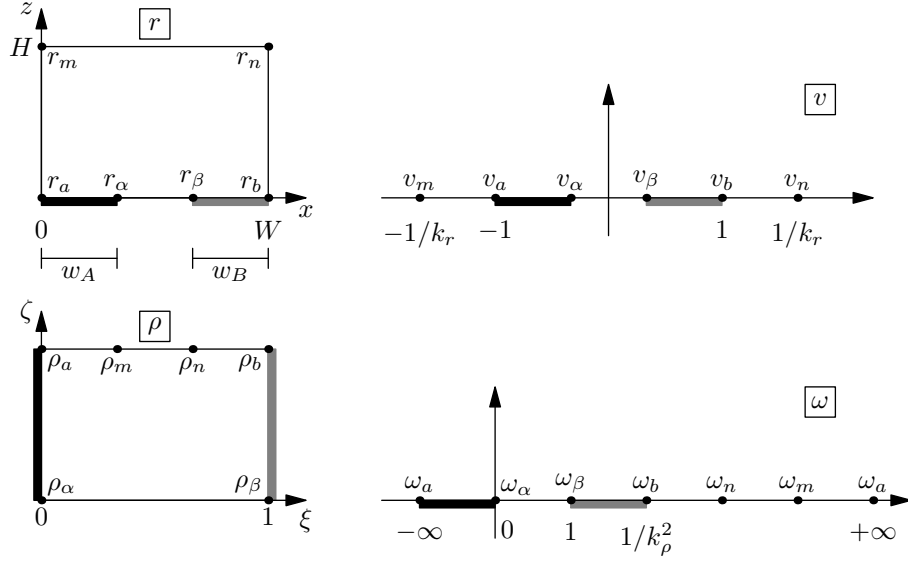


Figure 2: Complex transformation of the IDAE domain $\mathbf{r} = (x, z)$ into the conformal parallel-plates domain $\boldsymbol{\rho} = (\xi, \zeta)$, by using the auxiliary complex domains \mathbf{v} and $\boldsymbol{\omega}$. First, the transformation $\mathbf{r} \rightarrow \mathbf{v}$ maps the interior of the unit cell into the upper half plane by using a Jacobian elliptic function. Later, the transformation $\mathbf{v} \rightarrow \boldsymbol{\omega}$ reorganizes the structure of the upper half plane through a Möbius transformation. Finally, the transformation $\boldsymbol{\omega} \rightarrow \boldsymbol{\rho}$ maps the upper half plane to the interior of the conformal parallel-plates cell, by using a composition of squared root and a inverse Jacobian elliptic function.

Möbius functions are important, since they are able to reorganize the upper half-plane, by mapping into itself [21, §2.3].

One can now regard the concentration $c_{\sigma,f}(x, z)$ as a function $c_{\sigma,f}(\mathbf{r})$ of a complex variable $\mathbf{r} = x + iz$, where $i^2 = -1$, and find a complex function $\boldsymbol{\rho} = T_r^\rho(\mathbf{r})$ that can transform the unit cell from the IDAE domain $\mathbf{r} = x + iz$ to a parallel-plates domain $\boldsymbol{\rho} = \xi + i\zeta$ as shown in Fig. 2.

Lemma 2.1. *The domain $\mathbf{r} = (x, z)$ of the IDAE unit cell can be conformally transformed into a parallel-plates configuration in the domain $\boldsymbol{\rho} = (\xi, \zeta)$, through the use of a complex transformation $\boldsymbol{\rho} = T_r^\rho(\mathbf{r})$ (see*

Fig. 2). This domain transformation is given by

$$\boldsymbol{\rho} = T_r^\rho(\mathbf{r}) = T_\omega^\rho \circ T_v^\omega \circ T_r^v(\mathbf{r}) \quad (2.9a)$$

$$\boldsymbol{\rho} = T_\omega^\rho(\boldsymbol{\omega}) = \frac{1}{K(k_\rho)} \operatorname{arcsn}(\sqrt{\boldsymbol{\omega}}, k_\rho) \quad (2.9b)$$

$$\boldsymbol{\omega} = T_v^\omega(\mathbf{v}) = \frac{(\mathbf{v} - \mathbf{v}_\alpha)(\mathbf{v}_\beta - \mathbf{v}_a)}{(\mathbf{v} - \mathbf{v}_a)(\mathbf{v}_\beta - \mathbf{v}_\alpha)} \quad (2.9c)$$

$$\mathbf{v} = T_r^v(\mathbf{r}) = -\operatorname{cd}\left(K(k_r)\frac{2\mathbf{r}}{W}, k_r\right) \quad (2.9d)$$

where the moduli and their complements are

$$k_\rho^2 = \frac{2(\mathbf{v}_\beta - \mathbf{v}_\alpha)}{(1 - \mathbf{v}_\alpha)(1 + \mathbf{v}_\beta)}, \quad k'_\rho{}^2 = \frac{(1 + \mathbf{v}_\alpha)(1 - \mathbf{v}_\beta)}{(1 - \mathbf{v}_\alpha)(1 + \mathbf{v}_\beta)} \quad (2.10a)$$

$$k_r = Q^{-1}(e^{-\pi 2H/W}), \quad k'_r = Q^{-1}(e^{-\pi W/2H}) \quad (2.10b)$$

and the following points on the boundary of the IDAE domain \mathbf{r}

$$\mathbf{r}_a = (0, 0), \quad \mathbf{r}_\alpha = (w_A, 0) \quad (2.11a)$$

$$\mathbf{r}_b = (W, 0), \quad \mathbf{r}_\beta = (W - w_B, 0) \quad (2.11b)$$

are transformed to the auxiliary domain \mathbf{v} as

$$\mathbf{v}_a = T_r^v(\mathbf{r}_a) = -1, \quad \mathbf{v}_\alpha = T_r^v(\mathbf{r}_\alpha) = -\operatorname{cd}\left(K(k_r)\frac{2w_A}{W}, k_r\right) \quad (2.12a)$$

$$\mathbf{v}_b = T_r^v(\mathbf{r}_b) = 1, \quad \mathbf{v}_\beta = T_r^v(\mathbf{r}_\beta) = \operatorname{cd}\left(K(k_r)\frac{2w_B}{W}, k_r\right) \quad (2.12b)$$

and to the parallel-plates domain $\boldsymbol{\rho}$ as

$$\boldsymbol{\rho}_a = T_r^\rho(\mathbf{r}_a) = \left(0, \frac{K'(k_\rho)}{K(k_\rho)}\right), \quad \boldsymbol{\rho}_\alpha = T_r^\rho(\mathbf{r}_\alpha) = (0, 0) \quad (2.13a)$$

$$\boldsymbol{\rho}_b = T_r^\rho(\mathbf{r}_b) = \left(1, \frac{K'(k_\rho)}{K(k_\rho)}\right), \quad \boldsymbol{\rho}_\beta = T_r^\rho(\mathbf{r}_\beta) = (1, 0) \quad (2.13b)$$

For a detailed construction of this transformation see *Supplementary information* §S1.1.

Several special functions have been used for the definition of the conformal transformation T_r^ρ : $\operatorname{cd}(\mathbf{u}, k)$ and $\operatorname{arcsn}(\mathbf{u}, k)$ correspond to Jacobian elliptic functions [22, Eqs. (22.2.8) and (22.15.12)] analogous to their circu-

lar counterparts $\cos(\cdot)$ and $\arcsin(\cdot)$ respectively, $K(k)$ and $K'(k)$ correspond to the *complete elliptic integral of the first kind* and its associated function respectively [22, Eqs. (19.2.4), (19.2.8) and (19.2.9)], and $Q(k)$ corresponds to the *elliptic nome function* [22, Eq. (22.2.1)].

The conformal transformation in Lemma 2.1 agrees with that in [8, Eqs. (9), (10), (14), (15) and (19)]⁴ for semi-infinite geometries, since $k_r \rightarrow 0^+$, $\text{cd}(\cdot, k_r) \rightarrow \cos(\cdot)$ and $K(k_r) \rightarrow \pi/2$ when $H \rightarrow +\infty$.

2.2.2 Concentration profile

If the concentration profile is now written in terms of the conformal parallel-plates domain $(\xi, \zeta) = T_r^\rho(x, z)$ by using Lema 2.1

$$\gamma_{\sigma,f}(\xi, \zeta) = \gamma_{\sigma,f} \circ T_r^\rho(x, z) = c_{\sigma,f}(x, z) \quad (2.14)$$

then the Laplacian operator in the IDAE and the parallel-plates domains are related [23, §2.1 Problem 7, Eq. (5.4.17)], [21, Eq. (5.20)], [24, Eq. (6.3)]

$$\frac{\partial^2 c_{\sigma,f}}{\partial x^2}(x, z) + \frac{\partial^2 c_{\sigma,f}}{\partial z^2}(x, z) = \left| \frac{\partial \mathbf{r}}{\partial \boldsymbol{\rho}}(\xi, \zeta) \right|^{-2} \left[\frac{\partial^2 \gamma_{\sigma,f}}{\partial \xi^2}(\xi, \zeta) + \frac{\partial^2 \gamma_{\sigma,f}}{\partial \zeta^2}(\xi, \zeta) \right] \quad (2.15)$$

meaning that the diffusion equation in steady state is invariant under conformal domain transformations. The same is true for insulation/symmetry boundary conditions, that is, they remain invariant under conformal transformations, since the angles between the iso-concentration lines and the flux lines are preserved.

Therefore, the steady-state diffusion problem in Eqs. (2.8) is transformed to the conformal parallel-plates domain $\boldsymbol{\rho} = (\xi, \zeta)$

$$\frac{\partial^2 \gamma_{\sigma,f}}{\partial \xi^2}(\xi, \zeta) + \frac{\partial^2 \gamma_{\sigma,f}}{\partial \zeta^2}(\xi, \zeta) = 0 \quad (2.16a)$$

$$\frac{\partial \gamma_{\sigma,f}}{\partial \zeta}(\xi, 0) = \frac{\partial \gamma_{\sigma,f}}{\partial \zeta}(\xi, \zeta_a) = 0 \quad (2.16b)$$

$$\gamma_{\sigma,f}(0, \zeta) = c_{\sigma,f}^A \quad (2.16c)$$

$$\gamma_{\sigma,f}(1, \zeta) = c_{\sigma,f}^B \quad (2.16d)$$

where $\zeta_a = \Im \boldsymbol{\rho}_a = K'(k_\rho)/K(k_\rho)$ corresponds to the imaginary part of $\boldsymbol{\rho}_a$ defined in Eq. (2.13). This leads to the following solution for the concentration profile in steady state

⁴ Note that in [8] the parameter $p = k_\rho^2$ is used instead of the modulus k_ρ .

Theorem 2.1. *If the IDAE can be modeled as an assembly of unit cells and the final concentrations on the bands A and B are uniform, such as in §2.1, then the concentration profile in the final steady state is given by*

$$c_{\sigma,f}(x, z) = c_{\sigma,f}^A + [c_{\sigma,f}^B - c_{\sigma,f}^A]\xi(x, z) \quad (2.17)$$

where $c_{\sigma,f}^E$ is the steady-state concentration of the species $\sigma \in \{O, R\}$ on each band $E \in \{A, B\}$, defined in Eq. (2.6), and $\xi(x, z) = \Re T_r^\rho(x, z)$ corresponds to the real part of the conformal transformation $T_r^\rho(x, z)$, defined in Eq. (2.9).

Proof. Due to the symmetry boundary conditions in Eq. (2.16b), the parallel-plates cell can be extended infinitely along the ζ -axis. The concentration profile $\gamma_{\sigma,f}(\xi, \zeta)$ for the infinite parallel-plates cell doesn't depend on the ζ -coordinate, therefore the steady-state solution of Eq. (2.16) is given by a linear interpolation of the concentration at each of the plates

$$\gamma_{\sigma,f}(\xi, \zeta) = c_{\sigma,f}^A + [c_{\sigma,f}^B - c_{\sigma,f}^A]\xi \quad (2.18)$$

The desired result is finally obtained by applying the conformal transformation $(\xi, \zeta) = T_r^\rho(x, z)$ in Lema 2.1 to return to the IDAE domain. *QED.*

Note that the expression for the concentration profile given by Eqs. (2.17) and (2.6) agrees with that in [8, Eqs. (20) and (21)]⁵ for semi-infinite geometries, which depends directly on the real part of the conformal transformation T_r^ρ in Lemma 2.1.

2.2.3 Current density

Corollary 2.1. *Under the conditions of Theorem 2.1, the current density $j_f(x)$ in the final steady state is given by*

$$\mp \frac{j_f(x)}{Fn_e D_\sigma [c_{\sigma,f}^B - c_{\sigma,f}^A]} = \frac{\partial \xi}{\partial z}(x, 0) = -\Im \frac{\partial \rho}{\partial \mathbf{r}}(x) \quad (2.19)$$

where $\Im\{\}$ corresponds to the imaginary part and the complex deriva-

⁵ Note that [8, H in Eq. (21)] has a typo, and the $+$ sign, at the middle of the expression, should be replaced by a $-$ sign.

tive of $\boldsymbol{\rho} = T_r^\rho(\mathbf{r})$ is given by

$$\frac{\partial \boldsymbol{\rho}}{\partial \mathbf{r}}(\mathbf{r}) = \mathbf{i} \frac{k'_r}{W} \frac{K(k_r)}{K(k_\rho)} \frac{(1 - \mathbf{v}_\alpha)^{1/2} (1 + \mathbf{v}_\beta)^{1/2}}{(\mathbf{v} - \mathbf{v}_\alpha)^{1/2} (\mathbf{v} - \mathbf{v}_\beta)^{1/2}} \text{nd} \left(K(k_r) \frac{2\mathbf{r}}{W}, k_r \right) \quad (2.20)$$

of which its parameters are defined in Eqs. (2.10) and (2.12), and $\text{nd}(\cdot)$ corresponds to a Jacobian elliptic function, defined in [22, Eq. (22.2.6)].

Proof. Applying Fick's law to Eq. (2.17) leads to

$$j_f(x) = \mp F n_e D_\sigma \frac{\partial c_{\sigma,f}}{\partial z}(x, 0) = \mp F n_e D_\sigma [c_{\sigma,f}^B - c_{\sigma,f}^A] \frac{\partial \xi}{\partial z}(x, 0) \quad (2.21)$$

Later, using the Cauchy-Riemann equations [24, Theorem 3.2]

$$\frac{\partial \xi}{\partial z} = -\frac{\partial \zeta}{\partial x} = -\Im \frac{\partial \boldsymbol{\rho}}{\partial x} = -\Im \frac{\partial \boldsymbol{\rho}}{\partial \mathbf{r}} \quad (2.22)$$

leads to Eq. (2.19), which ends the main proof. The rest of the proof concerns about obtaining the complex derivative of T_r^ρ in Eq. (2.20), which is detailed in *Supplementary information* §S1.2. *QED.*

The expression for the current density in Eq. (2.19) agrees with that in [8, Eqs. (26) and (19)] for semi-infinite geometries. Both results depend directly on the imaginary part of the complex derivative $\partial \boldsymbol{\rho}(x)/\partial \mathbf{r}$ and the product [8, $c^* H$ given by Eqs. (6) and (21)]⁶ corresponds to $[c_{\sigma,f}^B - c_{\sigma,f}^A]$.

The expression for $\Im \partial \boldsymbol{\rho}(x)/\partial \mathbf{r}$ in Eq. (2.20) also agrees with that in [8, Eqs. (27) and (17)] for semi-infinite geometries, which can be seen with the help of the identity

$$\cos(\alpha + \beta) + \cos(\alpha - \beta) = (1 + \cos(2\alpha))^{1/2} (1 + \cos(2\beta))^{1/2} \quad (2.23)$$

and because $k_r \rightarrow 0^+$, $k'_r \rightarrow 1^-$, $K(k_r) \rightarrow \pi/2$, $\text{cd}(\cdot, k_r) \rightarrow \cos(\cdot)$, $\text{nd}(\cdot, k_r) \rightarrow 1$, when $H \rightarrow +\infty$.

⁶ Note that [8, H in Eq. (21)] has a typo, and the + sign, at the middle of the expression, should be replaced by a - sign.

2.2.4 Current per band

Corollary 2.2. *Under the conditions of Theorem 2.1, the current in the final steady state i_f^E flowing through one band $E \in \{A, B\}$ is*

$$\pm \frac{i_f^A/L}{Fn_e D_\sigma [c_{\sigma,f}^A - c_{\sigma,f}^B]} = \pm \frac{i_f^B/L}{Fn_e D_\sigma [c_{\sigma,f}^B - c_{\sigma,f}^A]} = 2 \frac{K'(k_\rho)}{K(k_\rho)} \quad (2.24)$$

where the modulus k_ρ and its complement k'_ρ are defined in Eq. (2.10a).

Proof. The current i_f^E can be obtained by integrating the flux through one band $E \in \{A, B\}$

$$i_f^E = \mp \int_E Fn_e D_\sigma \frac{\partial c_{\sigma,f}}{\partial z}(x, 0) L dx = \mp \int_E Fn_e D_\sigma [c_{\sigma,f}^B - c_{\sigma,f}^A] \frac{\partial \xi}{\partial z}(x, 0) L dx \quad (2.25)$$

Using the Cauchy-Riemann identities in Eq. (2.22) the current can be further simplified

$$\mp \frac{i_f^E/L}{Fn_e D_\sigma [c_{\sigma,f}^B - c_{\sigma,f}^A]} = \int_E \frac{\partial \xi}{\partial z}(x, 0) dx = -\Im \int_E \frac{\partial \rho}{\partial x}(x, 0) dx = -\Im \int_E \partial \rho(\mathbf{r}) \quad (2.26)$$

Due to symmetry this integral can be taken in a half band

$$-\Im \int_A \partial \rho(\mathbf{r}) = -2 \Im \rho(\mathbf{r}) \Big|_{r_a}^{r_\alpha}, \quad -\Im \int_B \partial \rho(\mathbf{r}) = -2 \Im \rho(\mathbf{r}) \Big|_{r_\beta}^{r_b} \quad (2.27)$$

Since $\rho = T_r^\rho(\mathbf{r})$ and due to Eq. (2.13), the result in Eq. (2.24) can be obtained. *QED.*

Note that Eq. (2.24) agrees with the result in [8, Eqs. (28)]⁷ for semi-infinite geometries, where the product [8, c^*H given by Eqs. (6) and (21)]⁸ corresponds to $[c_{\sigma,f}^B - c_{\sigma,f}^A]$.

2.2.5 Voltammogram

The voltammogram in steady state corresponds just to the expression of current, obtained in Eq. (2.24), as the potential applied to the bands is

⁷ Note that in [8] the parameter $p = k_\rho^2$ is used instead of the modulus k_ρ .

⁸ Note that [8, H in Eq. (21)] has a typo, and the + sign, at the middle of the expression, should be replaced by a - sign.

scanned. During the scan, all parameters of the expression for the current remain unchanged, except for the difference of concentrations $c_{\sigma,f}^A - c_{\sigma,f}^B$, which varies according to the potential due to Eqs. (2.6).

Therefore, the shape of the voltammogram is proportional to the shape of $c_{\sigma,f}^A - c_{\sigma,f}^B$ as the potential is scanned. This difference is analyzed in two cases: when the IDAE has an external and an internal counter electrode.

Case of external counter electrode This case is the simplest to analyze, but its experimental setup is relatively complex, since it requires a bipotentiostat connected to the IDAE and an external counter electrode.

Theorem 2.2. *Consider the electrodes A and B with an external counter electrode, which undergo reversible electrode reactions and satisfy Eq. (2.5) (like in §2.1 with Fig. 1b). If the potential at $E \in \{A, B\}$ is scanned and its complementary electrode E' is fixed to an extreme potential, such that $c_{\sigma,f}^{E'} = 0$, then the difference of final concentrations is given by*

$$[c_{\sigma,f}^E - c_{\sigma,f}^{E'}] = c_{\sigma,f}^E = \frac{D_{\sigma} \bar{c}_{\sigma,i}^{whole} + D_{\sigma'} \bar{c}_{\sigma',i}^{whole}}{D_{\sigma} \bar{c}_{\sigma,i}^{whole} + D_{\sigma'} \bar{c}_{\sigma',i}^{whole} e^{\mp(\eta_f^E - \eta_{null})}} \bar{c}_{\sigma,i}^{whole} \quad (2.28)$$

where σ' is the complementary redox species of $\sigma \in \{O, R\}$, $D_{\sigma'}$ and D_{σ} are their diffusion coefficients, $\bar{c}_{\sigma,i}^{whole}$ and $\bar{c}_{\sigma',i}^{whole}$ are the average concentrations of the whole cell in the initial steady state, η_f^E is the normalized potential applied to E, defined in Eq. (2.4), and η_{null} is the normalized null potential in Eq. (2.7).

Proof. Eq. (2.28) is obtained directly from Eq. (2.6), when $c_{\sigma,f}^{E'} = 0$. *QED.*

Case of internal counter electrode In this case the experimental setup is simpler, since it requires a conventional potentiostat connected to both arrays of the IDAE. Moreover, when the internal counter electrode serves as reference, no potentiostat would be necessary and a voltage source with a sensitive ammeter would suffice as instrumentation [25, end of p. 33].

However, the analysis is not direct, since the potential at the counter electrode bands is controlled automatically by the potentiostat, and therefore it is unknown before performing the experiment. Moreover, when the internal counter electrode acts as reference, even the potential at the working electrode is unknown and only the voltage (difference of potential) between

working and counter electrodes would be known.

One solution is to consider the case of bands of equal width $2w_A = 2w_B$. Here the average in Eq. (2.3a) is reduced to $\bar{c}_{\sigma,i}^{\text{whole}} = (c_{\sigma,f}^A + c_{\sigma,f}^B)/2$ [10, Eq. (15)], due to symmetry, or equivalently

$$[c_{\sigma,f}^A - \bar{c}_{\sigma,i}^{\text{whole}}] = -[c_{\sigma,f}^B - \bar{c}_{\sigma,i}^{\text{whole}}] \quad (2.29)$$

This allows an *a priori* estimation of the concentration at the counter electrode bands. However, this also restricts the magnitude of the concentrations on the bands, since they must be non-negative, and therefore, they cannot decrease indefinitely below the average $\bar{c}_{\sigma,i}^{\text{whole}}$

$$-D_\sigma \bar{c}_{\sigma,i}^{\text{whole}} \leq D_\sigma [c_{\sigma,f}^A - \bar{c}_{\sigma,i}^{\text{whole}}] = -D_\sigma [c_{\sigma,f}^B - \bar{c}_{\sigma,i}^{\text{whole}}] \leq D_\sigma \bar{c}_{\sigma,i}^{\text{whole}} \quad (2.30)$$

Due to Eq. (2.3b), a similar situation occurs with the complementary species, and has been graphically illustrated in [19, Fig. 2].

Lemma 2.2. *Consider the electrodes A and B, which undergo reversible electrode reactions and satisfy Eqs. (2.5) and (2.29) (like in §2.1 with Fig. 1a and bands of equal width). If the electrode $E \in \{A, B\}$ and its complementary electrode E' perform as working and counter electrodes respectively, then the difference of final concentrations of species $\sigma \in \{O, R\}$ is given by*

$$[c_{\sigma,f}^E - c_{\sigma,f}^{E'}] = 2[c_{\sigma,f}^E - \bar{c}_{\sigma,i}^{\text{whole}}] = -2[c_{\sigma,f}^{E'} - \bar{c}_{\sigma,i}^{\text{whole}}] \quad (2.31)$$

Nevertheless, this difference cannot reach its ideal maximum, obtainable from Eq. (2.34a), being limited from above and below by

$$-2D_\lambda \bar{c}_{\lambda,i}^{\text{whole}} \leq D_\sigma [c_{\sigma,f}^E - c_{\sigma,f}^{E'}] \leq 2D_\lambda \bar{c}_{\lambda,i}^{\text{whole}} \quad (2.32)$$

where the limiting species $\lambda \in \{O, R\}$ is such that $D_\lambda \bar{c}_{\lambda,i}^{\text{whole}} = \min(D_O \bar{c}_{O,i}^{\text{whole}}, D_R \bar{c}_{R,i}^{\text{whole}})$. This last expression determines the limiting current of the cell.

See *Supplementary information* §S1.3 for a detailed proof.

Remark 2.1. *Note that, in the case of external counter electrode, the difference of concentrations is bounded by*

$$0 \leq D_\sigma [c_{\sigma,f}^E - c_{\sigma,f}^{E'}] \leq D_\sigma \bar{c}_{\sigma,f}^{\text{whole}} + D_{\sigma'} \bar{c}_{\sigma',f}^{\text{whole}} \quad (2.33)$$

due to Eq. (2.28) when $\eta_f^E \rightarrow \pm\infty$. This determines the limiting current in the case of external counter electrode.

The result in Lemma 2.2 allows us to estimate the unknown concentration on the counter electrode, thus facilitating an analytical expression for the voltammogram

Theorem 2.3. *Under the assumptions of Lemma 2.2, the difference of concentrations (voltammogram) in terms of the normalized potential is given by*

$$[c_{\sigma,f}^E - c_{\sigma,f}^{E'}] = \frac{D_{\sigma'} \bar{c}_{\sigma',i}^{whole} - D_{\sigma'} \bar{c}_{\sigma',i}^{whole} e^{\mp(\eta_f^E - \eta_{null})}}{D_{\sigma} \bar{c}_{\sigma,i}^{whole} + D_{\sigma'} \bar{c}_{\sigma',i}^{whole} e^{\mp(\eta_f^E - \eta_{null})}} \cdot 2\bar{c}_{\sigma,i}^{whole} \quad (2.34a)$$

or in terms of the normalized voltage

$$\begin{aligned} \pm(\eta_f^E - \eta_f^{E'}) &= 2 \operatorname{arctanh} \left(\frac{c_{\sigma,f}^E - c_{\sigma,f}^{E'}}{2\bar{c}_{\sigma,i}^{whole}} \right) \\ &+ 2 \operatorname{arctanh} \left(\frac{D_{\sigma} \bar{c}_{\sigma,i}^{whole}}{D_{\sigma'} \bar{c}_{\sigma',i}^{whole}} \cdot \frac{c_{\sigma,f}^E - c_{\sigma,f}^{E'}}{2\bar{c}_{\sigma,i}^{whole}} \right) \end{aligned} \quad (2.34b)$$

where σ' is the complementary redox species of σ , $D_{\sigma'}$ and D_{σ} are their diffusion coefficients, $\bar{c}_{\sigma,i}^{whole}$ and $\bar{c}_{\sigma',i}^{whole}$ are the average concentrations of the whole cell in the initial steady state, η_f^E and $\eta_f^{E'}$ are the normalized potentials applied to the electrodes E and E' , given in Eq. (2.4), and η_{null} is the normalized null potential in Eq. (2.7).

Proof. Eq. (2.34a) is obtained when subtracting Eq. (2.6) with $\bar{c}_{\sigma,i}^{whole}$, and later by applying $[c_{\sigma,f}^E - c_{\sigma,f}^{E'}] = 2[c_{\sigma,f}^E - \bar{c}_{\sigma,f}^{whole}]$. The proof for Eq. (2.34b) can be found in *Supplementary information* §S1.4. *QED.*

2.3 Approximations for shallow and tall cells

For calculating the steady-state current through the cell, one must evaluate the ratio $K'(k_\rho)/K(k_\rho)$ in Eq. (2.24), which depends on several elliptic functions as seen in Eqs. (2.10) and (2.12). Currently, commercial and *free and open source software* (FOSS) are available to aid in such calculations:

Mathematica, Sage and SciPy⁹ to name a few examples [22, §22.22]. However, standard scientific calculators and standard office software (with MS Office and LibreOffice as common examples) are not able to compute such special functions, and therefore, approximations using trigonometric/hyperbolic functions are needed.

One convenient way to find such approximations is by using the *nome function* $q = Q(k)$ [26, §VI.3 Eq. (16)], [22, Eqs. (19.2.9) and (22.2.1)]

$$\frac{\ln Q(k)}{-\pi} = \frac{-\pi}{\ln Q(k')} = \frac{K'(k)}{K(k)} \quad (2.35)$$

as a way to compute the ratio¹⁰ $K'(k)/K(k)$. This is because the Taylor expansion of the nome function $Q(k)$ is known and converges relatively fast [27, below Eq. (12)] [22, Eq. (19.5.5)]

$$Q(k) = \frac{k^2}{16} + 8 \left(\frac{k^2}{16}\right)^2 + 84 \left(\frac{k^2}{16}\right)^3 + 992 \left(\frac{k^2}{16}\right)^4 + O(k^{10}) \quad (2.36)$$

Therefore, for a sufficiently small modulus k or k' , the ratio $K'(k)/K(k)$ can be approximated with enough accuracy by using only the first term of the previous series

$$\left. \frac{K'(k)}{K(k)} \right|_{k \approx 0} = -\frac{1}{\pi} \ln Q(k) \Big|_{k \approx 0} \approx -\frac{1}{\pi} \ln \left(\frac{k^2}{16}\right) \quad (2.37a)$$

$$\left. \frac{K'(k)}{K(k)} \right|_{k' \approx 0} = -\pi [\ln Q(k')]^{-1} \Big|_{k' \approx 0} \approx -\pi \left[\ln \left(\frac{k'^2}{16}\right) \right]^{-1} \quad (2.37b)$$

Also the following alternative representations of the moduli k_ρ and k'_ρ are useful for finding the desired approximations

Lemma 2.3. *The modulus k_ρ and the complementary modulus k'_ρ have alternative representations to those given in Eq. (2.10a). For k_ρ the proposed alternative representation depends on the gap between consecutive bands $g = W - 2w_E$, when the width of both electrode bands is*

⁹ Jacobian elliptic functions, the nome function and their inverses are available through the library `mpmath`

¹⁰ this ratio is closely related to the *lattice parameter* $\tau = iK'(k)/K(k)$ and the *nome* $q = \exp(i\pi\tau)$ [22, §20.1, §22.1, and Eqs. (22.2.1) and (22.2.12)].

equal $2w_E = 2w_A = 2w_B$

$$k_\rho^2 = \frac{4 \operatorname{sn}\left(K(k_r) \frac{g}{W}, k_r\right)}{\left[1 + \operatorname{sn}\left(K(k_r) \frac{g}{W}, k_r\right)\right]^2} \quad (2.38)$$

For k'_ρ the proposed alternative representation is given directly by

$$k'^2_\rho = k'^4_r \frac{\operatorname{sd}\left(K(k_r) \frac{w_A}{W}, k_r\right)^2 \operatorname{sd}\left(K(k_r) \frac{w_B}{W}, k_r\right)^2}{\operatorname{cn}\left(K(k_r) \frac{w_A}{W}, k_r\right)^2 \operatorname{cn}\left(K(k_r) \frac{w_B}{W}, k_r\right)^2} \quad (2.39)$$

Proof. Eq. (2.38) is obtained from Eqs. (2.10a) and (2.12) when $2w_A = 2w_B = 2w_E$, later substituting $\operatorname{cd}()$ by $\operatorname{sn}()$

$$\operatorname{cd}(\mathbf{u}, k) = \operatorname{sn}(\mathbf{u} - K(k) + 2K(k), k) = \operatorname{sn}(K(k) - \mathbf{u}) \quad (2.40)$$

(which is obtained from translation by quarter/half period [22, Table 22.4.3] and $\operatorname{sn}(-\mathbf{z}, k) = -\operatorname{sn}(\mathbf{z}, k)$ [22, Table 22.6.1]) and finally by substituting $2w_E = W - g$.

Similarly, Eq. (2.39) is obtained from Eqs. (2.10a) and (2.12), and later using the identity [28, Eqs. (1.10) and (4.1)]

$$\frac{1 - \operatorname{cd}(2\mathbf{u}, k)}{1 + \operatorname{cd}(2\mathbf{u}, k)} = k'^2 \frac{\operatorname{sd}(\mathbf{u}, k)^2}{\operatorname{cn}(\mathbf{u}, k)^2} \quad (2.41)$$

QED.

The last step remaining is to find trigonometric/hyperbolic approximations of the moduli k_ρ and k'_ρ , so they can be plugged into Eqs. (2.37). This is shown below for the case of tall electrochemical cells with small and large electrode bands.

2.3.1 Case of tall cells

In this case, the Jacobian elliptic functions $\operatorname{sn}()$ and $\operatorname{sd}()$ in Lemma 2.3 can be approximated by their trigonometric counterpart $\sin()$. In the same manner, $\operatorname{cn}()$ can be approximated by $\cos()$. See [22, Eqs. (22.10.4)–(22.10.6)] or [29, Eqs. (10.1)–(10.3)].

Theorem 2.4. *In case of tall electrochemical cells (H is large), the modulus k_ρ and the complementary modulus k'_ρ are given by*

$$k_\rho^2 \Big|_{\substack{H \rightarrow +\infty \\ g \approx 0}} = \frac{4 \sin(\pi g/2W)}{[1 + \sin(\pi g/2W)]^2} \approx 4 \left(\frac{\pi g}{2W} \right) \quad (2.42a)$$

$$k'_\rho^2 \Big|_{\substack{H \rightarrow +\infty \\ 2w_A \approx 0 \\ 2w_B \approx 0}} = \tan\left(\frac{\pi w_A}{2W}\right)^2 \tan\left(\frac{\pi w_B}{2W}\right)^2 \approx \left(\frac{\pi w_A}{2W}\right)^2 \left(\frac{\pi w_B}{2W}\right)^2 \quad (2.42b)$$

Therefore, the ratio $K'(k_\rho)/K(k_\rho)$ for large and small electrodes is given respectively by

$$\frac{K'(k_\rho)}{K(k_\rho)} \Big|_{\substack{H \rightarrow +\infty \\ g \approx 0}} \approx -\frac{1}{\pi} \ln\left(\frac{\pi g}{8W}\right) \quad (2.43a)$$

$$\frac{K'(k_\rho)}{K(k_\rho)} \Big|_{\substack{H \rightarrow +\infty \\ 2w_A \approx 0 \\ 2w_B \approx 0}} \approx -\pi \left[2 \ln\left(\frac{\pi w_A}{4W}\right) + 2 \ln\left(\frac{\pi w_B}{4W}\right) \right]^{-1} \quad (2.43b)$$

Here $g = W - 2w_E$ corresponds to the gap between consecutive bands, when they have equal width $2w_E = 2w_A = 2w_B$.

The results in Eqs. (2.42a) and (2.43a) were first obtained by [8, Eq. (32)], for the case of large electrodes. Almost two decades later, Eqs. (2.42b) and (2.43b) were obtained by [10, Eqs. (2), (6) and (7)], for the case of small electrodes. See *Supplementary information* §S1.5.1 for a proof of both results. Also see Table 1 in *Results and discussion* §3.5 to know the width of the electrode bands for which the approximations hold.

2.3.2 Case of shallow cells

Similarly, hyperbolic approximations [29, Eqs. (11.1)–(11.3)] of Jacobian elliptic functions in Lemma 2.3 can be used for shallow electrochemical cells with small and large electrode bands.

Theorem 2.5. *In case of shallow electrochemical cells (H is small),*

the modulus k_ρ and the complementary modulus k'_ρ are given by

$$k_\rho^2 \Big|_{\substack{H \approx 0 \\ g \approx 0}} \approx 4 \coth\left(\frac{\pi W}{4 H} - \ln \sqrt{2}\right) \tanh\left(\frac{\pi g}{4 W} \frac{W}{H}\right) \quad (2.44a)$$

$$k'_\rho^2 \Big|_{H \approx 0} \approx 16 e^{-\pi W/H} \sinh\left(\frac{\pi w_A}{2} \frac{W}{H}\right)^2 \sinh\left(\frac{\pi w_B}{2} \frac{W}{H}\right)^2 \quad (2.44b)$$

Therefore, the normalized current in Eq. (2.24) for large and small electrodes is given respectively by

$$\frac{K'(k_\rho)}{K(k_\rho)} \Big|_{\substack{H \approx 0 \\ g \approx 0}} \approx -\frac{1}{\pi} \left[\ln \tanh\left(\frac{\pi g}{4 H}\right) - \ln \tanh\left(\frac{\pi W}{4 H} - \ln \sqrt{2}\right) - \ln 4 \right] \quad (2.45a)$$

$$\frac{K'(k_\rho)}{K(k_\rho)} \Big|_{\substack{H \approx 0 \\ 2w_A \approx 0 \\ 2w_B \approx 0}} \approx -\pi \left[2 \ln \sinh\left(\frac{\pi w_A}{2} \frac{W}{H}\right) + 2 \ln \sinh\left(\frac{\pi w_B}{2} \frac{W}{H}\right) - \pi \frac{W}{H} \right]^{-1} \quad (2.45b)$$

Here the gap between consecutive bands equals $g = W - 2w$, when they have equal width $2w = 2w_A = 2w_B$.

See *Supplementary information* §S1.5.2 for a proof. Also see Table 1 in *Results and discussion* §3.5 to know the cell dimensions for which the approximations hold.

3 Results and discussion

The scripts¹¹ for obtaining the plots and simulations in this section were written in Python using the SciPy stack [30]. In particular, Jacobian elliptic functions (required for plotting the theoretical concentration profile, current density and current) were obtained from the library `mpmath` [31]. The simulations of the concentration profile and current were computed using the finite element library `FiPy` [32].

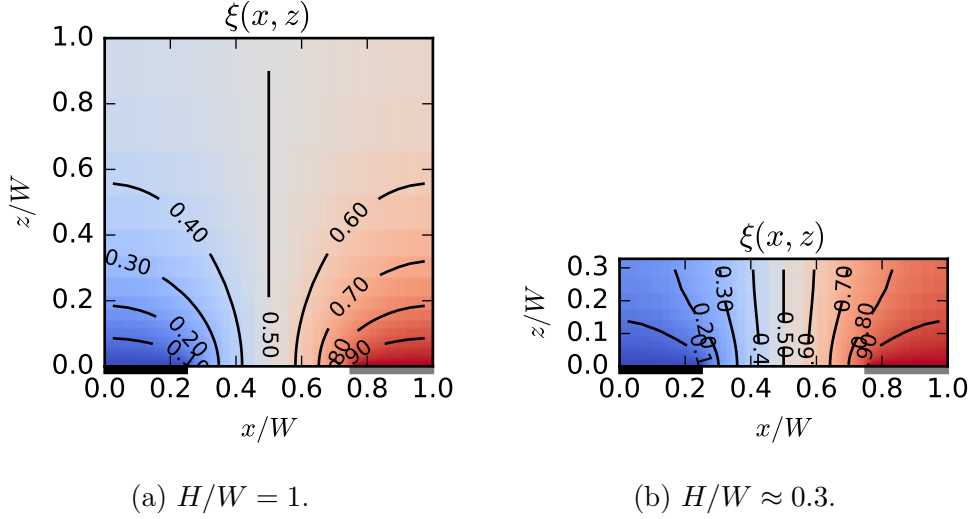


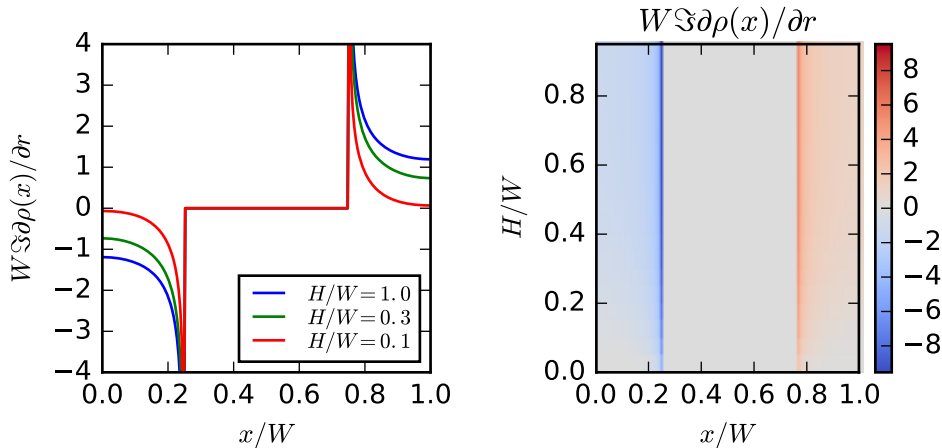
Figure 3: Normalized concentration $\xi(x, z) = [c_{\sigma,f}(x, z) - c_{\sigma,f}^A]/[c_{\sigma,f}^B - c_{\sigma,f}^A]$ in the final steady state Eq. (2.17) (iso-concentration lines shown in black). Plots consider electrodes of equal size $2w_A = 2w_B = 0.5W$ and different aspect ratios H/W for the unit cell. The absolute error between theoretical concentration and its simulated counterpart was not greater than ≈ 0.003 for this two cases. (See *Supplementary information* §S2.1.3 for error plots).

3.1 Concentration profile

The concentration profile in Eq. (2.17) was contrasted against simulations of Eqs. (2.8) for different values of aspect ratio $H/W \in]0, 1.25[$ and electrode widths $2w_A/W = 2w_B/W \in]0, 1[$. In 43 of 45 analyzed cases, the maximum absolute error was not greater than ≈ 0.0045 (which corresponds to two decimal places of accuracy), confirming the correctness of the expression obtained in Eq. (2.17). See Table S2 in *Supplementary information* §S2.1.4 for more details.

Fig. 3 shows the behavior of the concentration profile under the cases of high and low aspect ratios H/W (simulation errors and other details are shown in *Supplementary information* §S2.1.3). In case of high aspect ratio H/W (Fig. 3a), the concentration becomes uniform far from the surface of the electrodes (near the roof of the cell) and full radial diffusion is present, thus mimicking the behavior of semi-infinite configurations [18, Figs. 6 and 9] [33, p. 6406 and Fig. S3] [34, Fig. 39] [16, 309]. Moreover, according to [19, Theorem 2.6], $H/W \gtrsim 1$ corresponds to the condition under which

¹¹All python scripts are available online at <https://gitlab.com/cfgy/elektrodo/tree/p2019mar>.



(a) Selected values of H/W . (b) Range of values $H/W \in [0, 1]$.

Figure 4: Plots of the normalized current density $W\mathfrak{S}\partial\rho(x)/\partial r = \pm Wj_f(x)/(Fn_eD_\sigma[c_{\sigma,f}^B - c_{\sigma,f}^A])$ in Eq. (2.19) for electrode bands of equal width $2w_A = 2w_B = 0.5W$ and different values of H/W .

the concentration of a finite-height cell and its semi-infinite counterpart have similar profiles, which agrees with Fig. 3a.

In the case of low aspect ratio H/W (Figs. 3b), the concentration profile doesn't exhibit a region of uniform concentration, and radial diffusion is truncated by the low roof of the cell. Similar results obtained in [18, Fig. 6] [19, §3.2] [33, p.6406, Fig. S3] [34, Fig. 39] [16, p.309] confirm these facts. Moreover, when the aspect ratio is low enough (compare supplementary Figs. S3b and S3c), the vertical gradient of concentration is almost inexistent, being the horizontal gradient the only one that is clearly appreciable, which resembles that of a parallel-plates configuration in the gap between consecutive electrode bands.

3.2 Current density

The aspect ratio of the unit cell also affects the shape of the current density on the IDAE.

Fig. 4 shows the normalized current density, at the bottom of the unit cell, for different aspect ratios H/W , when the width of the electrode bands equals $2w_A = 2w_B = 0.5W$. As predicted by Eq. (2.20), the current density becomes singular at the edges of the electrode bands. Also, it can be seen that the current density is highly non-uniform near the edges, and becomes approximately uniform near the center of the electrode bands.

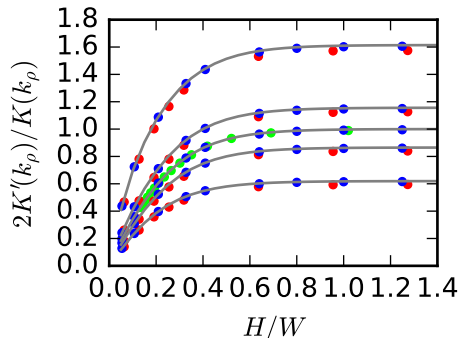


Figure 5: Comparison between simulated and theoretical normalized current per band $2K'(k_\rho)/K(k_\rho) = \pm(i_f^E/L)/(Fn_eD_\sigma[c_{\sigma,f}^E - c_{\sigma,f}^{E'}])$ for $2w_A/W = 2w_B/W \in \{0.2, 0.4, 0.5, 0.6, 0.8\}$ (black lines in order from bottom to top). Black line: Theoretical expression. Blue dots: Simulations in this work. Red dots: Simulation data from [19, Fig. 7a]. Green dots: Simulation data from [18, Fig. 7a]. See *Supplementary information* §S2.1.4 for data.

Fig. 4 also shows that the magnitude of the plateau of current density varies according to the aspect ratio H/W of the unit cell. For $H/W \gtrsim 1$ the plateau remains the highest and the current density is approximately independent of H/W , mainly because radial diffusion is completely developed (see Fig. 3a), as in the case of semi-infinite cells. In the range of approximately $0.3 \lesssim H/W \lesssim 1$, the current density decreases slowly as the aspect ratio H/W decreases, due to truncation of the radial diffusion caused by the lower roof of the cell. In the range of approximately $0 \leq H/W \lesssim 0.3$, the current density decreases quickly as H/W decreases, with plateaus approaching zero for very low H/W , mainly because the vertical diffusion in the cell becomes almost nonexistent, and only horizontal diffusion between consecutive bands takes place (see Fig. 3b).

3.3 Current per band

The normalized current in Eq. (2.24) was contrasted against simulations of Eqs. (2.8) for different values of aspect ratio $H/W \in]0, 1.25[$ and electrode widths $2w_A/W = 2w_B/W \in]0, 1[$, see Fig. 5. In 44 of 45 analyzed cases, the maximum absolute error was not greater than ≈ 0.0078 , thus confirming the correctness of Eq. (2.24). The theoretical result also agrees with simulation results previously reported in the literature [18, Fig. 7a] [19, Fig. 7a], which are also shown in Fig. 5. For more details on the data see Tables S3, S4 and S5 in *Supplementary information* §S2.1.4.

3.3.1 Effect of the counter electrode in the collection efficiency

The expression in Eq. (2.24) shows that the currents at bands of both arrays are equal in magnitude but opposite $i_f^A = -i_f^B$. This suggests that 100% collection efficiency is a necessary condition for this expression to hold, which is immediately satisfied when the IDAE operates with internal counter electrode [8, start of p. 280] [35, p. 7558 mid col. 2].

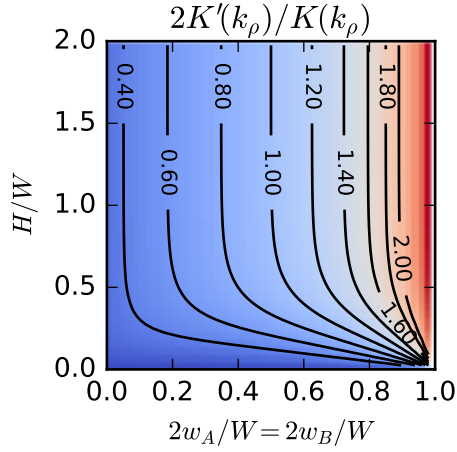
However, in the case of external counter electrode, the collection efficiency may not reach 100% [8, start of p. 280] [35, p. 7558 mid col. 2]. In case the roof of the cell is low ($H/W \lesssim 1$), the collection efficiency is close to 100% [18, Fig. 5b] [16, Fig. 5e] and Eq. (2.24) approximately holds. However, when the roof of the cell becomes taller ($H/W \gtrsim 1$), the collection efficiency departs from 100% and decreases [18, Fig. 5a] [16, Fig. 5e]. In this last case, a correction that takes into account the effect of external counter is needed to accurately predict the current through the IDAE. This kind of correction was done semi-empirically in [8, Eq. (33)] and later in [10, Eqs. (13) and (20)], both for the case of semi-infinite cells ($H \rightarrow +\infty$).

3.3.2 Influence of the cell geometry

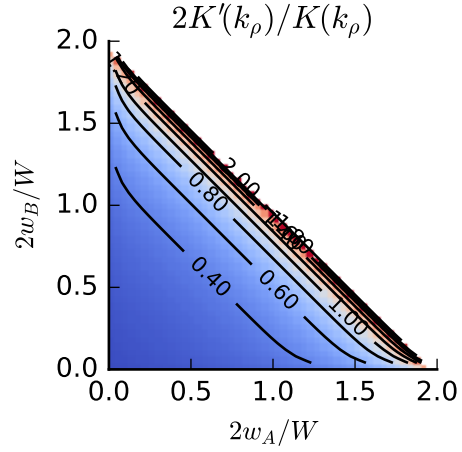
According to Corollary 2.2, the current in steady state through the IDAE depends on the ratio $2K'(k_\rho)/K(k_\rho)$, which is a purely geometrical factor, since the modulus k_ρ depends only on the relative dimensions of the unit cell $2w_A/W$, $2w_B/W$ and H/W , as seen in Eqs. (2.10) and (2.12). This implies that, for known electrochemical species in the cell (D_σ and n_e are known) and for known potentials applied to the IDAE (therefore $c_{\sigma,f}^A$ and $c_{\sigma,f}^B$ are also known), the performance of the cell can be optimized just by adjusting the widths of the electrode bands and the aspect ratio of the unit cell.

Visualization of the ratio $2K'(k_\rho)/K(k_\rho)$, as a function of its three geometrical parameters ($2w_A/W$, $2w_B/W$ and H/W), is helpful to find the right combination of cell dimensions that allow an optimal performance. However, this ratio is difficult to visualize, since it corresponds to a three-dimensional scalar field. Therefore, Fig. 6 shows two-dimensional slices and contour lines of the ratio $2K'(k_\rho)/K(k_\rho)$, as a function of the relative dimensions of the cell. These slices were chosen such that they provide enough information to understand how the normalized current $2K'(k_\rho)/K(k_\rho)$ behaves for different values of $2w_A/W$, $2w_B/W$ and H/W .

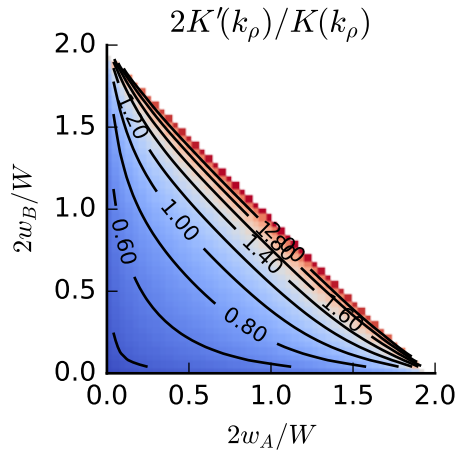
Figs. 5 and 6 show that the current increases as both the width of the electrode bands and the aspect ratio of the unit cell increase (similarly occurs for the case of elevated electrodes in the simulations of [15, Fig. 5] [33, Table 1] [34, Table 2]). For aspect ratios $H/W \gtrsim 1$, the current becomes



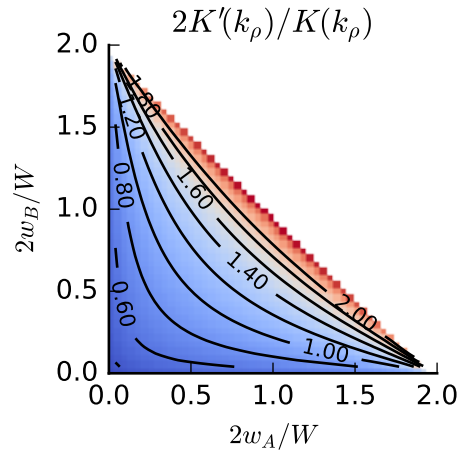
(a) Case of bands of equal width.



(b) Case $H/W = 0.1$.



(c) Case $H/W = 0.3$.



(d) Case $H/W = 1$.

Figure 6: Different slices and contour lines of the normalized current per band $2K'(k_\rho)/K(k_\rho) = \pm(i_f^E/L)/(Fn_eD_\sigma[c_{\sigma,f}^E - c_{\sigma,f}^{E'}])$. The normalized current is a function of the relative dimensions of the cell: $2w_A/W$, $2w_B/W$ and H/W .

independent of H/W , and only depends on the width of the electrode bands. For $0.3 \lesssim H/W \lesssim 1$ and fixed band widths, the current decreases slowly as the aspect ratio H/W decreases. For $0 \leq H/W \lesssim 0.3$ and fixed band widths, the current decreases much faster as the ratio H/W decreases. This variation in the magnitude of the current, in relation to the aspect ratio H/W , has the same explanation as the one given for the current density in the previous section, and relates to the truncation of the radial diffusion by a low roof of the cell.

Also, Figs. 5 and 6a confirm that there is a certain limit about $H/W \gtrsim 1$ where the cell is so high that diffusion is not affected by the roof of the cell, and the current approaches that of semi-infinite diffusion, as predicted earlier in [18, §3.2 and Fig. 7a] [19, §3.3 and Fig. 7a] [16, p. 309 and Fig. 5]. Similar results have been also found through simulations for the case of elevated electrodes [15, p.451 and Fig. 5b].

Finally, note that the amount of material used for fabricating the electrodes can be also optimized for a given current. This amount of material is proportional to $m = 2w_A/W + 2w_B/W$ and corresponds to an anti-diagonal line in the domain of Figs. 6b, c and d. Therefore, the minimum amount of utilized material that produces a desired current is obtained when $2w_A = 2w_B$. This can be seen by selecting a desired iso-current line, and intersecting it with the anti-diagonal $m = 2w_A/W + 2w_B/W$. This produces two intersection points, which are symmetric with respect to the diagonal line $2w_A/W = 2w_B/W$. The minimum of m is obtained by moving the anti-diagonal towards the origin, which makes the two intersection points on the iso-current line converge to a single point, thus obtaining $2w_A = 2w_B$.

3.4 Voltammogram shape

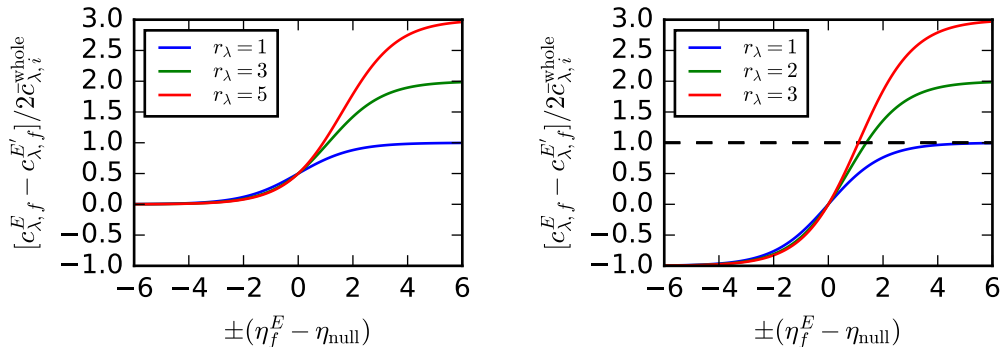
Consider the current¹² through one array of the IDAE, consisting of N_E bands of length L , see Eq. (2.24)

$$N_E i_f^E = \pm N_E L 2 \frac{K'(k_\rho)}{K(k_\rho)} \cdot F n_e D_\sigma [c_{\sigma,f}^E - c_{\sigma,f}^{E'}] \quad (3.1)$$

Here one can distinguish two clear factors with different roles: A geometrical factor $N_E L 2K'(k_\rho)/K(k_\rho)$ and an electrochemical factor $F n_e D_\sigma [c_{\sigma,f}^E - c_{\sigma,f}^{E'}]$.

The inherent shape of the voltammogram is solely due to the electrochemical factor, which is proportional to the difference of concentrations in Eqs (2.28) and (2.34). This inherent shape can be amplified or attenuated

¹² for \pm or \mp , the upper sign corresponds to $\sigma = O$, and the lower sign, to $\sigma = R$.



(a) Case of external counter electrode. (b) Case of internal counter electrode. Solid lines: Result in Eq. (2.28). Solid lines: Result in Eq. (2.34a). Dashed line: Saturation limit in Eq. (2.32) due to depletion.

Figure 7: Plot of the normalized difference of concentration $[c_{\lambda,f}^E - c_{\lambda,f}^{E'}]/2\bar{c}_{\lambda,i}^{\text{whole}}$ as a function of the normalized potential $\eta_f^E - \eta_{\text{null}} = (n_e F/RT)(V_f^E - V_{\text{null}})$ for different ratios $r_\lambda = (D_{\lambda'}\bar{c}_{\lambda',i}^{\text{whole}})/(D_\lambda\bar{c}_{\lambda,i}^{\text{whole}})$. Here λ and λ' correspond to the limiting species and its complementary species, such that $D_\lambda\bar{c}_{\lambda,i}^{\text{whole}} = \min(D_O\bar{c}_{O,i}^{\text{whole}}, D_R\bar{c}_{R,i}^{\text{whole}})$.

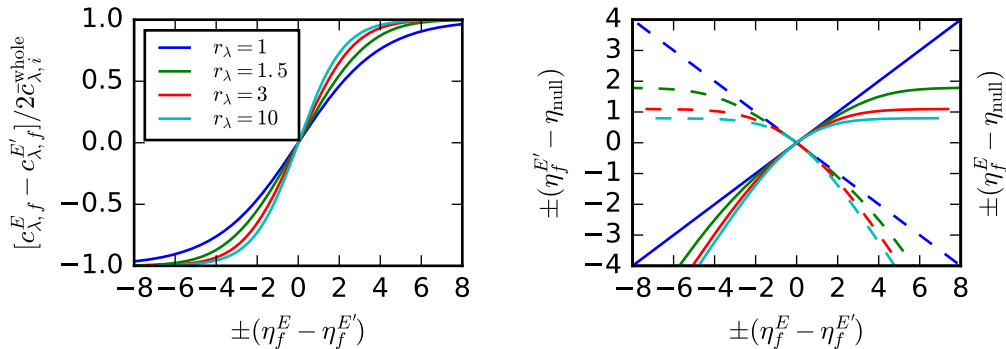
by the geometrical factor, which is shown in Figs. 5 and 6, and expressed approximately in Eqs. (2.43) and (2.45).

Therefore, here we examine the shape of the voltammogram just by looking at the behavior of the difference of concentrations in two cases: With external and internal counter electrodes.

The first, and the most commonly found in the literature, corresponds to the case where the counter electrode is external to the IDAE, which means that each array of the IDAE is potentiostated individually (commonly, the potential of one array is scanned, while the complementary array is fixed to a sufficiently negative potential).

Fig. 7a shows the plot of the normalized difference of concentrations when using an external counter electrode, see Eq. (2.28). This normalized difference (and thus the current) is unipolar (its is either always positive or always negative), and it increases with the weighted sum of initial concentrations of both electrochemical species. Moreover, the steady-state current reaches plateaus (limiting current) that are proportional to this weighted (total, when $D_O = D_R$) sum of concentrations [35, p. 7558 start of col. 2], when the applied potential at the scanning electrode exceeds $|\eta_f^E - \eta_{\text{null}}| \gtrsim 4$.

The second is the case where the counter electrode is internal to the



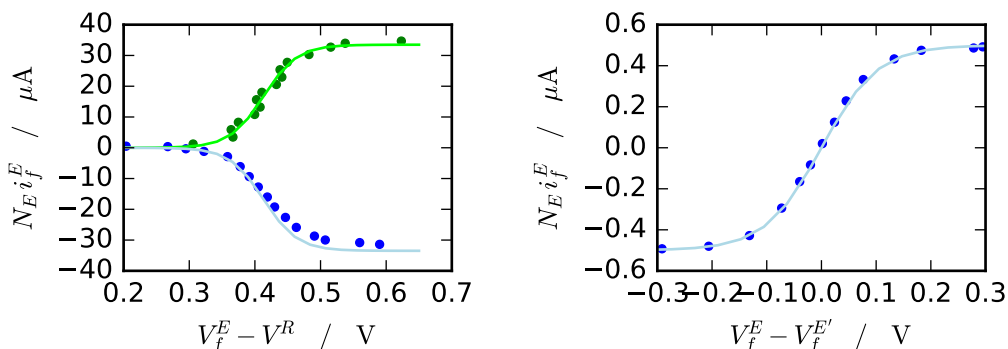
(a) Normalized difference of concentration $[c_{\lambda,f}^E - c_{\lambda,f}^{E'}] / 2\bar{c}_{\lambda,i}^{\text{whole}}$ as a function of the normalized voltage $\eta_f^E - \eta_f^{E'}$. See Eq. (2.34b). (b) Dependence of the normalized potentials $\eta_f^E - \eta_{\text{null}}$ (solid) and $\eta_f^{E'} - \eta_{\text{null}}$ (dashed) as a function of the normalized voltage $\eta_f^E - \eta_f^{E'}$. See Eqs. (2.34).

Figure 8: Case when the internal counter electrode is used as reference electrode, analyzed for different ratios $r_\lambda = (D_{\lambda'}\bar{c}_{\lambda',i}^{\text{whole}})/(D_\lambda\bar{c}_{\lambda,i}^{\text{whole}})$. Here λ and λ' are the determinant and its complementary species, such that $D_\lambda\bar{c}_{\lambda,i}^{\text{whole}} = \min(D_O\bar{c}_{O,i}^{\text{whole}}, D_R\bar{c}_{R,i}^{\text{whole}})$, $\eta_f^E - \eta_{\text{null}} = (Fn_e/RT)(V_f^E - V_{\text{null}})$ is the normalized working potential, $\eta_f^{E'} - \eta_{\text{null}} = (Fn_e/RT)(V_f^{E'} - V_{\text{null}})$ is the normalized counter potential, and $\eta_f^E - \eta_f^{E'}$ is the normalized voltage.

IDAE, which means that one of the arrays is potentiostated at will, while the complementary array performs as counter electrode (its potential is controlled automatically by the potentiostat).

Fig. 7b shows the plot of the normalized difference of concentrations when using an internal counter electrode, see Eq. (2.34a). This normalized difference (and thus the current) is bipolar (it is positive and negative in the same plot), and presents plateaus when the applied potential is sufficiently high $|\eta_f^E - \eta_{\text{null}}| \gtrsim 4$. Ideally, the magnitude of the difference of concentrations (steady-state current) should increase as the ratio $r_\lambda = (D_{\lambda'}\bar{c}_{\lambda',i})/(D_\lambda\bar{c}_{\lambda,i})$ between the electrochemical species increases, but it is actually limited by Eq. (2.32) (dashed line), due to depletion of its limiting species λ [19, Fig. 2]. This causes the limiting current to be proportional to the concentration of the limiting species, instead of the weighted sum of concentrations of both species [35, p. 7558 mid col. 2] [36, Fig. 2] [25, Fig. 3.4]. This fact has been also discussed in [10, §2.3] and [19, §2.3] and implies that simultaneous presence of both electrochemical species is a necessary condition to obtain steady state currents.

Note that, in case the internal counter electrode serves as reference elec-



(a) Case of external counter electrode. Dots: Experimental voltammogram of 1 nmol μl^{-1} ferrocene (reduced sp.) with $V_f^{E'} - V^R = -0.15$ V from [8, Fig. 7]¹³ for generator (green) and collector (blue). Lines: Curve fitting of the current at the generator using Eq. (3.2) with $k_0 = 33.5$ μA and $k_1 = -0.413$ V (green) and its reflection (blue). (b) Case of internal counter electrode. Dots: Experimental voltammogram of 0.20 nmol μl^{-1} of each ferrocyanide (reduced sp.) and ferricyanide (oxidized sp.) from [35, Fig. 2] or equivalently from [25, Fig. 3.12]. Line: Curve fitting using Eq. (3.3) with $k_0 = 0.499$ μA .

Figure 9: Curve fitting of experimental voltammogram by using the proposed models for external and internal counter electrodes. $N_E i_f^E$ and V_f^E corresponds to the total current and the potential applied to the working array, $V_f^{E'}$ is the potential at the counter array and V^R is the potential at the reference electrode (saturated calomel electrode).

trode, only a voltage (difference of potentials) can be applied to the cell. Fig. 8a shows that a sigmoidal shape is maintained under this condition, of which its plateaus (limiting current) are also proportional to the concentration of the limiting species, see Eq. (2.34b). Fig 8b shows how the applied voltage is distributed among the potentials of the working and counter electrodes. When the voltage applied to the cell increases in one direction, the potential at one electrode increases indefinitely, whereas the potential at the other electrode saturates in the opposite direction. This is due to depletion of the limiting species λ at the electrode with greatest potential (in absolute value). This phenomenon has been observed experimentally in [36, Fig. 3] [25, Fig. 3.6], where figures similar to Fig. 8b were obtained. See *Supplementary information* §S2.2.1 for more details on how Figs. 8a and 8b were generated.

¹³ [8, Fig. 7] actually used the set of electrodes (E) instead of (D). This can be seen by

Finally, we show that the models in Eqs. (2.28) and (2.34) are also applicable to fit experimental data. Combining Eq. (3.1) with Eq. (2.28), for the case of external counter electrode, leads to¹⁴

$$N_E i_f^E = \pm \frac{k_0}{1 + \exp\left(\mp \frac{F n_e}{RT} (V_f^E - V^R + k_1)\right)} \quad (3.2)$$

where the voltammogram is mirrored horizontally and vertically when changing the polarity at the complementary electrode [37, §3.3]. Fig. 9a shows that the model in Eq. (3.2) correctly fits the experimental data for the generator in [8, Fig. 7], whereas the data for the collector is slightly overestimated, thus showing that the collection efficiency is near 100%.

For the case of internal counter electrode with bands of equal width, we combine Eqs. (3.1) with (2.34b) when $D_O \bar{c}_{O,i}^{\text{whole}} = D_R \bar{c}_{R,i}^{\text{whole}}$, obtaining

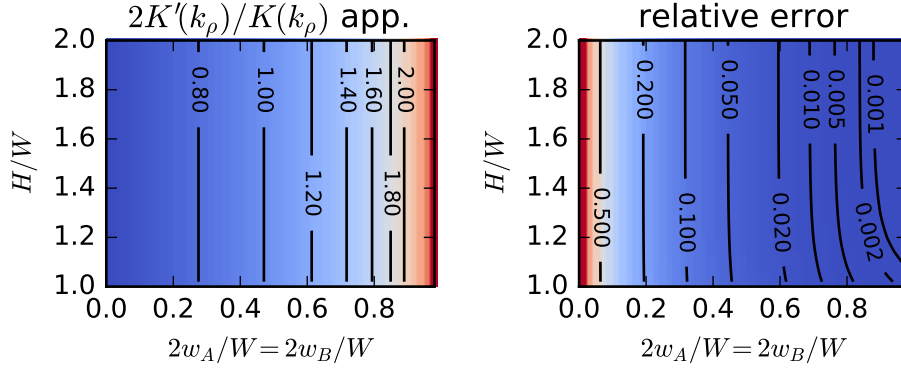
$$N_E i_f^E = k_0 \tanh\left(\frac{F n_e}{4RT} (V_f^E - V_f^{E'})\right) \quad (3.3)$$

Fig. 9b shows that this model also fits correctly the experimental data in [35, Fig. 2] [25, Fig. 3.12], both at the linear and the limiting current regions. For details on the experimental data used in both curve fittings see *Supplementary information* §S2.2.2.

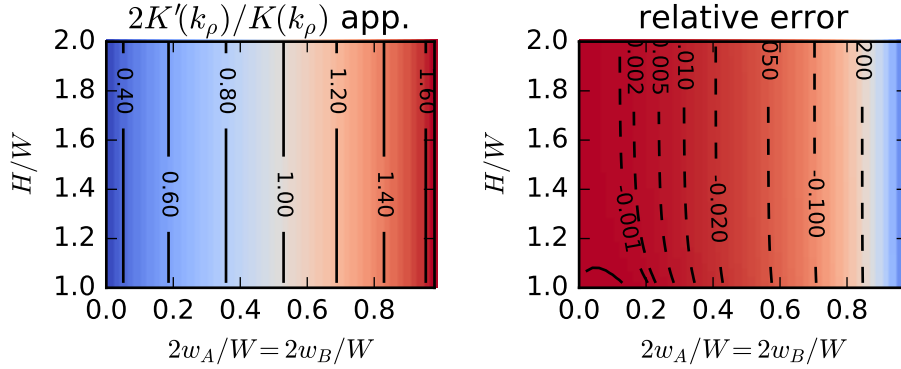
Remark 3.1. *Note that the models in Eqs. (2.28) and (2.34) for the difference of concentrations (shape of the steady-state voltammogram), in particular Eqs. (3.2) and (3.3), are valid for any electrochemical cell satisfying the following conditions: (i) The cell has reversible electrode reactions (Nernstian boundary conditions). (ii) The current is proportional to the difference between concentrations at both electrodes. (iii) The weighted sum of concentrations at each electrode satisfies a relation similar to Eq. (2.5). (iv) In case of internal counter electrode, the concentrations at both electrodes satisfy a relation similar to Eq. (2.29).*

dividing the limiting current from [8, Fig. 7] by the number of bands of (E) $\approx 34 \mu\text{A}/50 = 0.68 \mu\text{A}$, which corresponds to set (E) in [8, Fig. 8].

¹⁴ the upper sign corresponds to the case where the concentration of oxidized species at the complementary array is zero (at very negative potential), and the lower, to the case where the concentration of reduced species is zero (at very positive potential), see Corollary 2.2.



(a) Approximation in Eq. (2.43a) for large electrodes.



(b) Approximation in Eq. (2.43b) for small electrodes.

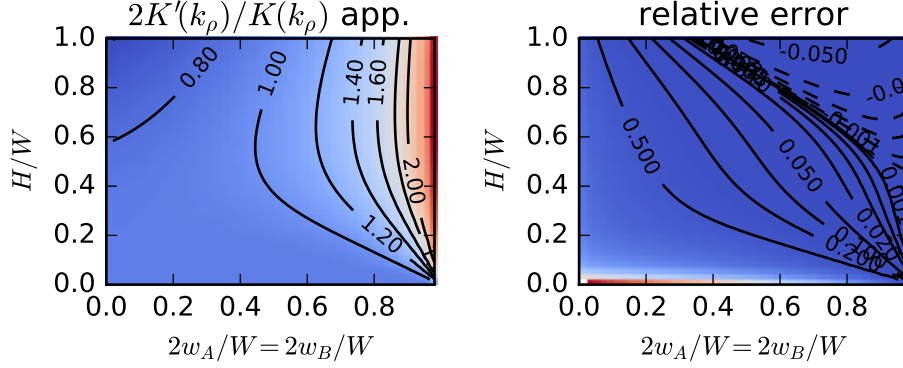
Figure 10: Approximation of the normalized current $2K'(k_\rho)/K(k_\rho) = \pm(i_f^E/N_E L)/(F n_e D_\sigma [c_{\sigma,f}^E - c_{\sigma,f}^{E'}])$ for tall electrochemical cells ($H/W > 1$).

This is because the previous conditions are properties that depend only on the boundary conditions at the electrodes, which are independent of the whole domain of the cell.

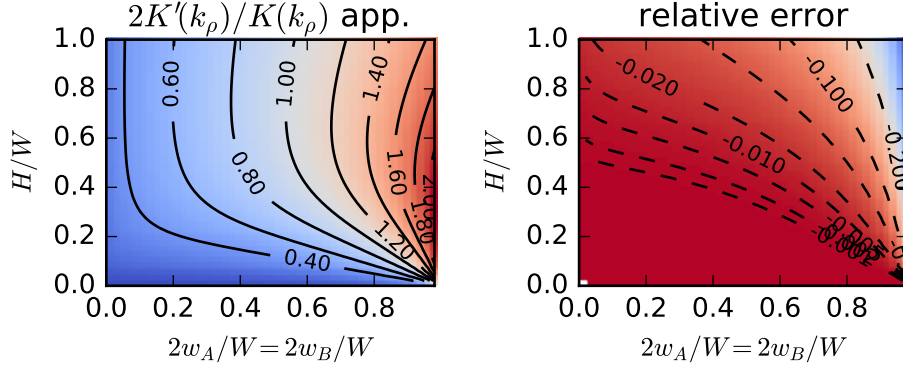
3.5 Approximations for shallow and tall cells

The approximations of the normalized current $2K'(k_\rho)/K(k_\rho)$ in Eqs. (2.43) for tall electrochemical cells are already available in the literature, and were obtained first by Aoki and colleagues, for the case of large electrodes [8, Eq. (32) and the equation above it], and later by Morf and colleagues, for the case of small electrodes [10, Eqs. (6) and (7)]. Therefore, these results serve as a validation of the exact results obtained in Corollary 2.2.

Fig. 10 shows the approximations for tall cells $H/W > 1$ as well as



(a) Approximation in Eq. (2.45a) for large electrodes.



(b) Approximation in Eq. (2.45b) for small electrodes.

Figure 11: Approximation of the normalized current $2K'(k_\rho)/K(k_\rho) = \pm(i_f^E/N_E L)/(F n_e D_\sigma [c_{\sigma,f}^E - c_{\sigma,f}^{E'}])$ for shallow electrochemical cells ($H/W \leq 1$).

their relative errors. Here the current becomes independent of H/W and depends only on the relative size of the electrodes. The approximation for large electrodes becomes accurate (error less than $\pm 5\%$) for bands of relative width > 0.46 . In the case of small electrodes, the approximation has an error less than $\pm 5\%$ for bands of relative width < 0.56 . The regions of approximation for both sizes of electrodes overlap, thus covering all cases of $H/W > 1$ with a relative error less than $\pm 5\%$ in the current. See Table 1 for a summary and *Supplementary information* §S2.2.3 for details on the errors.

Approximations of the normalized current $2K'(k_\rho)/K(k_\rho)$ in Eqs. (2.45) for shallow electrochemical cells are results that have not been published before. Fig. 11 shows the approximations for shallow cells $H/W \leq 1$ as well as their relative errors. The approximation for large electrodes becomes accurate (error less than $\pm 5\%$) for combinations of $(2w_E/W, H/W)$ approx-

Approx.	Cell	Electrodes	Domain
Eq. (2.43a)	Tall	Large	$2w_E/W > 0.46$
Eq. (2.43b)	Tall	Small	$2w_E/W < 0.56$
Eq. (2.45a)	Shallow	Large	$2w_E + (1 - 0.28)H \gtrsim W$
Eq. (2.45b)	Shallow	Small	$2w_E + (1 - 0.36)H \lesssim W$

Table 1: Regions where the approximations hold with a relative error less than $\pm 5\%$ for tall ($H/W > 1$) and shallow ($H/W \leq 1$) cells.

imately at the right of the line given by the points $(1, 0)$ and $(0.28, 1)$, where the line that passes through the points $(1, 0)$ and $(p, 1)$ is given by

$$\frac{2w_E}{W} + (1 - p)\frac{H}{W} = 1 \quad (3.4)$$

In the case of small electrodes, the approximation has an error less than $\pm 5\%$ for combinations of $(2w_E/W, H/W)$ approximately at the left of the line given by the points $(1, 0)$ and $(0.36, 1)$. The regions of approximation for both sizes of electrodes overlap, thus covering all cases of $H/W \leq 1$ with a relative error less than $\pm 5\%$ in the current. See Table 1 for a summary and *Supplementary information* §S2.2.3 for details on the errors.

4 Conclusions

Thanks to Jacobian elliptic functions, it is possible to transform the unit cell from the IDAE domain into a parallel-plates domain. In this last domain, the solution of the diffusion equation in steady state is simple, and corresponds to a linear interpolation of the concentrations on both plates. This solution is transformed back into the IDAE domain, leading to an analytical result for the concentration profile that depends on elliptic functions and integrals. Both, current density and current were derived from this concentration profile.

The results for the concentration profile, current density and current depend geometrically on the relative dimensions of the cell, not on absolute dimensions. Their behavior approaches that of an IDAE in a semi-infinite cell as it becomes taller (approximately when the cell is taller than the separation between centers of consecutive bands).

The shape obtained for the voltammogram is sigmoidal and can be unipolar (it has either always positive or always negative currents) or bipolar (presenting positive and negative currents) depending on whether the IDAE is bipotentiostated using an external counter electrode, or potentiostated using

one of its arrays as internal counter electrode. In case of using an external counter electrode, the plateaus of current (limiting current) are proportional to the weighted sum of initial concentrations (total initial concentration when the diffusion coefficients are equal). Whereas, in case of using an internal counter electrode, the plateaus of current (limiting current) are proportional to the limiting species, which will be the species of least concentration if the diffusion coefficients are equal.

Approximations for the exact results were found. Trigonometric and hyperbolic functions were used to approximate the cases of tall and shallow cells respectively. The approximations are accurate with a relative error smaller than $\pm 5\%$ with respect to the exact values. Finally, when the approximations are used in combination, they cover all possibilities of interest for IDAE in confined cells.

Acknowledgements

The authors deeply appreciate the aid and comments of Dr. Mithran Somasundrum, which helped to improve the quality of this manuscript. The authors would like to thank the financial support provided by *King Mongkut's University of Technology Thonburi* through the *KMUTT 55th Anniversary Commemorative Fund*, and the *Petchra Pra Jom Klao Ph. D. scholarship* (Grant No. 28/2558) for sponsoring CFGY. Finally, the authors acknowledge the *Higher Education Research Promotion and National Research University Project of Thailand, Office of the Higher Education Commission*, Ministry of Education, Thailand.

References

- [1] M. A. Dayton, J. C. Brown, K. J. Stutts, and R. M. Wightman. Faradaic electrochemistry at microvoltammetric electrodes. *Analytical Chemistry*, 52(6):946–950, 1980. doi:10.1021/ac50056a040.
- [2] A. G. Ewing, M. A. Dayton, and R. M. Wightman. Pulse voltammetry with microvoltammetric electrodes. *Analytical Chemistry*, 53(12):1842–1847, 1981. doi:10.1021/ac00235a028.
- [3] R. Mark Wightman. Microvoltammetric electrodes. *Analytical Chemistry*, 53(9):1125A–1134A, 1981. doi:10.1021/ac00232a004.
- [4] Robert J. Forster and Tia E. Keyes. *Behavior of ultramicroelectrodes*,

- chapter 6.1, pages 155 – 171. In Zoski [39], 1 edition, 2007. ISBN 978-0-444-51958-0. doi:10.1016/B978-044451958-0.50007-0.
- [5] Sabine Szunerits and Laurent Thouin. *Microelectrode Arrays*, chapter 10, pages 391 – XI. In Zoski [39], 1 edition, 2007. ISBN 978-0-444-51958-0. doi:10.1016/B978-044451958-0.50023-9.
- [6] Koichi Aoki. Theory of ultramicroelectrodes. *Electroanalysis*, 5(8):627–639, September 1993. ISSN 1040-0397. doi:10.1002/elan.1140050802.
- [7] Koichi Aoki and Mitsuya Tanaka. Time-dependence of diffusion-controlled currents of a soluble redox couple at interdigitated microarray electrodes. *Journal of Electroanalytical Chemistry*, 266(1):11–20, July 1989. ISSN 00220728. doi:10.1016/0022-0728(89)80211-6.
- [8] Koichi Aoki, Masao Morita, Osamu Niwa, and Hisao Tabei. Quantitative analysis of reversible diffusion-controlled currents of redox soluble species at interdigitated array electrodes under steady-state conditions. *Journal of Electroanalytical Chemistry and Interfacial Electrochemistry*, 256(2):269–282, December 1988. ISSN 00220728. doi:10.1016/0022-0728(88)87003-7.
- [9] Koichi Aoki. Theory of stationary current-potential curves at interdigitated microarray electrodes for quasi-reversible and totally irreversible electrode reactions. *Electroanalysis*, 2(3):229–233, April 1990. ISSN 1040-0397. doi:10.1002/elan.1140020310.
- [10] Werner E. Morf, Milena Koudelka-Hep, and Nicolaas F. de Rooij. Theoretical treatment and computer simulation of microelectrode arrays. *Journal of Electroanalytical Chemistry*, 590(1):47–56, May 2006. ISSN 15726657. doi:10.1016/j.jelechem.2006.01.028.
- [11] David C. Duffy, J. Cooper McDonald, Olivier J. A. Schueller, and George M. Whitesides. Rapid prototyping of microfluidic systems in poly(dimethylsiloxane). *Analytical Chemistry*, 70(23):4974–4984, December 1998. doi:10.1021/ac980656z. PMID: 21644679.
- [12] Younan Xia and George M. Whitesides. Soft lithography. *Annual Review of Materials Science*, 28(1):153–184, August 1998. doi:10.1146/annurev.matsci.28.1.153.
- [13] George M. Whitesides, Emanuele Ostuni, Shuichi Takayama, Xingyu Jiang, and Donald E. Ingber. Soft lithography in biology and biochemistry. *Annual Review of Biomedical Engineering*, 3(1):335–373, August 2001. ISSN 1523-9829. doi:10.1146/annurev.bioeng.3.1.335.

- [14] Wijitar Dungchai, Orawon Chailapakul, and Charles S. Henry. Electrochemical detection for paper-based microfluidics. *Analytical Chemistry*, 81(14):5821–5826, July 2009. doi:10.1021/ac9007573. PMID: 19485415.
- [15] Edgar D. Goluch, Bernhard Wolfrum, Pradyumna S. Singh, Marcel A. G. Zevenbergen, and Serge G. Lemay. Redox cycling in nanofluidic channels using interdigitated electrodes. *Analytical and Bioanalytical Chemistry*, 394(2):447–56, May 2009. ISSN 1618-2650. doi:10.1007/s00216-008-2575-x.
- [16] Yusuke Kanno, Takehito Goto, Kosuke Ino, Kumi Y. Inoue, Yasufumi Takahashi, Hitoshi Shiku, and Tomokazu Matsue. Su-8-based flexible amperometric device with ida electrodes to regenerate redox species in small spaces. *Analytical Sciences*, 30(2):305–309, 2014. doi:10.2116/analsci.30.305.
- [17] Penny M. Lewis, Leah Bullard Sheridan, Robert E. Gawley, and Ingrid Fritsch. Signal amplification in a microchannel from redox cycling with varied electroactive configurations of an individually addressable microband electrode array. *Analytical Chemistry*, 82(5):1659–68, March 2010. ISSN 1520-6882. doi:10.1021/ac901066p.
- [18] Jörg Strutwolf and D. E. Williams. Electrochemical sensor design using coplanar and elevated interdigitated array electrodes. a computational study. *Electroanalysis*, 17(2):169–177, February 2005. ISSN 1040-0397. doi:10.1002/elan.200403112.
- [19] Cristian Guajardo, Sirimarn Ngamchana, and Werasak Surareungchai. Mathematical modeling of interdigitated electrode arrays in finite electrochemical cells. *Journal of Electroanalytical Chemistry*, 705:19–29, September 2013. ISSN 15726657. doi:10.1016/j.jelechem.2013.07.014.
- [20] Keith Oldham and Jan Myland. *Fundamentals of electrochemical science*. Academic Press, 1994.
- [21] Tobin A. Driscoll and Lloyd N. Trefethen. *Schwarz-Christoffel mapping*, volume 8. Cambridge University Press, 2002.
- [22] Frank W. J. Olver, Adri B. Olde Daalhuis, Daniel W. Lozier, Barry I. Schneider, Ronald F. Boisvert, Charles W. Clark, Bruce R. Miller, and Bonita V. Saunders, editors. *NIST Digital Library of Mathematical Functions*. March 2018. URL <http://dlmf.nist.gov/>. Release 1.0.18.

- [23] Mark J. Ablowitz and Athanassios S. Fokas. *Complex variables: Introduction and applications*. Cambridge University Press, 2nd edition, April 2003.
- [24] Peter J. Olver. Complex analysis and conformal mapping, September 2018. URL http://www-users.math.umn.edu/~olver/ln_/cml.pdf.
- [25] Mohammad Mehdi Rahimi. Cyclic biamperometry. Master's thesis, University of Waterloo, August 2009. URL <http://hdl.handle.net/10012/4555>.
- [26] Zeev Nehari. *Conformal Mapping*. International series in pure and applied mathematics. McGraw-Hill, 1952.
- [27] Adolf Kneser. Neue untersuchung einer reihe aus der theorie der elliptischen funktionen. *Journal für die reine und angewandte Mathematik*, 158:209–218, 1927. URL [https://gdz.sub.uni-goettingen.de/id/PPN243919689_0158?tify={"pages":\[221\],"view":"toc"}](https://gdz.sub.uni-goettingen.de/id/PPN243919689_0158?tify={).
- [28] B.C. Carlson. Symmetry in c , d , n of jacobian elliptic functions. *Journal of Mathematical Analysis and Applications*, 299(1):242 – 253, November 2004. ISSN 0022-247X. doi:10.1016/j.jmaa.2004.06.049.
- [29] J. D. Fenton and R. S. Gardiner-Garden. Rapidly-convergent methods for evaluating elliptic integrals and theta and elliptic functions. *The ANZIAM Journal*, 24:47–58, July 1982. ISSN 1446-8735. doi:10.1017/S0334270000003301.
- [30] Eric Jones, Travis Oliphant, Pearu Peterson, et al. SciPy: Open source scientific tools for Python, January 2016. URL <http://www.scipy.org/>.
- [31] Fredrik Johansson et al. mpmath: a Python library for arbitrary-precision floating-point arithmetic, December 2015. URL <http://mpmath.org/>.
- [32] Jonathan E. Guyer, Daniel Wheeler, and James A. Warren. Fipy: Partial differential equations with python. *Computing in Science & Engineering*, 11(3):6–15, May 2009. ISSN 1521-9615. doi:10.1109/mcse.2009.52.
- [33] Jeong-Il Heo, Yeongjin Lim, and Heungjoo Shin. The effect of channel height and electrode aspect ratio on redox cycling at carbon interdigitated array nanoelectrodes confined in a microchannel. *Analyst*, 138:6404–6411, 2013. doi:10.1039/C3AN00905J.

- [34] Jeong-Il Heo. Development of electrochemical sensor based on carbon interdigitated array nanoelectrodes for high current amplification. Master's thesis, Ulsan National Institute of Science and Technology, June 2014. URL <http://www.dcollection.net/handler/unist/000001924804>.
- [35] Mehdi Rahimi and Susan R. Mikkelsen. Cyclic biamperometry at micro-interdigitated electrodes. *Analytical Chemistry*, 83(19):7555–7559, 2011. doi:10.1021/ac2012703. PMID: 21870855.
- [36] Mehdi Rahimi and Susan R. Mikkelsen. Cyclic biamperometry. *Analytical Chemistry*, 82(5):1779–1785, March 2010. doi:10.1021/ac902383w.
- [37] Amélie J. C. Wahl, Ian P. Seymour, Micheal Moore, Pierre Lovera, Alan O’Riordan, and James F. Rohan. Diffusion profile simulations and enhanced iron sensing in generator-collector mode at interdigitated nanowire electrode arrays. *Electrochimica Acta*, 277:235–243, July 2018. doi:10.1016/j.electacta.2018.04.181.
- [38] Dieter Britz and Jörg Strutwolf. *Digital Simulation in Electrochemistry*. Monographs in Electrochemistry. Springer International Publishing, 4 edition, 2016. ISBN 978-3-319-30290-4, 978-3-319-30292-8. doi:10.1007/978-3-319-30292-8.
- [39] Cynthia G. Zoski, editor. *Handbook of Electrochemistry*. Elsevier, Amsterdam, 1 edition, 2007. ISBN 978-0-444-51958-0. doi:10.1016/b978-0-444-51958-0.x5000-9.

Supplementary information

Steady-state theory of interdigitated array of electrodes in confined spaces: Case of pure diffusion and reversible electrode reactions

Cristian F. GUAJARDO YÉVENES and Werasak SURAREUNGCHAI

King Mongkut's University of Technology Thonburi, 49 Soi Thianthale 25, Thanon Bangkhunthian Chaithale, Bangkok 10150, Thailand

S1 Additional proofs

S1.1 Transformation of the unit cell domain

S1.1.1 From \mathbf{r} to \mathbf{v} domain

Considering the special values of the function $\operatorname{arcsn}()$ [22, Table 22.5.1]

$$0 = \operatorname{arcsn}(0, k) \quad (\text{S1.1a})$$

$$\pm K(k) = \operatorname{arcsn}(\pm 1, k) \quad (\text{S1.1b})$$

$$\pm K(k) + iK'(k) = \operatorname{arcsn}(\pm 1/k, k) \quad (\text{S1.1c})$$

$$iK'(k) = \operatorname{arcsn}(\infty, k) \quad (\text{S1.1d})$$

one can construct a function $(T_r^v)^{-1}$ that maps the upper half-plane of \mathbf{v} into the IDAE domain \mathbf{r} , as shown in Fig. S1. The scale and translation of the function $\operatorname{arcsn}()$ must be chosen such that $\mathbf{v}_a = -1$ is mapped to $\mathbf{r}_a = 0$ and $\mathbf{v}_b = 1$ is mapped to $\mathbf{r}_b = W$, which leads to

$$\mathbf{r} = (T_r^v)^{-1}(\mathbf{v}) = \frac{W}{2} \left[1 + \frac{1}{K(k_r)} \operatorname{arcsn}(\mathbf{v}, k_r) \right] \quad (\text{S1.2a})$$

$$\mathbf{v} = T_r^v(\mathbf{r}) = \operatorname{sn} \left(K(k_r) \frac{2\mathbf{r}}{W} - K(k_r), k_r \right) = -\operatorname{cd} \left(K(k_r) \frac{2\mathbf{r}}{W}, k_r \right) \quad (\text{S1.2b})$$

which corresponds to Eq. (2.9d) due to the quarter- and half-period properties [22, Table 22.4.3]

$$\operatorname{sn}(\mathbf{u} - K(k), k) = \operatorname{sn}(\mathbf{u} + K(k) - 2K(k), k) = -\operatorname{cd}(\mathbf{u}, k) \quad (\text{S1.3})$$

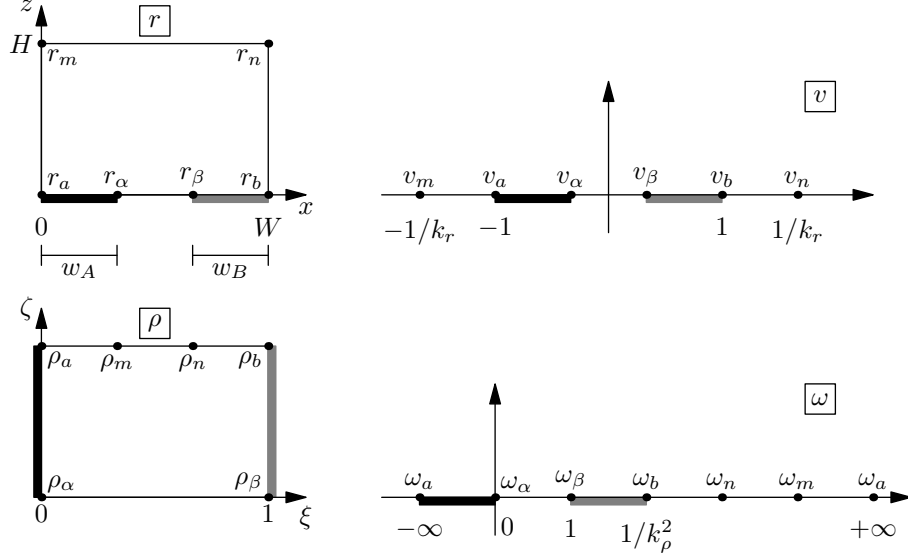


Figure S1: Complex transformation of the IDAE domain $\mathbf{r} = (x, z)$ into the conformal parallel-plates domain $\boldsymbol{\rho} = (\xi, \zeta)$, by using the auxiliary complex domains \mathbf{v} and $\boldsymbol{\omega}$.

The appropriate modulus k_r can be obtained by forcing $\mathbf{v}_m = -1/k_r$ to be mapped to the upper-left corner $\mathbf{r}_m = iH$

$$\mathbf{r}_m = (T_r^v)^{-1}(\mathbf{v}_m) \Leftrightarrow iH = i \frac{W}{2} \frac{K'(k_r)}{K(k_r)} \Leftrightarrow \frac{K'(k_r)}{K(k_r)} = \frac{2H}{W} \quad (\text{S1.4})$$

which leads to Eq. (2.10b), by applying the inverse nome function Eq. (2.35) [22, Eqs. (19.2.9) and (22.2.1)]. Therefore, the function T_r^v in Eq. (S1.2b) transforms the IDAE domain \mathbf{r} into the upper half-plane \mathbf{v} as shown in Fig. S1.

Finally, the point \mathbf{v}_α , in Eq. (2.12a), is obtained directly by evaluating Eq. (S1.2b). Whereas the point \mathbf{v}_β , in Eq. (2.12b), is obtained by evaluating Eq. (S1.2b), and by combining the fact that $\text{sn}()$ is an odd function and Eq. (S1.3).

S1.1.2 From \mathbf{v} to $\boldsymbol{\omega}$ domain

The function T_v^ω in Eq. (2.9c), which is also shown below for convenience,

$$\boldsymbol{\omega} = T_v^\omega(\mathbf{v}) = \frac{(\mathbf{v} - \mathbf{v}_\alpha)(\mathbf{v}_\beta - \mathbf{v}_a)}{(\mathbf{v} - \mathbf{v}_a)(\mathbf{v}_\beta - \mathbf{v}_\alpha)} \quad (\text{S1.5})$$

corresponds to a Möbius function and it is constructed such that: (i) it maps the upper half-plane of \mathbf{v} into the upper half-plane of $\boldsymbol{\omega}$ and (ii) it maps the

half band of A to the negative real axis of ω and the half band of B to the real interval $\omega \in [1, \omega_b]$, see Fig. S1.

Condition (ii) is immediately achieved, since Eq. (S1.5) maps \mathbf{v}_a , \mathbf{v}_α and \mathbf{v}_β into $\omega_a = \infty$, $\omega_\alpha = 0$ and $\omega_\beta = 1$. Condition (i) can be analyzed by rewriting Eq. (S1.5) as a composition of translations, rotations and scalings, and inversion

$$\omega = T_v^\omega(\mathbf{v}) = \left[1 + \frac{\mathbf{v}_a - \mathbf{v}_\alpha}{\mathbf{v} - \mathbf{v}_a} \right] \underbrace{\left[\frac{\mathbf{v}_\beta - \mathbf{v}_a}{\mathbf{v}_\beta - \mathbf{v}_\alpha} \right]}_p \quad (\text{S1.6})$$

The fact that $\mathbf{v}_a \in \mathbb{R}$, $\mathbf{v}_a - \mathbf{v}_\alpha < 0$ and $p > 0$ ensures that the upper half-plane of \mathbf{v} is mapped to the upper half-plane of ω . See [23, Eq. (5.7.3)], [26, §V.2 Eqs. (6), (7) and (10)] or [24, Examples 5.3 and 5.4] for more details on decomposition and mapping of Möbius functions.

S1.1.3 From ω to ρ domain

The function T_ω^ρ in Eq. (2.9b), which is written below for convenience,

$$\rho = T_\omega^\rho(\omega) = \frac{1}{K(k_\rho)} \operatorname{arcsn}(\sqrt{\omega}, k_\rho) \quad (\text{S1.7})$$

is in charge of mapping the upper half-plane of ω into the parallel-plates domain ρ , see Fig. S1. This is achieved in two stages: (i) The upper half-plane of ω is mapped to the first quadrant of $\sqrt{\omega}$, such that the half band of A is mapped to the positive imaginary axis of $\sqrt{\omega}$ and the half band of B is mapped to the real interval $\sqrt{\omega} \in [1, \sqrt{\omega_b}]$. (ii) The first quadrant of $\sqrt{\omega}$ is mapped to the parallel-plates domain ρ by using the special values of $\operatorname{arcsn}()$ in Eqs. (S1.1) or [22, Table 22.5.1].

The scaling and translation of the function $\operatorname{arcsn}()$ are chosen such that $\sqrt{\omega_\alpha} = 0$ is mapped to $\rho_\alpha = 0$ and $\sqrt{\omega_\beta} = 1$ is mapped to $\rho_\beta = 1$, which leads to Eq. (S1.7). The appropriate modulus k_ρ is obtained by choosing $\sqrt{\omega_b} = 1/k_\rho$, such that $\sqrt{\omega_b}$ be mapped to the upper right corner ρ_b of the parallel-plates domain, leading to Eq. (2.10a).

Finally, the point ρ_a , in Eqs. (2.13), can be obtained directly by evaluating $\sqrt{\omega_a} = \infty$ in Eq. (S1.7), by using the properties in (S1.1).

S1.1.4 Conformality of the transformation

The conformality of T_r^ρ comes from the fact that T_r^ρ has non-zero complex derivative in the interior of the IDAE domain. This can be seen from Eq. (2.20) or (S1.14), where the zeros of $\operatorname{nd}(K(k_r)2\mathbf{r}/W, k_r)$

$$\mathbf{r} = mW + (2n + 1)\mathbf{i}H \quad m, n \in \mathbb{Z} \quad (\text{S1.8})$$

lay only on the top vertices of the IDAE domain. These zeros are obtained by using [22, Table 22.4.2] and Eq. (S1.4).

S1.2 Derivative of the domain transformation

This proof concerns about obtaining the complex derivative of the domain transformation T_r^ρ in Eqs. (2.9), which is written below for convenience

$$\boldsymbol{\rho} = T_r^\rho(\mathbf{r}) = T_\omega^\rho \circ T_v^\omega \circ T_r^v(\mathbf{r}) \quad (\text{S1.9a})$$

$$\boldsymbol{\rho} = T_\omega^\rho(\boldsymbol{\omega}) = \frac{1}{K(k_\rho)} \operatorname{arcsn}(\sqrt{\boldsymbol{\omega}}, k_\rho) \quad (\text{S1.9b})$$

$$\boldsymbol{\omega} = T_v^\omega(\mathbf{v}) = \frac{(\mathbf{v} - \mathbf{v}_\alpha)(\mathbf{v}_\beta - \mathbf{v}_a)}{(\mathbf{v} - \mathbf{v}_a)(\mathbf{v}_\beta - \mathbf{v}_\alpha)} \quad (\text{S1.9c})$$

$$\mathbf{v} = T_r^v(\mathbf{r}) = -\operatorname{cd}\left(K(k_r)\frac{2\mathbf{r}}{W}, k_r\right) \quad (\text{S1.9d})$$

First, the complex derivative of each component of T_r^ρ , in Eq. (S1.9), is taken

$$\frac{\partial \boldsymbol{\rho}}{\partial \boldsymbol{\omega}} = \frac{1}{2K(k_\rho)} \frac{1}{\boldsymbol{\omega}^{1/2}(1-\boldsymbol{\omega})^{1/2}(1-k_\rho^2\boldsymbol{\omega})^{1/2}} \quad (\text{S1.10a})$$

$$\frac{\partial \boldsymbol{\omega}}{\partial \mathbf{v}} = \frac{(\mathbf{v}_\alpha - \mathbf{v}_a)(\mathbf{v}_\beta - \mathbf{v}_a)}{(\mathbf{v} - \mathbf{v}_a)^2(\mathbf{v}_\beta - \mathbf{v}_\alpha)} \quad (\text{S1.10b})$$

$$\frac{\partial \mathbf{v}}{\partial \mathbf{r}} = k_r'^2 \operatorname{sd}\left(K(k_r)\frac{2\mathbf{r}}{W}, k_r\right) \operatorname{nd}\left(K(k_r)\frac{2\mathbf{r}}{W}, k_r\right) \frac{2}{W} K(k_r) \quad (\text{S1.10c})$$

where

$$\boldsymbol{\omega} = \frac{(\mathbf{v} - \mathbf{v}_\alpha)(\mathbf{v}_\beta - \mathbf{v}_a)}{(\mathbf{v} - \mathbf{v}_a)(\mathbf{v}_\beta - \mathbf{v}_\alpha)} \quad (\text{S1.11a})$$

$$(1 - \boldsymbol{\omega}) = \frac{(\mathbf{v} - \mathbf{v}_\beta)(\mathbf{v}_\alpha - \mathbf{v}_a)}{(\mathbf{v} - \mathbf{v}_a)(\mathbf{v}_\beta - \mathbf{v}_\alpha)} e^{i(\pi+2\pi\mathbb{Z})} \quad (\text{S1.11b})$$

$$(1 - k_\rho^2\boldsymbol{\omega}) = \frac{(\mathbf{v}_b - \mathbf{v})(\mathbf{v}_\alpha - \mathbf{v}_a)}{(\mathbf{v} - \mathbf{v}_a)(\mathbf{v}_b - \mathbf{v}_\alpha)} \quad (\text{S1.11c})$$

since $1/k_\rho^2 = \boldsymbol{\omega}_b = T_v^\omega(\mathbf{v}_b)$. Later, two components are combined

$$\frac{\partial \boldsymbol{\rho}}{\partial \boldsymbol{\omega}} \frac{\partial \boldsymbol{\omega}}{\partial \mathbf{v}} = \frac{e^{-i(\pi/2+\pi\mathbb{Z})}}{2K(k_\rho)} \frac{(\mathbf{v}_b - \mathbf{v}_\alpha)^{1/2}(\mathbf{v}_\beta - \mathbf{v}_a)^{1/2}}{(\mathbf{v} - \mathbf{v}_\alpha)^{1/2}(\mathbf{v} - \mathbf{v}_\beta)^{1/2}} \frac{1}{(\mathbf{v} - \mathbf{v}_a)^{1/2}(\mathbf{v}_b - \mathbf{v})^{1/2}} \quad (\text{S1.12})$$

which leads to an expression that consists of two complex branches: $e^{-i(\pi/2+\pi\mathbb{Z})} = \pm i$. Using the identity $1 - \text{cd}(\mathbf{u}, k)^2 = k'^2 \text{sd}(\mathbf{u}, k)^2$ from [22, Eq. (22.6.4)] [28, Eq. (1.1)] and $\mathbf{v}_a = -1$ and $\mathbf{v}_b = 1$ from Fig. S1

$$(\mathbf{v} - \mathbf{v}_a)(\mathbf{v}_b - \mathbf{v}) = 1 - \mathbf{v}^2 = k_r'^2 \text{sd}\left(K(kr)\frac{2\mathbf{r}}{W}, kr\right)^2 \quad (\text{S1.13})$$

the final expression for the complex derivative can be obtained

$$\frac{\partial \rho}{\partial \omega} \frac{\partial \omega}{\partial \mathbf{v}} \frac{\partial \mathbf{v}}{\partial \mathbf{r}} = \pm i \frac{k_r'}{W} \frac{K(k_r)}{K(k_\rho)} \frac{(\mathbf{v}_b - \mathbf{v}_a)^{1/2} (\mathbf{v}_\beta - \mathbf{v}_a)^{1/2}}{(\mathbf{v} - \mathbf{v}_a)^{1/2} (\mathbf{v} - \mathbf{v}_\beta)^{1/2}} \text{nd}\left(K(kr)\frac{2\mathbf{r}}{W}, kr\right) \quad (\text{S1.14})$$

In case $c_{O,f}^B > c_{O,f}^A$, the current density at each electrode band B must be positive

$$j_f(x) = Fn_e D_O [c_{O,f}^B - c_{O,f}^A] \Im \frac{\partial \rho}{\partial \mathbf{r}}(x) \quad (\text{S1.15})$$

In order to achieve this, the $+i$ branch of the complex derivative must be chosen as the one carrying physical meaning, such that the current density be positive on each electrode band B .

S1.3 Differences of concentrations when using internal counter electrode

S1.3.1 Difference with respect to the average in the unit cell

Inside the unit cell the average concentration satisfies [19, Remark 2.2]

$$\int_{\text{unit}} c_{\sigma,f}(x, z) - \bar{c}_{\sigma,i}^{\text{unit}} dx = 0 \quad (\text{S1.16a})$$

(either when an integer number of unit cells fits exactly in the whole cell, or when it doesn't, at least the number of unit cells is large enough) since the counter electrode is internal to the IDAE. Considering that the concentrations at the bands A and B are uniform, due to reversible electrode reactions, one obtains

$$w_A [c_{\sigma,f}^A - \bar{c}_{\sigma,i}^{\text{unit}}] + \int_{w_A}^{W-w_B} c_{\sigma,f}(x, z) - \bar{c}_{\sigma,i}^{\text{unit}} dx + w_B [c_{\sigma,f}^B - \bar{c}_{\sigma,i}^{\text{unit}}] = 0 \quad (\text{S1.16b})$$

If the bands have equal width $2w_A = 2w_B$, the integral in the gap between consecutive bands is zero, due to symmetry, which leads to

$$[c_{\sigma,f}^A - \bar{c}_{\sigma,i}^{\text{unit}}] + [c_{\sigma,f}^B - \bar{c}_{\sigma,i}^{\text{unit}}] = 0 \quad (\text{S1.16c})$$

S1.3.2 Difference with respect to the average in the whole cell

Note that the average in the unit cell may not equal that in the whole cell

$$\int_{\text{whole}} c_{\sigma,f}(x, z) - \bar{c}_{\sigma,i}^{\text{whole}} dx = 0 \quad (\text{S1.17a})$$

this can be seen by separating the integral inside the IDAE and outside it (IDAE')

$$\int_{\text{IDAE}} c_{\sigma,f}(x, z) - \bar{c}_{\sigma,i}^{\text{whole}} dx + \int_{\text{IDAE}'} c_{\sigma,f}(x, z) - \bar{c}_{\sigma,i}^{\text{whole}} dx = 0 \quad (\text{S1.17b})$$

$$2WN_E[\bar{c}_{\sigma,i}^{\text{unit}} - \bar{c}_{\sigma,i}^{\text{whole}}] + \int_{\text{IDAE}'} c_{\sigma,f}(x, z) - \bar{c}_{\sigma,i}^{\text{whole}} dx = 0 \quad (\text{S1.17c})$$

Since the thickness of the fully-developed diffusion layer is in the order of the center-to-center separation between consecutive bands (namely kW), and any concentration outside the diffusion layer should equal the bulk $\bar{c}_{\sigma,i}^{\text{whole}}$, then

$$2WN_E[\bar{c}_{\sigma,i}^{\text{unit}} - \bar{c}_{\sigma,i}^{\text{whole}}] + 2kW[c_{\sigma,f}(x_o, z) - \bar{c}_{\sigma,i}^{\text{whole}}] = 0 \quad (\text{S1.17d})$$

where x_o is some value within the diffusion layer, due to the *first mean value theorem for integrals* [22, Eq. (1.4.29)] (note that the choice of k and x_o depends on z).

Therefore, the larger the number of bands N_E , the closer the averages $\bar{c}_{\sigma,i}^{\text{unit}} = \bar{c}_{\sigma,i}^{\text{whole}}$. This leads to the following equality when the bands satisfy $2w_A = 2w_B$

$$[c_{\sigma,f}^A - \bar{c}_{\sigma,i}^{\text{whole}}] = -[c_{\sigma,f}^B - \bar{c}_{\sigma,i}^{\text{whole}}] \quad (\text{S1.18})$$

due to the result in the previous section, which allows to estimate the unknown concentration on the internal counter electrode.

S1.3.3 Limits for the differences of concentration

To obtain the limits for the difference of concentration in steady state, one considers Eq. (S1.18) with non-negative concentrations on all electrodes

$$-\bar{c}_{\sigma,i}^{\text{whole}} \leq [c_{\sigma,f}^E - \bar{c}_{\sigma,i}^{\text{whole}}] = -[c_{\sigma,f}^{E'} - \bar{c}_{\sigma,i}^{\text{whole}}] \leq \bar{c}_{\sigma,i}^{\text{whole}} \quad (\text{S1.19a})$$

$$-\bar{c}_{\sigma',i}^{\text{whole}} \leq [c_{\sigma',f}^E - \bar{c}_{\sigma',i}^{\text{whole}}] = -[c_{\sigma',f}^{E'} - \bar{c}_{\sigma',i}^{\text{whole}}] \leq \bar{c}_{\sigma',i}^{\text{whole}} \quad (\text{S1.19b})$$

where E' are the complementary bands of $E \in \{A, B\}$ and σ' is the complementary species of $\sigma \in \{O, R\}$.

The limits for the concentration of species σ' may also affect the limits for the concentration of species σ . This can be seen by applying the weighted sum of concentrations in Eq. (2.3b) at the bands E and E'

$$D_\sigma [c_{\sigma,f}^E - \bar{c}_{\sigma,i}^{\text{whole}}] + D_{\sigma'} [c_{\sigma',f}^E - \bar{c}_{\sigma',i}^{\text{whole}}] = 0 \quad (\text{S1.20a})$$

$$D_\sigma [c_{\sigma,f}^{E'} - \bar{c}_{\sigma,i}^{\text{whole}}] + D_{\sigma'} [c_{\sigma',f}^{E'} - \bar{c}_{\sigma',i}^{\text{whole}}] = 0 \quad (\text{S1.20b})$$

which agrees with [10, Eqs. (15) and (16)] when $D_O = D_R$.

Combining the last four equations leads to

$$-D_\sigma \bar{c}_{\sigma,i}^{\text{whole}} \leq D_\sigma [c_{\sigma,f}^E - \bar{c}_{\sigma,i}^{\text{whole}}] = -D_\sigma [c_{\sigma,f}^{E'} - \bar{c}_{\sigma,i}^{\text{whole}}] \leq D_\sigma \bar{c}_{\sigma,i}^{\text{whole}} \quad (\text{S1.21a})$$

$$-D_{\sigma'} \bar{c}_{\sigma',i}^{\text{whole}} \leq D_\sigma [c_{\sigma,f}^E - \bar{c}_{\sigma,i}^{\text{whole}}] = -D_\sigma [c_{\sigma,f}^{E'} - \bar{c}_{\sigma,i}^{\text{whole}}] \leq D_{\sigma'} \bar{c}_{\sigma',i}^{\text{whole}} \quad (\text{S1.21b})$$

which can be summarized as

$$-D_\lambda \bar{c}_{\lambda,i}^{\text{whole}} \leq D_\sigma [c_{\sigma,f}^E - \bar{c}_{\sigma,i}^{\text{whole}}] = -D_\sigma [c_{\sigma,f}^{E'} - \bar{c}_{\sigma,i}^{\text{whole}}] \leq D_\lambda \bar{c}_{\lambda,i}^{\text{whole}} \quad (\text{S1.22})$$

when defining $D_\lambda \bar{c}_{\lambda,i}^{\text{whole}} = \min(D_O \bar{c}_{O,i}^{\text{whole}}, D_R \bar{c}_{R,i}^{\text{whole}})$.

S1.4 Difference of potential (voltage) when using internal counter electrode

Consider Eq. (2.34a) with $c_{\sigma,f}^E - c_{\sigma,f}^{E'} = 2[c_{\sigma,f}^E - \bar{c}_{\sigma,i}^{\text{whole}}] = -2[c_{\sigma,f}^{E'} - \bar{c}_{\sigma,i}^{\text{whole}}]$, which is written below for convenience

$$\frac{c_{\sigma,f}^E - \bar{c}_{\sigma,i}^{\text{whole}}}{\bar{c}_{\sigma,i}^{\text{whole}}} = \frac{D_{\sigma'} \bar{c}_{\sigma',i}^{\text{whole}} - D_{\sigma'} \bar{c}_{\sigma',i}^{\text{whole}} e^{\mp(\eta_f^E - \eta_{\text{null}})}}{D_\sigma \bar{c}_{\sigma,i}^{\text{whole}} + D_{\sigma'} \bar{c}_{\sigma',i}^{\text{whole}} e^{\mp(\eta_f^E - \eta_{\text{null}})}} = \frac{1 - e^{\mp(\eta_f^E - \eta_{\text{null}})}}{r_\sigma^{-1} + e^{\mp(\eta_f^E - \eta_{\text{null}})}} \quad (\text{S1.23a})$$

where $r_\sigma = (D_{\sigma'} \bar{c}_{\sigma',i}^{\text{whole}})/(D_\sigma \bar{c}_{\sigma,i}^{\text{whole}})$. A similar expressions is obtained at the complementary electrode E'

$$-\frac{c_{\sigma,f}^{E'} - \bar{c}_{\sigma,i}^{\text{whole}}}{\bar{c}_{\sigma,i}^{\text{whole}}} = \frac{D_{\sigma'} \bar{c}_{\sigma',i}^{\text{whole}} - D_{\sigma'} \bar{c}_{\sigma',i}^{\text{whole}} e^{\mp(\eta_f^{E'} - \eta_{\text{null}})}}{D_\sigma \bar{c}_{\sigma,i}^{\text{whole}} + D_{\sigma'} \bar{c}_{\sigma',i}^{\text{whole}} e^{\mp(\eta_f^{E'} - \eta_{\text{null}})}} = \frac{1 - e^{\mp(\eta_f^{E'} - \eta_{\text{null}})}}{r_\sigma^{-1} + e^{\mp(\eta_f^{E'} - \eta_{\text{null}})}} \quad (\text{S1.23b})$$

Now taking their inverses

$$e^{\mp(\eta_f^E - \eta_{\text{null}})} = \frac{1 - r_\sigma^{-1} [c_{\sigma,f}^E - \bar{c}_{\sigma,i}^{\text{whole}}]/\bar{c}_{\sigma,i}^{\text{whole}}}{1 + [c_{\sigma,f}^E - \bar{c}_{\sigma,i}^{\text{whole}}]/\bar{c}_{\sigma,i}^{\text{whole}}} \quad (\text{S1.24a})$$

$$e^{\mp(\eta_f^{E'} - \eta_{\text{null}})} = \frac{1 + r_\sigma^{-1} [c_{\sigma,f}^E - \bar{c}_{\sigma,i}^{\text{whole}}]/\bar{c}_{\sigma,i}^{\text{whole}}}{1 - [c_{\sigma,f}^E - \bar{c}_{\sigma,i}^{\text{whole}}]/\bar{c}_{\sigma,i}^{\text{whole}}} \quad (\text{S1.24b})$$

and combining both expressions

$$e^{\pm(\eta_f^E - \eta_f^{E'})} = \frac{1 + \frac{c_{\sigma,f}^E - \bar{c}_{\sigma,i}^{\text{whole}}}{\bar{c}_{\sigma,i}^{\text{whole}}}}{1 - r_\sigma^{-1} \frac{c_{\sigma,f}^E - \bar{c}_{\sigma,i}^{\text{whole}}}{\bar{c}_{\sigma,i}^{\text{whole}}}} \cdot \frac{1 + r_\sigma^{-1} \frac{c_{\sigma,f}^E - \bar{c}_{\sigma,i}^{\text{whole}}}{\bar{c}_{\sigma,i}^{\text{whole}}}}{1 - \frac{c_{\sigma,f}^E - \bar{c}_{\sigma,i}^{\text{whole}}}{\bar{c}_{\sigma,i}^{\text{whole}}}} \quad (\text{S1.25})$$

leads to

$$e^{\pm(\eta_f^E - \eta_f^{E'})} = \frac{1 + \frac{c_{\sigma,f}^E - \bar{c}_{\sigma,i}^{\text{whole}}}{\bar{c}_{\sigma,i}^{\text{whole}}}}{1 - \frac{c_{\sigma,f}^E - \bar{c}_{\sigma,i}^{\text{whole}}}{\bar{c}_{\sigma,i}^{\text{whole}}}} \cdot \frac{1 + r_\sigma^{-1} \frac{c_{\sigma,f}^E - \bar{c}_{\sigma,i}^{\text{whole}}}{\bar{c}_{\sigma,i}^{\text{whole}}}}{1 - r_\sigma^{-1} \frac{c_{\sigma,f}^E - \bar{c}_{\sigma,i}^{\text{whole}}}{\bar{c}_{\sigma,i}^{\text{whole}}}} \quad (\text{S1.26})$$

after reorganizing the factors.

Finally, by using the hyperbolic identity [22, Eq. (4.37.24)]

$$\operatorname{arctanh} z = \frac{1}{2} \ln \left(\frac{1+z}{1-z} \right) \quad (\text{S1.27})$$

one obtains

$$\begin{aligned} \pm(\eta_f^E - \eta_f^{E'}) &= 2 \operatorname{arctanh} \left(\frac{c_{\sigma,f}^E - \bar{c}_{\sigma,f}^{\text{whole}}}{\bar{c}_{\sigma,f}^{\text{whole}}} \right) \\ &+ 2 \operatorname{arctanh} \left(\frac{D_\sigma \bar{c}_{\sigma,f}^{\text{whole}}}{D_{\sigma'} \bar{c}_{\sigma',f}^{\text{whole}}} \frac{c_{\sigma,f}^E - \bar{c}_{\sigma,f}^{\text{whole}}}{\bar{c}_{\sigma,f}^{\text{whole}}} \right) \end{aligned} \quad (\text{S1.28})$$

which leads to Eq. (2.34b) after applying the relation in Eq. (2.31) $c_{\sigma,f}^E - \bar{c}_{\sigma,f}^{E'} = 2[c_{\sigma,f}^E - \bar{c}_{\sigma,f}^{\text{whole}}]$.

S1.5 Approximations for k_ρ and k'_ρ

S1.5.1 Case of tall cells

Consider first the following approximations when the nome $q = Q(k)$ tends to zero [29, (10.1)–(10.3)]

$$\lim_{q \rightarrow 0^+} \operatorname{sn}(\mathbf{u}, k) = \lim_{q \rightarrow 0^+} \operatorname{sd}(\mathbf{u}, k) = \sin \left(\frac{\pi}{2} \frac{\mathbf{u}}{K(k)} \right) \quad (\text{S1.29a})$$

$$\lim_{q \rightarrow 0^+} \operatorname{cn}(\mathbf{u}, k) = \lim_{q \rightarrow 0^+} \operatorname{cd}(\mathbf{u}, k) = \cos \left(\frac{\pi}{2} \frac{\mathbf{u}}{K(k)} \right) \quad (\text{S1.29b})$$

$$\lim_{q \rightarrow 0^+} \operatorname{dn}(\mathbf{u}, k) = \lim_{q \rightarrow 0^+} \operatorname{nd}(\mathbf{u}, k) = 1 \quad (\text{S1.29c})$$

Since $q_r = Q(k_r) = \exp(-\pi 2H/W)$ in Eq. (2.10b) tends to zero when $H \rightarrow +\infty$, then

$$k_\rho^2 = \frac{4 \operatorname{sn}\left(K(k_r) \frac{g}{W}, k_r\right)}{\left[1 + \operatorname{sn}\left(K(k_r) \frac{g}{W}, k_r\right)\right]^2} \quad (\text{S1.30a})$$

$$k_\rho'^2 = k_r'^4 \frac{\operatorname{sd}\left(K(k_r) \frac{w_A}{W}, k_r\right)^2 \operatorname{sd}\left(K(k_r) \frac{w_B}{W}, k_r\right)^2}{\operatorname{cn}\left(K(k_r) \frac{w_A}{W}, k_r\right)^2 \operatorname{cn}\left(K(k_r) \frac{w_B}{W}, k_r\right)^2} \quad (\text{S1.30b})$$

can be approximated by

$$\lim_{q_r \rightarrow 0^+} k_\rho^2 = \frac{4 \sin\left(\frac{\pi}{2} \frac{g}{W}\right)}{\left[1 + \sin\left(\frac{\pi}{2} \frac{g}{W}\right)\right]^2} \quad (\text{S1.31a})$$

$$\lim_{q_r \rightarrow 0^+} k_\rho'^2 = \tan\left(\frac{\pi}{2} \frac{w_A}{W}\right)^2 \tan\left(\frac{\pi}{2} \frac{w_B}{W}\right)^2 \quad (\text{S1.31b})$$

which leads to Eqs. (2.42).

S1.5.2 Case of shallow cells

Consider the following approximations when the associated nome $q' = Q(k')$ is sufficiently small [29, Eqs. (11.1)–(11.3)]

$$\operatorname{sn}(\mathbf{u}, k) \Big|_{q' \approx 0} \approx (k^2)^{-1/4} \tanh\left(\frac{\pi}{2} \frac{\mathbf{u}}{K'(k)}\right) \quad (\text{S1.32a})$$

$$\operatorname{cn}(\mathbf{u}, k) \Big|_{q' \approx 0} \approx \frac{1}{2} \left(\frac{k'^2}{k^2 q'}\right)^{1/4} \operatorname{sech}\left(\frac{\pi}{2} \frac{\mathbf{u}}{K'(k)}\right) \quad (\text{S1.32b})$$

$$\operatorname{dn}(\mathbf{u}, k) \Big|_{q' \approx 0} \approx \frac{1}{2} \left(\frac{k'^2}{q'}\right)^{1/4} \operatorname{sech}\left(\frac{\pi}{2} \frac{\mathbf{u}}{K'(k)}\right) \quad (\text{S1.32c})$$

also of the subsidiary function $\operatorname{sd} = \operatorname{sn} / \operatorname{dn}$

$$\operatorname{sd}(\mathbf{u}, k) \Big|_{q' \approx 0} \approx 2 \left(\frac{q'}{k^2 k'^2}\right)^{1/4} \sinh\left(\frac{\pi}{2} \frac{\mathbf{u}}{K'(k)}\right) \quad (\text{S1.32d})$$

and of the modulus $(k^2)^{1/4}$ [29, beginning of §7]

$$(k^2)^{1/4} \Big|_{q' \approx 0} \approx \frac{1 - 2q'}{1 + 2q'} = \tanh\left(\frac{\pi}{2} \frac{K(k)}{K'(k)} - \frac{1}{2} \ln 2\right) \quad (\text{S1.32e})$$

Since $q'_r = Q(k'_r) = \exp(-\pi W/2H)$ in Eq. (2.10b) is approximately zero when $H \approx 0$, then k_ρ and k'_ρ in Eqs. (S1.30) can be approximated by

$$k_\rho^2 \Big|_{\substack{q'_r \approx 0 \\ g \approx 0}} \approx 4 \operatorname{sn} \left(K(k_r) \frac{g}{W}, k_r \right) \Big|_{q'_r \approx 0} \approx 4 \frac{\tan \left(\frac{\pi}{2} \frac{K(k_r)}{K'(k_r)} \frac{g}{W} \right)}{\tan \left(\frac{\pi}{2} \frac{K(k_r)}{K'(k_r)} - \ln \sqrt{2} \right)} \quad (\text{S1.33a})$$

$$k'_\rho{}^2 \Big|_{q'_r \approx 0} \approx 16q_r'^2 \sinh \left(\pi \frac{K(k_r)}{K'(k_r)} \frac{w_A}{W} \right)^2 \sinh \left(\pi \frac{K(k_r)}{K'(k_r)} \frac{w_B}{W} \right)^2 \quad (\text{S1.33b})$$

where the last equality was obtained through the identity $2 \sinh(\mathbf{u}) \cosh(\mathbf{u}) = \sinh(2\mathbf{u})$, as shown below for $E \in \{A, B\}$

$$k_r'^2 \frac{\operatorname{sd} \left(K(k_r) \frac{w_E}{W}, k_r \right)^2}{\operatorname{cn} \left(K(k_r) \frac{w_E}{W}, k_r \right)^2} \approx 16q_r'^2 \frac{\sinh \left(\frac{\pi}{2} \frac{K(k_r)}{K'(k_r)} \frac{w_E}{W} \right)^2}{\operatorname{sech} \left(\frac{\pi}{2} \frac{K(k_r)}{K'(k_r)} \frac{w_E}{W} \right)^2} = 4q_r'^2 \sinh \left(\pi \frac{K(k_r)}{K'(k_r)} \frac{w_E}{W} \right)^2 \quad (\text{S1.34})$$

Finally, due to Eqs. (2.10b) and (2.35), that is $K(k_r)/K'(k_r) = -\ln Q(k'_r)/\pi = W/2H$, the desired result in Eqs. (2.44) is obtained.

S2 Numerical calculations

S2.1 Simulations in steady state

S2.1.1 Implementation

A normalized version of the diffusion equation in Eqs. (2.8) was used for the simulations

$$\frac{\partial^2 \xi_{\text{sim}}}{\partial x_{\text{sim}}^2}(x, z) + \frac{\partial^2 \xi_{\text{sim}}}{\partial z_{\text{sim}}^2}(x, z) = 0 \quad (\text{S2.1a})$$

$$\frac{\partial \xi_{\text{sim}}}{\partial x_{\text{sim}}}(0, z) = \frac{\partial \xi_{\text{sim}}}{\partial x_{\text{sim}}}(W, z) = 0, \forall z \in [0, H] \quad (\text{S2.1b})$$

$$\frac{\partial \xi_{\text{sim}}}{\partial z_{\text{sim}}}(x, H) = 0, \forall x \in [0, W] \quad (\text{S2.1c})$$

$$\frac{\partial \xi_{\text{sim}}}{\partial z_{\text{sim}}}(x, 0) = 0, \forall x \notin A \cup B \quad (\text{S2.1d})$$

$$\xi_{\text{sim}}(x, 0) = 0, \forall x \in A \quad (\text{S2.1e})$$

$$\xi_{\text{sim}}(x, 0) = 1, \forall x \in B \quad (\text{S2.1f})$$

where

$$\xi_{\text{sim}} = \frac{c_{\sigma,f} - c_{\sigma,f}^A}{c_{\sigma,f}^B - c_{\sigma,f}^A}, \quad x_{\text{sim}} = \frac{x}{W}, \quad z_{\text{sim}} = \frac{z}{W} \quad (\text{S2.2})$$

The width of each band electrode was taken equal $2w_A = 2w_B = 2w_E$ for all simulations, and different aspect ratios H/W for the unit cell were considered.

An exponential mesh was used to partition the unit cell, in order to keep the memory usage low while maintaining good resolution near the electrode bands (see [38, Chapter 7] for more details on this kind of mesh). The number of elements of the mesh is $n_x \times n_z$, of which their growth factors are $r_x = r_z = r$, and the width and height of its smallest element are $\delta_x = \delta_z = \delta_0$. Additionally, the mesh parameter R is sometimes given, which corresponds to the ratio between the largest ($\delta_0 r^{n_z-1}$) and the smallest (δ_0) elements in the mesh.

S2.1.2 Selection of the parameters for the exponential mesh

Here four cases were considered: $2w_E/W \in \{0.2, 0.4, 0.6, 0.8\}$ with $H/W = 1.0$. The mesh for each case was successively refined until the absolute error between the simulated $\xi_{\text{sim}}(x, z)$ and the theoretical concentration profile $\xi(x, z)$ was less than 0.005 (approximately to two decimal places of accuracy). See *Refinement output of Fig. S2* at the end of this section.

The mesh candidates are shown in Fig. S2. The case for $2w_E/W = 0.8$ is the most restrictive of all, and therefore it requires the finest mesh to reach the desired accuracy. This is because the current flowing in this cell is the highest, due to the largest electrode widths, producing the greatest gradient of concentration among all the cases.

See *Refinement output of Fig. S2* for values of the normalized current $2K'(k_\rho)/K(k_\rho)$. Note that the normalized current has been written in terms of the lattice parameter τ for brevity, that is $-2i\tau = 2K'(k)/K(k)$ due to Eq. [22, (22.2.12)]. The ratio $K'(k_\rho)/K(k_\rho)$ obtained in the simulations was computed numerically using the expression

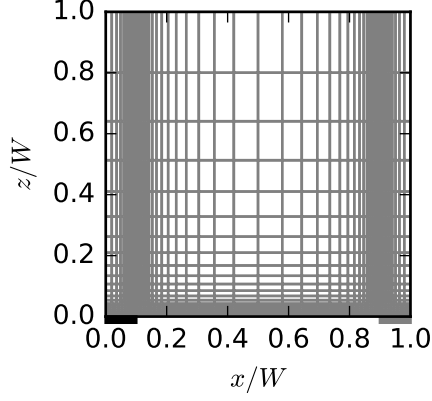
$$-i\tau = \frac{K'(k_\rho)}{K(k_\rho)} = \int_0^{w_A} \frac{\partial \xi}{\partial z} \Big|_{z=0} dx = \int_0^{w_A/W} \frac{\partial \xi_{\text{sim}}}{\partial z_{\text{sim}}} \Big|_{z_{\text{sim}}=0} dx_{\text{sim}} \quad (\text{S2.3})$$

due to Eqs. (2.26), (2.27) and (2.13).

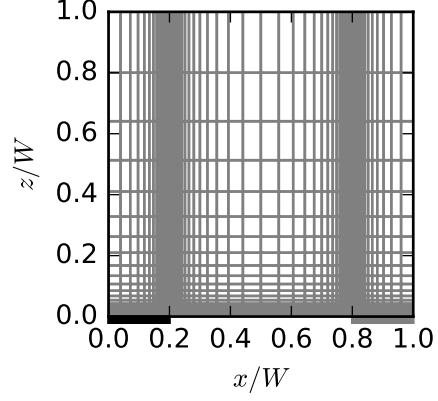
Finally, the parameters of the finest mesh among the candidates in Fig. S2:

$$\delta_0 = 0.000\,25 \text{ and } r = 1.249\,582\,052\,68 \quad (\text{S2.4})$$

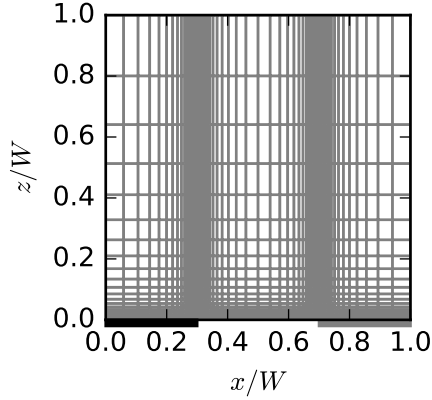
were selected for all the simulations in this report.



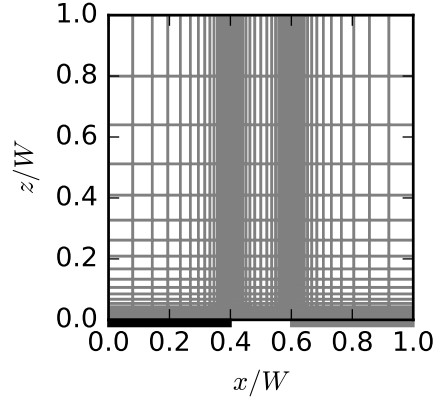
(a) $2w_E/W = 0.2$. Mesh: $\delta_0 = 0.0005$, $r = 1.248\,293\,646\,4$, $n_x \times n_z = 84 \times 28$. Error conc.: ± 0.0039 .



(b) $2w_E/W = 0.4$. Mesh: $\delta_0 = 0.0005$, $r = 1.248\,293\,646\,4$, $n_x \times n_z = 88 \times 28$. Error conc.: ± 0.0040 .



(c) $2w_E/W = 0.6$. Mesh: $\delta_0 = 0.0005$, $r = 1.248\,293\,646\,4$, $n_x \times n_z = 88 \times 28$. Error conc.: ± 0.0046 .



(d) $2w_E/W = 0.8$. Mesh: $\delta_0 = 0.000\,25$, $r = 1.249\,582\,052\,68$, $n_x \times n_z = 96 \times 31$. Error conc.: ± 0.0045 .

Figure S2: Exponential mesh candidates. The size of each mesh is $n_x \times n_z$, the dimensions of its smallest element are $\delta_x = \delta_z = \delta_0$ and the growth factors are $r_x = r_z = r$. The parameters of the finest mesh among the candidates, that is $\delta_0 = 0.000\,25$ and $r = 1.249\,582\,052\,68$, were selected for all simulations in this text.

Refinement output of Fig. S2

numpy: 1.11.0
matplotlib: 1.5.1
fipy: 3.1.3

H/W: 1.0, 2wE/W: 0.2

d0: 0.001
r: 1.24668231916
R: 198.673162644
(nx, nz): (72, 25)
(xi_sim - xi)_min: -0.0055702670935 at (0.8995, 0.0005)
(xi_sim - xi)_max: 0.00557026694512 at (0.1005, 0.0005)
-2itau_sim: 0.614130087454
-2itau_sim + 2itau: -0.0035839696459406859121637690753342364079264758376749102227617713482

d0: 0.0005
r: 1.2482936464
R: 398.613975357
(nx, nz): (84, 28)
(xi_sim - xi)_min: -0.00394025771519 at (0.89975, 0.00025)
(xi_sim - xi)_max: 0.00394025792104 at (0.10025, 0.00025)
-2itau_sim: 0.614628997862
-2itau_sim + 2itau: -0.0030850592382462330833997267239393446690348742751749102227617713482

H/W: 1.0, 2wE/W: 0.4

d0: 0.001
r: 1.24668231916
R: 198.673162644
(nx, nz): (76, 25)
(xi_sim - xi)_min: -0.00566368665462 at (0.7995, 0.0005)
(xi_sim - xi)_max: 0.00566368569237 at (0.2005, 0.0005)
-2itau_sim: 0.85762365783
-2itau_sim + 2itau: -0.0044977238833970306187808518106150001542417595123222092768377380438

d0: 0.0005
r: 1.2482936464
R: 398.613975357
(nx, nz): (88, 28)
(xi_sim - xi)_min: -0.00400968096584 at (0.79975, 0.00025)
(xi_sim - xi)_max: 0.00400968107264 at (0.20025, 0.00025)
-2itau_sim: 0.858133331146
-2itau_sim + 2itau: -0.0039880505674051985422039678186676025645582267974784592768377380438

H/W: 1.0, 2wE/W: 0.6

d0: 0.001
r: 1.24668231916
R: 198.673162644
(nx, nz): (76, 25)
(xi_sim - xi)_min: -0.00654672343082 at (0.6995, 0.0005)
(xi_sim - xi)_max: 0.00654672272843 at (0.3005, 0.0005)
-2itau_sim: 1.1460941062
-2itau_sim + 2itau: -0.006097664237956998989986921071485044556081808580771025801404182422

d0: 0.0005
r: 1.2482936464
R: 398.613975357

```

(nx, nz): (88, 28)
(xi_sim - xi)_min: -0.00463873205874 at (0.69975, 0.00025)
(xi_sim - xi)_max: 0.00463872975751 at (0.30025, 0.00025)
-2itau_sim: 1.14677402693
-2itau_sim + 2itau: -0.005417743508229109240048735511899354057729757799521025801404182422
-----

H/W: 1.0, 2wE/W: 0.8
-----
d0: 0.001
r: 1.24668231916
R: 198.673162644
(nx, nz): (72, 25)
(xi_sim - xi)_min: -0.00899524079541 at (0.5995, 0.0005)
(xi_sim - xi)_max: 0.00899524495282 at (0.4005, 0.0005)
-2itau_sim: 1.60011947532
-2itau_sim + 2itau: -0.0097043377054256020652574316060749899358774808157430304385092440169
-----
d0: 0.0005
r: 1.2482936464
R: 398.613975357
(nx, nz): (84, 28)
(xi_sim - xi)_min: -0.00638554613647 at (0.59975, 0.00025)
(xi_sim - xi)_max: 0.00638554672939 at (0.40025, 0.00025)
-2itau_sim: 1.60142001651
-2itau_sim + 2itau: -0.0084037965092709655845156030424518596143747952688680304385092440169
-----
d0: 0.00025
r: 1.24958205268
R: 799.729964567
(nx, nz): (96, 31)
(xi_sim - xi)_min: -0.00452419661225 at (0.599875, 0.000125)
(xi_sim - xi)_max: 0.00452419959184 at (0.400125, 0.000125)
-2itau_sim: 1.60206219202
-2itau_sim + 2itau: -0.0077616210048388358000111347807219337434794095266805304385092440169
-----

z/W: [ 2.50000000e-04  5.62395513e-04  9.52759340e-04  1.44055097e-03
 2.05008664e-03  2.81175147e-03  3.76351418e-03  4.95281977e-03
 6.43895469e-03  8.29600222e-03  1.06165355e-02  1.35162322e-02
 1.71396412e-02  2.16673880e-02  2.73251792e-02  3.43950535e-02
 4.32294416e-02  5.42687343e-02  6.80632364e-02  8.53005987e-02
 1.06840097e-01  1.33755468e-01  1.67388432e-01  2.09415581e-01
 2.61931951e-01  3.27555465e-01  4.09557431e-01  5.12025615e-01
 6.40068019e-01  8.00067509e-01  1.00000000e+00]

```

S2.1.3 Simulation of concentration profile in Fig. 3

Here a validation is done by comparing the theoretical normalized concentration $\xi(x, z)$ in Eq. (2.17) or (S1.9)

$$\xi(x, z) = \frac{c_{\sigma,f}(x, z) - c_{\sigma,f}^A}{c_{\sigma,f}^B - c_{\sigma,f}^A} = \Re T_r^\rho(x, z) \quad (\text{S2.5})$$

with its simulated counterpart in Eqs. (S2.1) and (S2.2).

The width of each band electrode was taken equal to $2w_A = 2w_B = 0.5W$ for all simulations and three different aspect ratios for the unit cell $H/W \in$

$\{\approx 0.33, \approx 0.51, 1.0\}$ were considered. The parameters used to generate each mesh were obtained from Eq. (S2.4).

The results of the simulations are shown in Fig. S3, of which Fig. 3 shows only a part. In all cases the theoretical concentration $\xi(x, z)$ agrees with the simulations $\xi_{\text{sim}}(x, z)$ up to two decimal places, since the absolute error obtained was not greater than ≈ 0.0030 . The error appears to be greater near the big-sized elements of the mesh, but it actually reaches its extrema at the edges of each electrode band (this is not easy to see from Fig. S3, but was obtained as output data of the simulations, see section *Simulation output* below).

Simulation output

```

numpy:      1.11.0
matplotlib: 1.5.1
fipy:      3.1.3

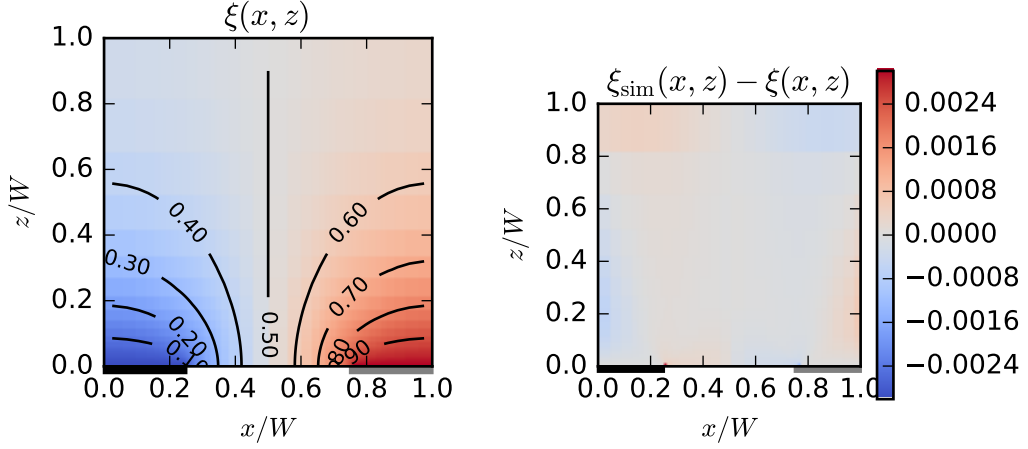
d0: 0.00025
r: 1.24958205268

H/W: 1.0
-----
R: 799.729964567
(nx, nz): (100, 31)
(xi_sim - xi)_min: -0.00300626586786 at (0.749875, 0.000125)
(xi_sim - xi)_max: 0.00300626486245 at (0.250125, 0.000125)
-2itau_sim: 0.992253126221
-2itau_sim + 2itau: -0.00433940282946
-----

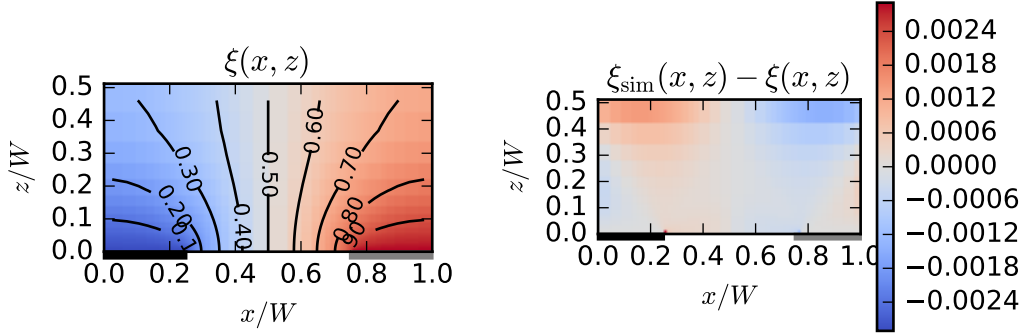
H/W: 0.512025615
-----
R: 409.872737037
(nx, nz): (100, 28)
(xi_sim - xi)_min: -0.00290949376575 at (0.749875, 0.000125)
(xi_sim - xi)_max: 0.00290949208295 at (0.250125, 0.000125)
-2itau_sim: 0.92562204374
-2itau_sim + 2itau: -0.00372746239555
-----

H/W: 0.327555465
-----
R: 262.494055937
(nx, nz): (100, 26)
(xi_sim - xi)_min: -0.0027092884472 at (0.749875, 0.000125)
(xi_sim - xi)_max: 0.00270929214004 at (0.250125, 0.000125)
-2itau_sim: 0.788457932688
-2itau_sim + 2itau: -0.00252385445816
-----

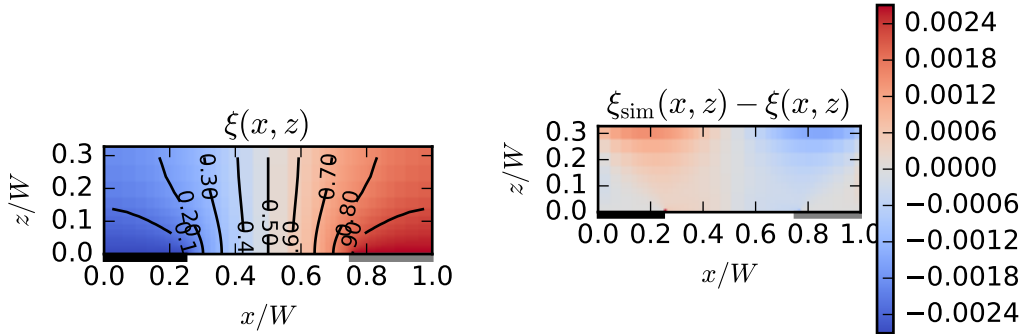
```



(a) $H/W = 1$. Mesh: 100×31 . Error max/min: $\approx \pm 0.0030$.



(b) $H/W \approx 0.5$. Mesh: 100×28 . Error. max/min: $\approx \pm 0.0029$.



(c) $H/W \approx 0.3$. Mesh: 100×26 . Error. max/min: $\approx \pm 0.0027$.

Figure S3: Left column: Normalized concentration $\xi(x, z) = [c_{\sigma,f}(x, z) - c_{\sigma,f}^A]/[c_{\sigma,f}^B - c_{\sigma,f}^A]$ in the final steady state (isoconcentration lines shown in black). Right column: Error between simulation and theoretical concentration $\xi_{\text{sim}}(x, z) - \xi(x, z)$. Plots consider electrodes of equal size $2w_A = 2w_B = 0.5W$ and different aspect ratios H/W for the unit cell. The simulations were obtained by numerically solving Eqs. (S2.1) in steady state.


```

# mesh size (nx, nz)
#
# H/W \ 2*wE/W: [ 0.2  0.4  0.5  0.6  0.8]
0.054269 (96, 18) (100, 18) (100, 18) (100, 18) (96, 18)
0.106840 (96, 21) (100, 21) (100, 21) (100, 21) (96, 21)
0.209416 (96, 24) (100, 24) (100, 24) (100, 24) (96, 24)
0.327555 (96, 26) (100, 26) (100, 26) (100, 26) (96, 26)
0.409557 (96, 27) (100, 27) (100, 27) (100, 27) (96, 27)
0.640068 (96, 29) (100, 29) (100, 29) (100, 29) (96, 29)
0.800068 (96, 30) (100, 30) (100, 30) (100, 30) (96, 30)
1.000000 (96, 31) (100, 31) (100, 31) (100, 31) (96, 31)
1.249832 (96, 32) (100, 32) (100, 32) (100, 32) (96, 32)

```

Table S1: Mesh sizes $n_x \times n_z$ obtained using the mesh parameters in Eq. (S2.4) for different values of H/W and $2w_E/W$.

```

# values of (xi_sim - xi)_min
#
# H/W \ 2*wE/W: [ 0.2  0.4  0.5  0.6  0.8]
0.054269 0.000017 -0.014094 -0.001479 -0.001883 -0.003391
0.106840 -0.001380 -0.001700 -0.001980 -0.002375 -0.003974
0.209416 -0.001959 -0.002163 -0.002430 -0.002818 -0.004316
0.327555 -0.002372 -0.002486 -0.002709 -0.003051 -0.004430
0.409557 -0.002537 -0.002621 -0.002824 -0.003141 -0.004467
0.640068 -0.002731 -0.002788 -0.002964 -0.003251 -0.004511
0.800068 -0.002770 -0.002822 -0.002994 -0.003274 -0.004520
1.000000 -0.002787 -0.002837 -0.003006 -0.003284 -0.004524
1.249832 -0.002792 -0.002842 -0.003011 -0.003287 -0.004526

```

(a) Minimum error between normalized concentrations: $\min \xi_{\text{sim}}(x, z) - \xi(x, z)$.

```

# values of (xi_sim - xi)_max
#
# H/W \ 2*wE/W: [ 0.2  0.4  0.5  0.6  0.8]
0.054269 0.999983 0.019672 0.001536 0.001876 0.003376
0.106840 0.001379 0.001700 0.001980 0.002375 0.003974
0.209416 0.001959 0.002163 0.002430 0.002818 0.004316
0.327555 0.002372 0.002486 0.002709 0.003051 0.004430
0.409557 0.002537 0.002621 0.002824 0.003141 0.004467
0.640068 0.002731 0.002788 0.002964 0.003251 0.004511
0.800068 0.002770 0.002822 0.002994 0.003274 0.004520
1.000000 0.002787 0.002837 0.003006 0.003284 0.004524
1.249832 0.002792 0.002842 0.003011 0.003287 0.004526

```

(b) Maximum error between normalized concentrations: $\max \xi_{\text{sim}}(x, z) - \xi(x, z)$.

Table S2: Error between simulated and theoretical concentrations obtained when simulating exhaustively for different values of H/W and $2w_E/W$.

S2.1.4 Exhaustive simulations

The normalized concentration profile $\xi(x, z)$ and current $2K'(k_\rho)/K(k_\rho)$ were exhaustively simulated for all combinations of the following electrode widths

$$\frac{2w_E}{W} = \{0.2, 0.4, 0.5, 0.6, 0.8\} \quad (\text{S2.6})$$

and aspect ratios

$$\frac{H}{W} \approx \{0.05, 0.11, 0.21, 0.33, 0.41, 0.64, 0.80, 1.00, 1.25\} \quad (\text{S2.7})$$

The implementation in Eqs. (S2.1) was used, together with the meshes specified in Table S1 and the selected mesh parameters in Eq. (S2.4). These simulations were contrasted against their theoretical counterparts, and the results are shown in Tables S2, S3 and in Fig. 5.

Table S2 shows that the minimum and maximum errors between the simulated and theoretical concentration profile were not greater than ≈ 0.0045 , except for the two first band widths when $H/W \approx 0.05$.

Table S3 shows the simulated values of the normalized current and the error with respect to its theoretical counterpart, which was not greater than ≈ 0.0051 for most of the cases (except for the case $H/W \approx 0.05$ and $2w_E/W = 0.2$ with an error of ≈ 0.1279 , and for the last six aspect ratios H/W when $2w_E/W = 0.8$ with an error not greater than ≈ 0.0078).

Table S4 shows exhaustive simulations of the normalized limiting current (case of internal counter electrode) obtained in [19, Fig. 7]. In order to compare the results in Table S4 against the normalized current of this text (Eq. (2.24))

$$\left| \frac{i_f^E/L}{Fn_e \cdot 2D_\lambda \bar{c}_{\lambda,i}^{\text{whole}}} \right| = 2 \frac{K'(k_\rho)}{K(k_\rho)} \quad (\text{S2.8})$$

($D_\lambda |c_{\lambda,f}^E - c_{\lambda,f}^{E'}| = 2D_\lambda \bar{c}_{\lambda,i}^{\text{whole}}$ for the limiting current case, see Eq. (2.32)) the average flux [19, $\bar{\phi}_\lambda^{\text{lim}}$] was related to the current per electrode band $i_f^E = Fn_e \bar{\phi}_\lambda^{\text{lim}} 2w_E L$, and then replaced in the expression of [19, Fig. 7a]

$$\left| \frac{\bar{\phi}_\lambda^{\text{lim}} w_E}{\pi^2 D_\lambda \bar{c}_{\lambda,i}^{\text{whole}}} \right| = \frac{1}{\pi^2} \left| \frac{i_f^E/L}{Fn_e \cdot 2D_\lambda \bar{c}_{\lambda,i}^{\text{whole}}} \right| = \frac{1}{\pi^2} \cdot 2 \frac{K'(k_\rho)}{K(k_\rho)} \quad (\text{S2.9})$$

showing that both normalized currents are related by a factor of $\pi^2 \approx 10$. After scaling by this factor, one can see the agreements between Tables S3 and S4. See Fig. 5 for a graphical representation of both tables.

```

# values of 2K'(k_rho)/K(k_rho)_sim
#
# H/W \ 2*wE/W: [ 0.2  0.4  0.5  0.6  0.8]
0.054269 0.127893 0.167383 0.197903 0.242036 0.436878
0.106840 0.236720 0.307210 0.358978 0.431529 0.724088
0.209416 0.397250 0.523456 0.604589 0.710782 1.087271
0.327555 0.506054 0.683877 0.788458 0.917149 1.332990
0.409557 0.549094 0.751141 0.866497 1.004927 1.435700
0.640068 0.600287 0.834122 0.963650 1.114661 1.563992
0.800068 0.610578 0.851204 0.983779 1.137483 1.590754
1.000000 0.614875 0.858382 0.992253 1.147105 1.602062
1.249832 0.616250 0.860685 0.994976 1.150200 1.605708

```

(a) Normalized current $2K'(k_\rho)/K(k_\rho)_{\text{sim}}$ obtained through simulations.

```

# values of 2K'(k_rho)/K(k_rho)_sim - 2K'(k_rho)/K(k_rho)
#
# H/W \ 2*wE/W: [ 0.2  0.4  0.5  0.6  0.8]
0.054269 0.127893 0.000115 -0.000196 -0.000293 -0.000960
0.106840 -0.000261 -0.000389 -0.000524 -0.000750 -0.002111
0.209416 -0.000831 -0.001115 -0.001411 -0.001869 -0.004090
0.327555 -0.001570 -0.002072 -0.002524 -0.003168 -0.005837
0.409557 -0.001994 -0.002637 -0.003162 -0.003879 -0.006672
0.640068 -0.002648 -0.003513 -0.004119 -0.004891 -0.007687
0.800068 -0.002793 -0.003695 -0.004304 -0.005068 -0.007800
1.000000 -0.002839 -0.003740 -0.004339 -0.005087 -0.007762
1.249832 -0.002837 -0.003725 -0.004314 -0.005049 -0.007690

```

(b) Error between normalized currents: $2K'(k_\rho)/K(k_\rho)_{\text{sim}} - 2K'(k_\rho)/K(k_\rho)$.

Table S3: Error between simulated and theoretical currents obtained when simulating exhaustively for different values of H/W and $2w_E/W$.

```

# simulation data used in [Fig. 7a, GuajardoYevenes2013sep]
# https://doi.org/10.1016/j.jelechem.2013.07.014
# https://arxiv.org/abs/1602.06428
#
# values of 2/pi^2 K'(k_rho)/K(k_rho)_sim
# horizontal: H/W = [0.2/pi, 0.4/pi, 0.6/pi, 0.8/pi,
#                   1/pi, 2/pi, 3/pi, 4/pi, 5/pi]
# vertical: 2wE/W = [0.2, 0.4, 0.6, 0.8]
#
0.01414 0.02652 0.03628 0.04353 0.04873 0.05864 0.06007 0.06026 0.06029
0.01845 0.03458 0.04792 0.05844 0.06636 0.08236 0.08475 0.08508 0.08513
0.0265 0.04817 0.06546 0.07902 0.08932 0.11050 0.11373 0.11417 0.11424
0.04729 0.07909 0.10152 0.11807 0.13031 0.15522 0.15926 0.15954 0.15962

```

Table S4: Normalized currents $2/\pi^2 K'(k_\rho)/K(k_\rho)_{\text{sim}}$ obtained in [19, Fig. 7a] by simulating exhaustively for different values of H/W and $2w_E/W$.

```

# 16 points per curve
# simulation data obtained from [Fig. 7a, Strutwolf2005feb]
# https://doi.org/10.1002/elan.200403112
#
# for 2wE = 0.5 g      | for 2wE = g
# 2wE/H      Gss: 2K'/K | 2wE/H      Gss: 2K'/K
0.25932504  0.7799733   0.25932504  0.99572764
0.49023091  0.76608812   0.49023091  0.98931909
0.72468917  0.71268358   0.72468917  0.97222964
0.95914742  0.64218959   0.95914742  0.93164219
1.19005329  0.57276368   1.19360568  0.87503338
1.42095915  0.51401869   1.42451155  0.81201602
1.65541741  0.46275033   1.6589698   0.75113485
1.88987567  0.41895861   1.89342806  0.69666222
2.12433393  0.38157543   2.12788632  0.64966622
2.35523979  0.35166889   2.35879218  0.60694259
2.58969805  0.32603471   2.59325044  0.56849132
2.82415631  0.30253672   2.8277087   0.53431242
3.05861456  0.28331108   3.06216696  0.50226969
3.28952043  0.26515354   3.29307282  0.47449933
3.52397869  0.25020027   3.52753108  0.44779706
3.75843694  0.23631509   3.76198934  0.42643525

```

Table S5: Normalized currents $2K'(k_\rho)/K(k_\rho)_{\text{sim}}$ obtained in [18, Fig. 7a] by simulating for different values of $2w_E/H$ and $2w_E/g \in \{0.5, 1\}$.

Table S5 shows simulations of the normalized limiting current (case of external counter electrode) obtained in [18, Fig. 7a]. In order to compare against the normalized current of this text (Eq. (2.24))

$$\left| \frac{i_f^E/L}{Fn_e \cdot [D_\sigma \bar{c}_{\sigma,i}^{\text{whole}} + D_{\sigma'} \bar{c}_{\sigma',i}^{\text{whole}}]} \right| = 2 \frac{K'(k_\rho)}{K(k_\rho)} \quad (\text{S2.10})$$

($D_\sigma |c_{\sigma,f}^E - c_{\sigma,f}^{E'}| = D_\sigma \bar{c}_{\sigma,i}^{\text{whole}} + D_{\sigma'} \bar{c}_{\sigma',i}^{\text{whole}}$, see Eq. (2.28) when $\pm\eta^E \rightarrow +\infty$ for the limiting current case) the expressions for [18, G_g and G_c in p. 171] were rewritten using the notation of this text

$$|G_E| = \left| \frac{N_E i_f^E}{LN_E n_e F [D_\sigma \bar{c}_{\sigma,i}^{\text{whole}} + D_{\sigma'} \bar{c}_{\sigma',i}^{\text{whole}}]} \right| = 2 \frac{K'(k_\rho)}{K(k_\rho)} \quad (\text{S2.11})$$

were the normalized current at the generator G_g and collector G_c have equal magnitude (but opposite sign) in steady state $|G_{ss}| = |G_g| = |G_c| =: |G_E|$. For plotting the data of [18, Fig. 7a] in Fig. 5, the horizontal variable [18, w_e/h_c in Fig. 7a] was also rewritten according to the notation of this text, that is $2w_E/H$ in Table S5, and later related to H/W by

$$\frac{H}{W} = \left[\frac{2w_E}{H} \cdot \left(\frac{g}{2w_E} + \frac{2w_E}{2w_E} \right) \right]^{-1} \quad (\text{S2.12})$$

where g is the gap between electrodes of equal width, such that $W = 2w_E + g$. Only the data for the case $2w_E = g$ ($2w_E/W = 0.5$) was plotted in Fig. 5, which agrees with its theoretical counterpart.

S2.2 Direct evaluations and curve fitting

S2.2.1 Voltammogram and potentials in Figs. 8a and 8b

Fig. 8a was generated from Eq. (2.34b) with $r_\lambda = (D_{\lambda'} \bar{c}_{\lambda',i}^{\text{whole}})/(D_\lambda \bar{c}_{\lambda,i}^{\text{whole}})$

$$\pm(\eta_f^E - \eta_f^{E'}) = 2 \operatorname{arctanh} \left(\frac{c_{\lambda,f}^E - c_{\lambda,f}^{E'}}{2\bar{c}_{\lambda,i}^{\text{whole}}} \right) + 2 \operatorname{arctanh} \left(\frac{1}{r_\lambda} \cdot \frac{c_{\lambda,f}^E - c_{\lambda,f}^{E'}}{2\bar{c}_{\lambda,i}^{\text{whole}}} \right) \quad (\text{S2.13})$$

by evaluating several points for $[c_{\lambda,f}^E - c_{\lambda,f}^{E'}]/2\bar{c}_{\lambda,i}^{\text{whole}} \in]-1, 1[$, and obtaining a list of points for $\pm(\eta_f^E - \eta_f^{E'})$.

The same list of points $[c_{\lambda,f}^E - c_{\lambda,f}^{E'}]/2\bar{c}_{\lambda,i}^{\text{whole}} \in]-1, 1[$ was evaluated in Eqs. (S1.24)

$$e^{\mp(\eta_f^E - \eta_{\text{null}})} = \frac{1 - r_\sigma^{-1} [c_{\sigma,f}^E - \bar{c}_{\sigma,i}^{\text{whole}}]/\bar{c}_{\sigma,i}^{\text{whole}}}{1 + [c_{\sigma,f}^E - \bar{c}_{\sigma,i}^{\text{whole}}]/\bar{c}_{\sigma,i}^{\text{whole}}} \quad (\text{S2.14a})$$

$$e^{\mp(\eta_f^{E'} - \eta_{\text{null}})} = \frac{1 + r_\sigma^{-1} [c_{\sigma,f}^E - \bar{c}_{\sigma,i}^{\text{whole}}]/\bar{c}_{\sigma,i}^{\text{whole}}}{1 - [c_{\sigma,f}^E - \bar{c}_{\sigma,i}^{\text{whole}}]/\bar{c}_{\sigma,i}^{\text{whole}}} \quad (\text{S2.14b})$$

obtaining one list of points for $\mp(\eta_f^E - \eta_{\text{null}})$ and another list of points for $\mp(\eta_f^{E'} - \eta_{\text{null}})$. Both of them were plotted against the list of points for $\pm(\eta_f^E - \eta_f^{E'})$ resulting in Fig. 8b.

S2.2.2 Curve fitting in Fig. 9

The data used for curve fitting in Fig. 9a was obtained from [8, Fig. 7], from which 16 data points for each curve (generator and collector) were extracted. The extracted data is shown in Table S6.

Similarly, the data used for curve fitting in Fig. 9b was obtained from [35, Fig. 2], or equivalently [25, 3.12], from which 16 data points were extracted. The extracted data is shown in Table S7.

S2.2.3 Approximated normalized current in Figs. 10 and 11.

The relative error between the approximated and exact currents, \tilde{i}_f^E and i_f^E , corresponds to that between its normalized counterparts

$$\text{relative error} = \frac{\tilde{i}_f^E}{i_f^E} - 1 = \left[2 \frac{K'(k_\rho)}{K(k_\rho)} \right]_{\text{app.}} \left[2 \frac{K'(k_\rho)}{K(k_\rho)} \right]^{-1} - 1 \quad (\text{S2.15})$$

```

# 16 points per curve
# experimental data obtained from [Fig. 7, Aoki1988dec]
# https://doi.org/10.1016/0022-0728(88)87003-7
#
# E: collector      | E: generator
# VfE - VR        NE ifE | VfE - VR        NE ifE
# /V              /uA   | /V              /uA
0.2037931        0.51457195   | 0.62310345     34.67668488
0.26724138      0.37340619   | 0.53758621     33.9708561
0.29482759     -0.33242259   | 0.51551724     32.7003643
0.32241379     -1.17941712   | 0.48241379     30.30054645
0.35827586     -2.87340619   | 0.44931034     27.75956284
0.37758621     -6.12021858   | 0.43827586     25.35974499
0.39137931     -9.36703097   | 0.44103448     22.95992714
0.40517241    -12.75500911   | 0.43275862     20.56010929
0.41896552    -16.00182149   | 0.41068966     18.01912568
0.43           -19.24863388   | 0.40241379     15.61930783
0.44655172    -22.63661202   | 0.40793103     13.21948998
0.46310345    -25.88342441   | 0.39965517     10.81967213
0.49068966    -28.70673953   | 0.37482759     8.27868852
0.50724138    -29.97723133   | 0.3637931      5.87887067
0.55965517    -30.82422587   | 0.36655172     3.47905282
0.59          -31.38888889   | 0.30586207     1.22040073

```

Table S6: Voltammogram data of 1 nmol μl^{-1} ferrocene with $V_f^{E'} - V^R = -0.15$ V from [8, Fig. 7] for generator and collector. Here V^R is the potential of the reference electrode (saturated calomel electrode).

```

# 16 points per curve
# experimental data obtained from [Fig. 2, Rahimi2011]
# https://doi.org/10.1021/ac2012703
# or equivalently from [Fig. 3.12, Rahimi2009]
# https://hdl.handle.net/10012/4555
#
# VfE - VfE'      NE ifE
# /V              /uA
-0.39557823     0.5061263
-0.35578231     0.49877474
-0.2914966      0.49255419
-0.20612245     0.4801131
-0.13163265     0.42808671
-0.07278912     0.29406221
-0.03979592     0.16512724
-0.02006803     0.08369463
0.00170068     -0.02035815
0.02380952     -0.12441093
0.0452381      -0.22846371
0.07653061     -0.33251649
0.1329932      -0.43317625
0.18265306     -0.47502356
0.27823129     -0.48633365
0.29489796     -0.49198869

```

Table S7: Voltammogram data of 0.20 nmol μl^{-1} of each ferrocyanide and ferricyanide from [35, Fig. 2], or equivalently from [25, Fig. 3.12].

For this reason, it suffices for Figs. 10 and 11 to show the approximated version of the normalized current $2K'(k_\rho)/K(k_\rho)$, together with its relative error with respect to the exact value, for tall and shallow cells respectively.

The combinations of $(2w_E/H, H/W)$ that produce a relative error less than $\pm 0.05 = \pm 5\%$ were considered to define regions where the approximations are valid. These correspond to $2w_E/W > 0.46$ (large electrodes) and $2w_E/W < 0.56$ (small electrodes) for the case of tall cells $H/W > 1$. In the case of shallow cells $H/W \leq 1$, these regions of validity correspond to the right of the line connecting $(1, 0) \rightarrow (0.28, 1)$ (large electrodes) and to the left of the line connecting $(1, 0) \rightarrow (0.36, 1)$ (small electrodes). See *Output of Figs. 10 and 11* at the following subsection for numerical results. The combinations of $(2w_E/H, H/W)$ that produce a relative error of $\pm 0.005 = \pm 0.5\%$ are also given as a reference in subsection *Output of Figs. 10 and 11*.

When expressing the ratio $K'(k)/K(k)$ (which is involved in the relative error) in terms of the nome function $Q(k)$, or equivalently $Q(k')$

$$\frac{K'(k)}{K(k)} = \frac{\ln Q(k)}{-\pi} = \frac{-\pi}{\ln Q(k')} \quad (\text{S2.16})$$

one can realize that the approximations in Eqs. (2.43) and (2.45)

$$\left[\frac{K'(k_\rho)}{K(k_\rho)} \right]_{\text{app.}} := \begin{cases} \frac{\ln \tilde{Q}(\tilde{k}_\rho)}{-\pi}, & \text{for } k_\rho \approx 0 \\ \frac{-\pi}{\ln \tilde{Q}(\tilde{k}'_\rho)}, & \text{for } k'_\rho \approx 0 \end{cases} \quad (\text{S2.17})$$

are due to a two-step approximation process: First, approximation of the nome function by

$$\tilde{Q}(k) := \frac{k^2}{16} \quad (\text{S2.18})$$

and later, the approximations of the moduli \tilde{k}_ρ and \tilde{k}'_ρ , which are given in Eqs. (2.42) and (2.44) in the main text.

Therefore, it is possible to analyze the propagation of the relative error, for $k_\rho \approx 0$, by looking at the following total ratio

$$\left[\frac{K'(k_\rho)}{K(k_\rho)} \right]_{\text{app.}} \left[\frac{K'(k_\rho)}{K(k_\rho)} \right]^{-1} = \frac{\ln \tilde{Q}(\tilde{k}_\rho)}{\ln Q(k_\rho)} = \frac{\ln \tilde{Q}(\tilde{k}_\rho) \ln \tilde{Q}(k_\rho)}{\ln \tilde{Q}(k_\rho) \ln Q(k_\rho)} \quad (\text{S2.19})$$

where a relative error of $\pm 0.05 = \pm 5\%$ corresponds to the total ratios 0.95 and 1.05. The ratios $\ln \tilde{Q}(k_\rho)/\ln Q(k_\rho)$ and $\ln \tilde{Q}(\tilde{k}_\rho)/\ln \tilde{Q}(k_\rho)$ show the individual contributions of the approximated nome \tilde{Q} and the approximated

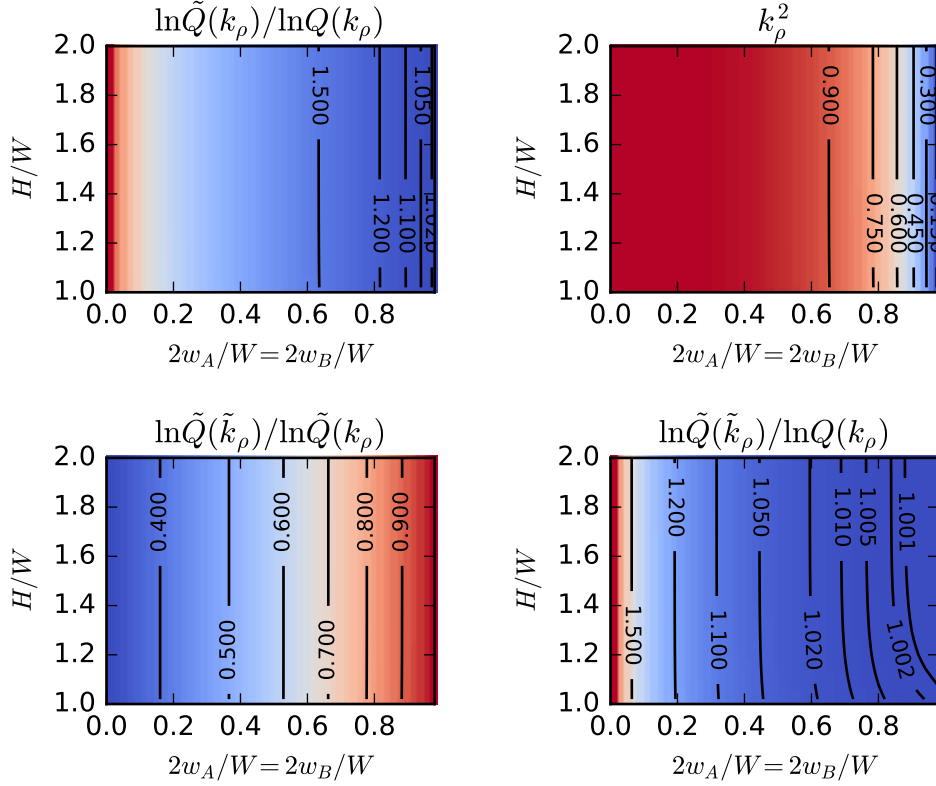


Figure S4: Propagation of the ratio of approximation $\ln \tilde{Q}(\tilde{k}_\rho)/\ln Q(k_\rho)$ for the case of tall cells and large electrodes. Contour lines of selected values are shown in black.

modulus \tilde{k}_ρ to the total ratio $\ln \tilde{Q}(\tilde{k}_\rho)/\ln Q(k_\rho)$, and therefore, to the relative error.

This is shown in Fig. S4 for the case of tall cells and large electrodes. The first ratio $\ln \tilde{Q}(k_\rho)/\ln Q(k_\rho) < 1.05$ (relative error of 5%) for widths $2w_E/W > 0.94$ ($k_\rho^2 \lesssim 0.314$), which corresponds to very extreme cases of wide electrodes. This agrees with the relative error of $\approx 4\%$ in [8, before Eq. (32)] when approximating only the nome function $\tilde{Q}(k_\rho)$ for gap widths $g/W < 0.059 \Leftrightarrow 2w_E/W > 0.941$ ($k_\rho^2 < 0.310$). Fortunately, the contribution due to the approximation of the modulus \tilde{k}_ρ makes the second ratio $\ln \tilde{Q}(\tilde{k}_\rho)/\ln \tilde{Q}(k_\rho) < 1$ in almost the whole domain $(2w_E/W, H/W)$. This helps to extend the region where the total ratio $\ln \tilde{Q}(\tilde{k}_\rho)/\ln Q(k_\rho) < 1.05$ (relative error less than 5%), which corresponds to more reasonable electrode widths $2w_E/W < 0.46$.

A similar analysis of the propagation of the relative error can be done for

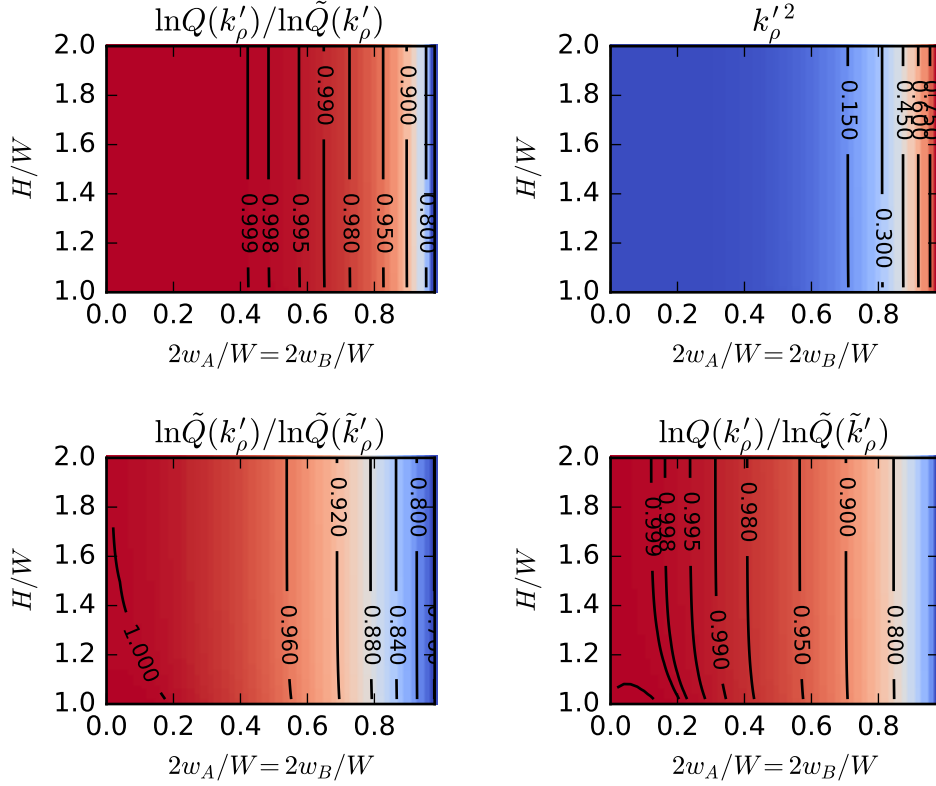


Figure S5: Propagation of the ratio of approximation $\ln \tilde{Q}(\tilde{k}'_\rho)/\ln Q(k'_\rho)$ for the case of tall cells and small electrodes. Contour lines of selected values are shown in black.

$k'_\rho \approx 0$ when considering the following total ratio

$$\left[\frac{K'(k_\rho)}{K(k_\rho)} \right]_{\text{app.}} \left[\frac{K'(k_\rho)}{K(k_\rho)} \right]^{-1} = \frac{\ln Q(k'_\rho)}{\ln \tilde{Q}(\tilde{k}'_\rho)} = \frac{\ln \tilde{Q}(k'_\rho)}{\ln \tilde{Q}(\tilde{k}'_\rho)} \frac{\ln Q(k'_\rho)}{\ln \tilde{Q}(k'_\rho)} \quad (\text{S2.20})$$

where the ratios $\ln Q(k'_\rho)/\ln \tilde{Q}(k'_\rho)$ and $\ln \tilde{Q}(k'_\rho)/\ln \tilde{Q}(\tilde{k}'_\rho)$ show the individual contributions of the approximated nome \tilde{Q} and the approximated complementary modulus \tilde{k}'_ρ to the total ratio $\ln Q(k'_\rho)/\ln \tilde{Q}(\tilde{k}'_\rho)$, and therefore, to the relative error.

This is shown in Fig. S5 for the case of tall cells and small electrodes. Unlike the previous case, the first ratio $\ln Q(k'_\rho)/\ln \tilde{Q}(k'_\rho) > 0.95$ (relative error of -5%) for widths $2w_E/W < 0.82$ ($k'^2_\rho \lesssim 0.315$), which corresponds to a large portion of the parameter domain. This agrees with the statement in [10, before Eq. (5)], which says that the approximation converges rapidly

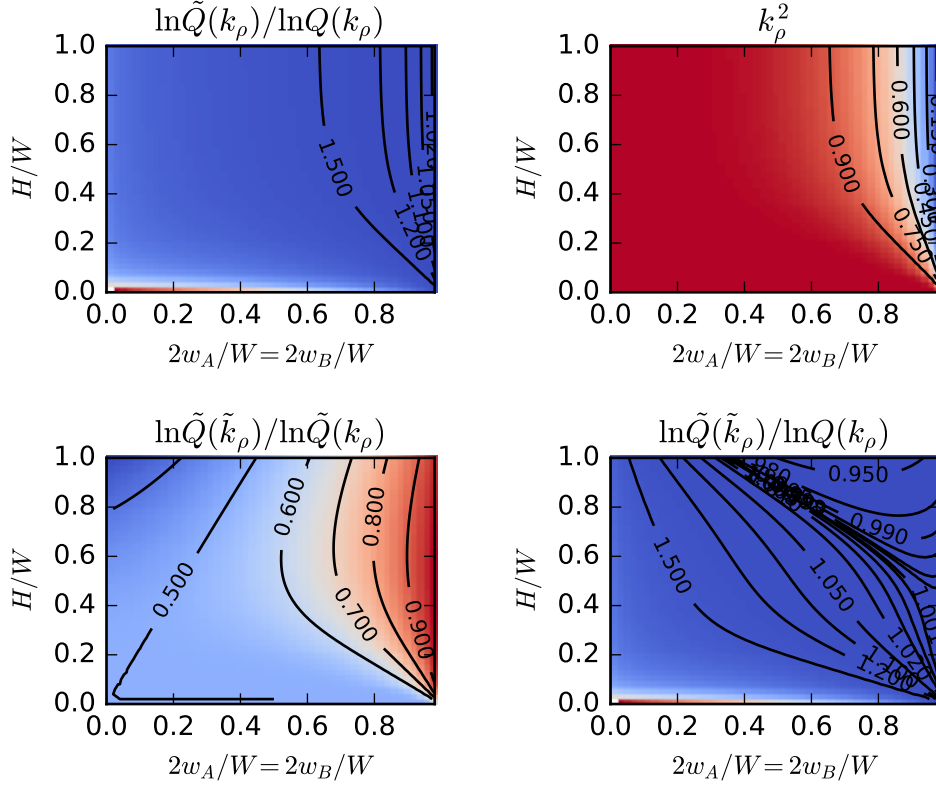


Figure S6: Propagation of the ratio of approximation $\ln \tilde{Q}(\tilde{k}_\rho)/\ln Q(k_\rho)$ for the case of shallow cells and large electrodes. Contour lines of selected values are shown in black.

for gap widths $g > 0.1 \cdot 2w_E \Leftrightarrow 2w_E/W < 0.909$ (no quantitative error is specified). Unfortunately, the contribution due to the approximation of the complementary modulus \tilde{k}'_ρ makes the second ratio $\ln \tilde{Q}(k'_\rho)/\ln \tilde{Q}(\tilde{k}'_\rho) < 1$ in most of the domain $(2w_E/W, H/W)$. This approximation helps to simplify the expression for the complementary modulus in Eq. (2.42b) at the expense of shrinking the domain where $\ln Q(k'_\rho)/\ln \tilde{Q}(\tilde{k}'_\rho) > 0.95$ (relative error of approximation less than -5%), which corresponds to electrode widths $2w_E/W \lesssim 0.56$.

The propagation of the relative error for cases of shallow cells have not been reported previously in the literature and they are given below as a reference.

Fig. S6 shows the propagation of the total ratio, in Eq. (S2.19), for the case of shallow cells and large electrodes. The first ratio $\ln \tilde{Q}(k_\rho)/\ln Q(k_\rho) < 1.05$ (relative error of 5%) for combinations of $(2w_E/W, H/W)$ roughly to the

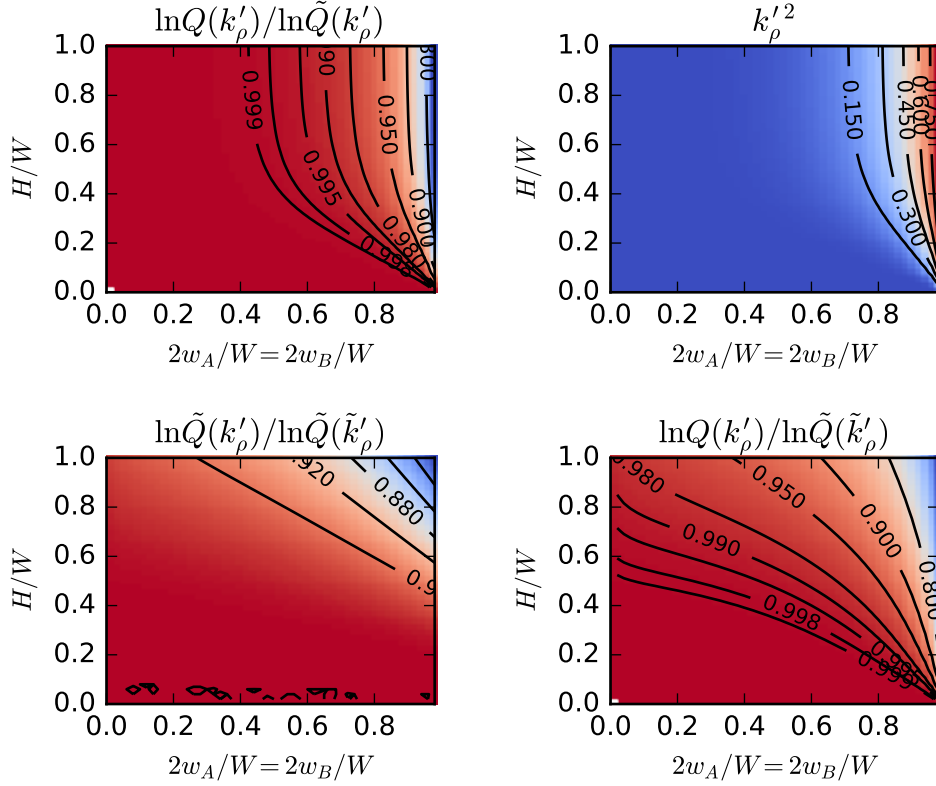


Figure S7: Propagation of the ratio of approximation $\ln \tilde{Q}(k'_\rho)/\ln Q(k_\rho)$ for the case of shallow cells and small electrodes. Contour lines of selected values are shown in black.

right of the line joining the points $(1, 0) \rightarrow (0.94, 1)$ ($k_\rho^2 \lesssim 0.316$), which again correspond to very wide electrodes. The contribution due to the approximation of the modulus \tilde{k}_ρ makes the second ratio $\ln \tilde{Q}(\tilde{k}_\rho)/\ln \tilde{Q}(k_\rho) < 1$ in most of the domain $(2w_E/W, H/W)$. This also extends the region where the total ratio $0.95 < \ln \tilde{Q}(\tilde{k}_\rho)/\ln Q(k_\rho) < 1.05$ (relative error less than $\pm 5\%$), which corresponds to combinations of $(2w_E/W, H/W)$ approximately at the right of the line joining the points $(1, 0) \rightarrow (0.28, 1)$.

Fig. S7 shows the propagation of the total ratio, in Eq. (S2.20), for the case of shallow cells and small electrodes. The first ratio $\ln Q(k'_\rho)/\ln \tilde{Q}(k'_\rho) > 0.95$ (relative error of -5%) for combinations of $(2w_E/W, H/W)$ roughly to the left of the line joining the points $(1, 0) \rightarrow (0.82, 1)$ ($k'_\rho{}^2 \lesssim 0.315$), which corresponds to a large portion of the parameter domain. The approximation of the complementary modulus \tilde{k}'_ρ makes the second ratio $\ln \tilde{Q}(k'_\rho)/\ln \tilde{Q}(\tilde{k}'_\rho) < 1$ in most of the domain $(2w_E/W, H/W)$. This approximation helps to sim-

plify the expression for the complementary modulus in Eq. (2.42b) at the expense of shrinking the domain where $\ln Q(k'_\rho)/\ln \tilde{Q}(\tilde{k}'_\rho) > 0.95$ (relative error of approximation less than -5%), which corresponds to combinations of $(2w_E/W, H/W)$ approximately at the left of the line joining the points $(1, 0) \rightarrow (0.36, 1)$.

Output of Figs. 10 and 11

```
mpmath:      0.19
numpy:       1.11.0
matplotlib:  1.5.1
```

H/W: tall, 2wE/W: large

```
-----
error < +-5.0%: [  4.89246306e-02  4.39635532e-02  3.94513927e-02  3.53466127e-02
  3.16126327e-02  2.82170766e-02  2.51311534e-02  2.23291461e-02
  1.97879836e-02  1.74868819e-02  1.54070399e-02  1.35313795e-02
  1.18443217e-02  1.03315920e-02  8.98004862e-03  7.77752814e-03
  6.71270414e-03  5.77495248e-03  4.95421687e-03  4.24086520e-03
  3.62552072e-03  3.09883913e-03  2.65117058e-03  2.27196010e-03
  1.94846970e-03  1.66230242e-03  1.37515620e-03  1.16230242e-03
  4.08347283e-02  3.63337276e-02  3.22437476e-02  2.85282641e-02
  2.51549557e-02  2.20950872e-02  1.93229978e-02  1.68156760e-02
  1.45524017e-02  1.25144444e-02  1.06848066e-02  9.04800381e-03
  7.58987477e-03  6.29741706e-03  5.15864251e-03  4.16244923e-03
  3.29850683e-03  2.55715139e-03  1.92928748e-03  1.40629337e-03
  9.79925362e-04  6.42214866e-04  3.85347603e-04  2.01504085e-04
  8.26116380e-05  1.98491161e-05]
H/W: [ 1.02  1.02  1.02  1.02  1.02  1.02  1.02  1.02  1.02  1.02  1.02  1.02  1.02
  1.02  1.02  1.02  2.  2.  2.  2.  2.  2.  2.  2.  2.
  1.02  1.02  1.02  2.  2.  2.  2.  2.  2.  2.  2.  2.  2.
  2.  2.  2.  2.  2.  2.  2.  2.  2.  2.  2.  2.
  2.  2.  2.  2.  ]
2wE/W: [ 0.46  0.48  0.5  0.52  0.54  0.56  0.58  0.6  0.62  0.64  0.66  0.68
  0.7  0.72  0.74  0.76  0.78  0.8  0.82  0.84  0.86  0.88  0.9  0.92
  0.94  0.96  0.98  0.46  0.48  0.5  0.52  0.54  0.56  0.58  0.6  0.62
  0.64  0.66  0.68  0.7  0.72  0.74  0.76  0.78  0.8  0.82  0.84  0.86
  0.88  0.9  0.92  0.94  0.96  0.98]
```

```
error < +-0.5%: [  4.95421687e-03  4.24086520e-03  3.62552072e-03  3.09883913e-03
  2.65117058e-03  2.27196010e-03  1.94846970e-03  1.66230242e-03
  1.37515620e-03  1.16244923e-03  3.29850683e-03  2.55715139e-03
  1.92928748e-03  1.40629337e-03  9.79925362e-04  6.42214866e-04
  3.85347603e-04  2.01504085e-04  8.26116380e-05  1.98491161e-05]
H/W: [ 1.02  1.02  1.02  1.02  1.02  1.02  1.02  1.02  1.02  1.02  2.  2.  2.
  2.
  2.  2.  2.  2.  2.  2.  2.  ]
2wE/W: [ 0.82  0.84  0.86  0.88  0.9  0.92  0.94  0.96  0.98  0.78  0.8  0.82
  0.84  0.86  0.88  0.9  0.92  0.94  0.96  0.98]
```

H/W: tall, 2wE/W: small

```
-----
error < +-5.0%: [  1.34379841e-03  1.50625142e-03  1.55492737e-03  1.51063107e-03
  1.37568637e-03  1.14727975e-03  8.20469773e-04  3.89165578e-04
 -1.53497014e-04 -8.15004047e-04 -1.60341016e-03 -2.52733424e-03
 -3.59598269e-03 -4.81919075e-03 -6.20747734e-03 -7.77211171e-03
 -9.52519160e-03 -1.14797334e-02 -1.36497758e-02 -1.60504988e-02
 -1.86983601e-02 -2.16112531e-02 -2.48086897e-02 -2.83120129e-02
 -3.21446459e-02 -3.63323863e-02 -4.09037545e-02 -4.58904100e-02
```

```

-1.40953695e-05 -7.59012833e-05 -1.94053115e-04 -3.77200484e-04
-6.33290716e-04 -9.69995216e-04 -1.39493189e-03 -1.91580639e-03
-2.54051530e-03 -3.27723003e-03 -4.13447098e-03 -5.12117737e-03
-6.24677632e-03 -7.52125377e-03 -8.95522915e-03 -1.05600358e-02
-1.23478090e-02 -1.43315832e-02 -1.65254008e-02 -1.89444353e-02
-2.16051310e-02 -2.45253626e-02 -2.77246203e-02 -3.12242233e-02
-3.50475704e-02 -3.92204342e-02 -4.37713099e-02 -4.87318322e-02]
H/W: [ 1.02 1.02 1.02 1.02 1.02 1.02 1.02 1.02 1.02 1.02 1.02 1.02 1.02 1.02
1.02 1.02 1.02 1.02 2. 2. 2. 2. 2. 2. 2. 2.
2. 2. 2. 2. 2. 2. 2. 2. 2. 2. 2. 2.
2. 2. 2. 2. 2. 2. ]
2wE/W: [ 0.02 0.04 0.06 0.08 0.1 0.12 0.14 0.16 0.18 0.2 0.22 0.24
0.26 0.28 0.3 0.32 0.34 0.36 0.38 0.4 0.42 0.44 0.46 0.48
0.5 0.52 0.54 0.56 0.02 0.04 0.06 0.08 0.1 0.12 0.14 0.16
0.18 0.2 0.22 0.24 0.26 0.28 0.3 0.32 0.34 0.36 0.38 0.4
0.42 0.44 0.46 0.48 0.5 0.52 0.54 0.56]

error < +-0.5%: [ 1.34379841e-03 1.50625142e-03 1.55492737e-03 1.51063107e-03
1.37568637e-03 1.14727975e-03 8.20469773e-04 3.89165578e-04
-1.53497014e-04 -8.15004047e-04 -1.60341016e-03 -2.52733424e-03
-3.59598269e-03 -4.81919075e-03 -1.40953695e-05 -7.59012833e-05
-1.94053115e-04 -3.77200484e-04 -6.33290716e-04 -9.69995216e-04
-1.39493189e-03 -1.91580639e-03 -2.54051530e-03 -3.27723003e-03
-4.13447098e-03]
H/W: [ 1.02 1.02 1.02 1.02 1.02 1.02 1.02 1.02 1.02 1.02 1.02 1.02 1.02
1.02 1.02 2. 2. 2. 2. 2. 2. 2. 2. 2. 2.
]
2wE/W: [ 0.02 0.04 0.06 0.08 0.1 0.12 0.14 0.16 0.18 0.2 0.22 0.24
0.26 0.28 0.02 0.04 0.06 0.08 0.1 0.12 0.14 0.16 0.18 0.2
0.22]

H/W: shallow, 2wE/W: large
-----
error < +-5.0%: [ 0.04266411 0.02856579 0.01599183 0.00475681 -0.00529221 -0.01428284
-0.02232264 -0.02950306 -0.03590251 -0.04158867 -0.04662042 -0.04894622
-0.04434866 -0.0380939 ]
H/W: [ 1. 1. 1. 1. 1. 1. 1. 1. 1. 1. 1. 1. 1. ]
2wE/W: [ 0.28 0.3 0.32 0.34 0.36 0.38 0.4 0.42 0.44 0.46 0.48 0.94
0.96 0.98]

error < +-0.5%: [ 0.00475681]
H/W: [ 1.]
2wE/W: [ 0.34]

H/W: shallow, 2wE/W: small
-----
error < +-5.0%: [ 8.64649787e-04 -1.25293460e-04 -9.18026175e-07 -9.93122166e-08
5.31949640e-09 3.78638454e-10 -1.31092914e-11 -2.44138043e-13
1.04360964e-14 -4.44089210e-16 -2.22044605e-16 -1.11022302e-16
-1.11022302e-16 -2.22044605e-16 -2.22044605e-16 -2.22044605e-16
-1.11022302e-16 -2.22044605e-16 -4.44089210e-16 -2.22044605e-16
-4.44089210e-16 -3.33066907e-16 -2.22044605e-16 -2.22044605e-16
-2.22044605e-16 0.00000000e+00 0.00000000e+00 -1.11022302e-16
-1.11022302e-16 -2.22044605e-16 -2.22044605e-16 0.00000000e+00
0.00000000e+00 -4.44089210e-16 -2.22044605e-16 -2.22044605e-16
-5.55111512e-16 -4.44089210e-16 -8.88178420e-16 -9.43689571e-15
-2.18935980e-13 -5.68267655e-12 -1.50597090e-10 -4.07730671e-09
-1.13676139e-07 -3.30817977e-06 -1.03186156e-04 -3.71923792e-03
-1.71721015e-02 -2.00078218e-02 -2.21800755e-02 -2.40671766e-02
-2.58058493e-02 -2.74645520e-02 -2.90842462e-02 -3.06925754e-02
-3.23099728e-02 -3.39526894e-02 -3.56344602e-02 -3.73674984e-02

```

```

-3.91631346e-02 -4.10322529e-02 -4.29856120e-02 -4.50340938e-02
-4.71889128e-02 -4.94618008e-02]
H/W: [ 0.02 0.02 0.02 0.02 0.02 0.02 0.02 0.02 0.02 0.02 0.02 0.02 0.02 0.02
0.02 0.02 0.02 0.02 0.02 0.02 0.02 0.02 0.02 0.02 0.02 0.02 0.02
0.02 0.02 0.02 0.02 0.02 0.02 0.02 0.02 0.02 0.02 0.02 0.02 0.02
1. 1. 1. 1. 1. 1. 1. 1. 1. 1. 1. 1. 1. 1.
1. 1. 1. 1. 1. ]
2wE/W: [ 0.04 0.06 0.08 0.1 0.12 0.14 0.16 0.18 0.2 0.22 0.24 0.26
0.28 0.3 0.32 0.34 0.36 0.38 0.4 0.42 0.44 0.46 0.48 0.5
0.52 0.54 0.56 0.58 0.6 0.62 0.64 0.66 0.68 0.7 0.72 0.74
0.76 0.78 0.8 0.82 0.84 0.86 0.88 0.9 0.92 0.94 0.96 0.98
0.02 0.04 0.06 0.08 0.1 0.12 0.14 0.16 0.18 0.2 0.22 0.24
0.26 0.28 0.3 0.32 0.34 0.36]

error < +/-0.5%: [ 8.64649787e-04 -1.25293460e-04 -9.18026175e-07 -9.93122166e-08
5.31949640e-09 3.78638454e-10 -1.31092914e-11 -2.44138043e-13
1.04360964e-14 -4.44089210e-16 -2.22044605e-16 -1.11022302e-16
-1.11022302e-16 -2.22044605e-16 -2.22044605e-16 -2.22044605e-16
-1.11022302e-16 -2.22044605e-16 -4.44089210e-16 -2.22044605e-16
-4.44089210e-16 -3.33066907e-16 -2.22044605e-16 -2.22044605e-16
-2.22044605e-16 0.00000000e+00 0.00000000e+00 -1.11022302e-16
-1.11022302e-16 -2.22044605e-16 -2.22044605e-16 0.00000000e+00
0.00000000e+00 -4.44089210e-16 -2.22044605e-16 -2.22044605e-16
-5.55111512e-16 -4.44089210e-16 -8.88178420e-16 -9.43689571e-15
-2.18935980e-13 -5.68267655e-12 -1.50597090e-10 -4.07730671e-09
-1.13676139e-07 -3.30817977e-06 -1.03186156e-04 -3.71923792e-03]
H/W: [ 0.02 0.02 0.02 0.02 0.02 0.02 0.02 0.02 0.02 0.02 0.02 0.02 0.02 0.02
0.02 0.02 0.02 0.02 0.02 0.02 0.02 0.02 0.02 0.02 0.02 0.02
0.02 0.02 0.02 0.02 0.02 0.02 0.02 0.02 0.02 0.02 0.02 0.02
0.02 0.02 0.02 0.02 0.02 0.02 0.02 0.02 0.02 0.02 0.02 0.02]
2wE/W: [ 0.04 0.06 0.08 0.1 0.12 0.14 0.16 0.18 0.2 0.22 0.24 0.26
0.28 0.3 0.32 0.34 0.36 0.38 0.4 0.42 0.44 0.46 0.48 0.5
0.52 0.54 0.56 0.58 0.6 0.62 0.64 0.66 0.68 0.7 0.72 0.74
0.76 0.78 0.8 0.82 0.84 0.86 0.88 0.9 0.92 0.94 0.96 0.98]

```

Output of Figs. S4–S7

```

mpmath: 0.19
numpy: 1.11.0
matplotlib: 1.5.1

```

```
H/W: tall, 2wE/W: large
```

```

-----
0.95 <= first ratio <= 1.05: [ 1.04898787 1.02980031 1.01291437 1.04859517
1.02956362 1.01281356]
krho2: [ 0.3161621 0.22364877 0.11883769 0.314465 0.22236378 0.1181084 ]
H/W: [ 1.02 1.02 1.02 2. 2. 2. ]
2wE/W: [ 0.94 0.96 0.98 0.94 0.96 0.98]

```

```

0.95 <= total ratio <= 1.05: [ 1.04892463 1.04396355 1.03945139 1.03534661
1.03161263 1.02821708
1.02513115 1.02232915 1.01978798 1.01748688 1.01540704 1.01353138
1.01184432 1.01033159 1.00898005 1.00777753 1.0067127 1.00577495
1.00495422 1.00424087 1.00362552 1.00309884 1.00265117 1.00227196
1.00194847 1.0016623 1.00137516 1.04578823 1.04083473 1.03633373
1.03224375 1.02852826 1.02515496 1.02209509 1.019323 1.01681568
1.0145524 1.01251444 1.01068481 1.009048 1.00758987 1.00629742
1.00515864 1.00416245 1.00329851 1.00255715 1.00192929 1.00140629
1.00097993 1.00064221 1.00038535 1.0002015 1.00008261 1.00001985]

```

```

2nd ratio: [ 0.55532422 0.56798152 0.58098241 0.59433678 0.60805423 0.62214392
0.63661436 0.65147323 0.66672707 0.68238099 0.69843827 0.71489984
0.73176371 0.74902424 0.76667122 0.78468872 0.80305371 0.82173422
0.84068702 0.8598545 0.87916049 0.89850429 0.91775183 0.93672129
0.95515734 0.97267625 0.98860791 0.5552433 0.56788428 0.58086642
0.5941994 0.60789256 0.62195482 0.63639446 0.65121891 0.66643449
0.6820461 0.69805684 0.71446748 0.73127595 0.74847658 0.76605922
0.78400814 0.80230065 0.82090535 0.83977983 0.8588677 0.87809452
0.89736204 0.91653972 0.93545101 0.95384905 0.97136553 0.98736815]
1st ratio: [ 1.88885086 1.8380238 1.78912714 1.7420201 1.69657997 1.65269971
1.61028593 1.56925734 1.5295434 1.49108327 1.45382503 1.41772501
1.38274734 1.34886368 1.31605312 1.28430231 1.2536057 1.22396624
1.19539637 1.16791953 1.1415726 1.11640962 1.09250795 1.06997884
1.04898787 1.02980031 1.01291437 1.88347745 1.83282892 1.78411712
1.73720093 1.69195731 1.64827881 1.60607162 1.56525399 1.52575488
1.48751293 1.45047565 1.41459875 1.37984573 1.34618757 1.31360265
1.2820768 1.25160368 1.22218537 1.19383333 1.16656999 1.1404311
1.11546943 1.09176089 1.06941501 1.04859517 1.02956362 1.01281356]
H/W: [ 1.02 1.02 1.02 1.02 1.02 1.02 1.02 1.02 1.02 1.02 1.02 1.02 1.02
1.02 1.02 1.02 1.02 1.02 1.02 1.02 1.02 1.02 1.02 1.02
1.02 1.02 1.02 2. 2. 2. 2. 2. 2. 2. 2. 2.
2. 2. 2. 2. 2. 2. 2. 2. 2. 2. 2. 2.
2. 2. 2. 2. ]
2wE/W: [ 0.46 0.48 0.5 0.52 0.54 0.56 0.58 0.6 0.62 0.64 0.66 0.68
0.7 0.72 0.74 0.76 0.78 0.8 0.82 0.84 0.86 0.88 0.9 0.92
0.94 0.96 0.98 0.46 0.48 0.5 0.52 0.54 0.56 0.58 0.6 0.62
0.64 0.66 0.68 0.7 0.72 0.74 0.76 0.78 0.8 0.82 0.84 0.86
0.88 0.9 0.92 0.94 0.96 0.98]

```

H/W: tall, 2wE/W: small

```

-----
0.95 <= first ratio <= 1.05: [ 1. 0.99999997 0.99999984 0.99999945
0.99999856 0.99999682
0.99999377 0.99998879 0.99998112 0.99996982 0.99995371 0.99993141
0.99990124 0.9998612 0.99980894 0.99974169 0.99965618 0.99954858
0.99941442 0.99924843 0.9990445 0.99879542 0.99849279 0.99812674
0.99768568 0.99715596 0.99652151 0.99576329 0.99485873 0.99378095
0.99249779 0.99097061 0.98915275 0.98698747 0.98440536 0.98132079
0.97762719 0.97319051 0.96784009 0.96135552 0.95344712 1.
0.99999997 0.99999984 0.99999943 0.99999852 0.99999673 0.99999359
0.99998847 0.99998059 0.99996897 0.99995243 0.99992953 0.99989855
0.99985746 0.99980386 0.99973491 0.99964728 0.99953707 0.99939973
0.99922992 0.99902141 0.99876692 0.99845791 0.9980844 0.99763467
0.99709493 0.99644896 0.99567758 0.99475802 0.99366324 0.99236088
0.99081212 0.98897008 0.98677784 0.98416578 0.98104806 0.97731795
0.97284125 0.96744723 0.96091545 0.95295639]
krho'2: [ 5.93150903e-08 9.50015949e-07 4.81769284e-06 1.52628329e-05
3.73778983e-05 7.77998860e-05 1.44779035e-04 2.48264551e-04
4.00008451e-04 6.13688859e-04 9.05054360e-04 1.29209132e-03
1.79521639e-03 2.43749675e-03 3.24490122e-03 4.24658553e-03
5.47521597e-03 6.96733582e-03 8.76378018e-03 1.09101450e-02
1.34573176e-02 1.64620771e-02 1.99877732e-02 2.41050955e-02
2.88929450e-02 3.44394228e-02 4.08429521e-02 4.82135546e-02
5.66743026e-02 6.63629743e-02 7.74339430e-02 9.00603363e-02
1.04436509e-01 1.20780878e-01 1.39339179e-01 1.60388219e-01
1.84240192e-01 2.11247677e-01 2.41809420e-01 2.76377038e-01
3.15462813e-01 6.08973189e-01 9.75319587e-01 4.94569082e-01
1.56669182e-01 3.83630096e-01 7.98389784e-01 1.48548687e-01
2.54679487e-01 4.10254733e-01 6.29255486e-01 9.27762981e-01
1.32412372e-01 1.83913939e-01 2.49628411e-01 3.32195205e-01
4.34573868e-01 5.60075980e-01 7.12401264e-01 8.95678452e-01
1.11451149e-01 1.37403177e-01 1.67995724e-01 2.03865922e-01

```

2.45723809e-02 2.94360901e-02 3.50659916e-02 4.15605805e-02
 4.90298300e-02 5.75966177e-02 6.73983523e-02 7.85888289e-02
 9.13403493e-02 1.05846149e-01 1.22323180e-01 1.41015308e-01
 1.62196985e-01 1.86177497e-01 2.13305850e-01 2.43976445e-01
 2.78635646e-01 3.17789420e-01]

H/W: [1.02 1.02 1.02 1.02 1.02 1.02 1.02 1.02 1.02 1.02 1.02 1.02 1.02
 1.02 1.02 1.02 1.02 1.02 1.02 1.02 1.02 1.02 1.02 1.02 1.02
 1.02 1.02 1.02 1.02 1.02 1.02 1.02 1.02 1.02 1.02 1.02 1.02
 1.02 1.02 1.02 1.02 1.02 1.02 1.02 1.02 1.02 1.02 1.02 1.02
 2. 2. 2. 2. 2. 2. 2. 2. 2. 2. 2. 2. 2.
 2. 2. 2. 2. 2. 2. 2. 2. 2. 2. 2. 2. 2.
 2. 2. 2. 2. 2. 2. 2. 2. 2. 2. 2. 2. 2.
 2. 2. 2. 2. 2. 2. 2. 2. 2. 2. 2. 2. 2.]

2wE/W: [0.02 0.04 0.06 0.08 0.1 0.12 0.14 0.16 0.18 0.2 0.22 0.24
 0.26 0.28 0.3 0.32 0.34 0.36 0.38 0.4 0.42 0.44 0.46 0.48
 0.5 0.52 0.54 0.56 0.58 0.6 0.62 0.64 0.66 0.68 0.7 0.72
 0.74 0.76 0.78 0.8 0.82 0.02 0.04 0.06 0.08 0.1 0.12 0.14
 0.16 0.18 0.2 0.22 0.24 0.26 0.28 0.3 0.32 0.34 0.36 0.38
 0.4 0.42 0.44 0.46 0.48 0.5 0.52 0.54 0.56 0.58 0.6 0.62
 0.64 0.66 0.68 0.7 0.72 0.74 0.76 0.78 0.8 0.82]

0.95 <= total ratio <= 1.05: [1.0013438 1.00150625 1.00155493 1.00151063
 1.00137569 1.00114728
 1.00082047 1.00038917 0.9998465 0.999185 0.99839659 0.99747267
 0.99640402 0.99518081 0.99379252 0.99222789 0.99047481 0.98852027
 0.98635022 0.9839495 0.98130164 0.97838875 0.97519131 0.97168799
 0.96785535 0.96366761 0.95909625 0.95410959 0.9999859 0.9999241
 0.99980595 0.9996228 0.99936671 0.99903 0.99860507 0.99808419
 0.99745948 0.99672277 0.99586553 0.99487882 0.99375322 0.99247875
 0.99104477 0.98943996 0.98765219 0.98566842 0.9834746 0.98105556
 0.97839487 0.97547464 0.97227538 0.96877578 0.96495243 0.96077957
 0.95622869 0.95126817]

2nd ratio: [1.0013438 1.00150628 1.00155509 1.00151118 1.00137713 1.00115046
 1.00082671 1.00040038 0.99986538 0.99921516 0.9984428 0.99754109
 0.99650243 0.99531896 0.99398243 0.99248425 0.99081547 0.9889667
 0.98692815 0.98468956 0.98224017 0.97956871 0.97666334 0.97351163
 0.97010048 0.96641614 0.9624441 0.95816907 0.99998591 0.99992413
 0.99980611 0.99962337 0.99936819 0.99903327 0.99861147 0.9980957
 0.99747884 0.99675369 0.9959129 0.99494894 0.99385405 0.99262023
 0.99123919 0.98970233 0.98800068 0.98612492 0.9840653 0.98181164
 0.97935325 0.97667896 0.97377703 0.97063513 0.96724028 0.96357883
 0.95963639 0.9553978]

1st ratio: [1. 0.99999997 0.99999984 0.99999945 0.99999856 0.99999682
 0.99999377 0.99998879 0.99998112 0.99996982 0.99995371 0.99993141
 0.99990124 0.9998612 0.99980894 0.99974169 0.99965618 0.99954858
 0.99941442 0.99924843 0.9990445 0.99879542 0.99849279 0.99812674
 0.99768568 0.99715596 0.99652151 0.99576329 1. 0.99999997
 0.99999984 0.99999943 0.99999852 0.99999673 0.99999359 0.99998847
 0.99998059 0.99996897 0.99995243 0.99992953 0.99989855 0.99985746
 0.99980386 0.99973491 0.99964728 0.99953707 0.99939973 0.99922992
 0.99902141 0.99876692 0.99845791 0.9980844 0.99763467 0.99709493
 0.99644896 0.99567758]

H/W: [1.02 1.02 1.02 1.02 1.02 1.02 1.02 1.02 1.02 1.02 1.02 1.02 1.02
 1.02 1.02 1.02 1.02 1.02 1.02 1.02 1.02 1.02 1.02 1.02 1.02
 1.02 1.02 1.02 1.02 2. 2. 2. 2. 2. 2. 2. 2. 2.
 2. 2. 2. 2. 2. 2. 2. 2. 2. 2. 2. 2. 2.
 2. 2. 2. 2. 2. 2. 2. 2. 2. 2. 2. 2. 2.]

2wE/W: [0.02 0.04 0.06 0.08 0.1 0.12 0.14 0.16 0.18 0.2 0.22 0.24
 0.26 0.28 0.3 0.32 0.34 0.36 0.38 0.4 0.42 0.44 0.46 0.48
 0.5 0.52 0.54 0.56 0.02 0.04 0.06 0.08 0.1 0.12 0.14 0.16
 0.18 0.2 0.22 0.24 0.26 0.28 0.3 0.32 0.34 0.36 0.38 0.4
 0.42 0.44 0.46 0.48 0.5 0.52 0.54 0.56]

H/W: shallow, 2wE/W: large

0.95 <= first ratio <= 1.05: [1.04904071 1.02983215 1.01292793]

krho2: [0.31638993 0.22382135 0.11893569]

H/W: [1. 1. 1.]

2wE/W: [0.94 0.96 0.98]

0.95 <= total ratio <= 1.05: [1.04266411 1.02856579 1.01599183 1.00475681

0.99470779 0.98571716

0.97767736 0.97049694 0.96409749 0.95841133 0.95337958 0.95105378
0.95565134 0.9619061]

2nd ratio: [0.42181475 0.43000682 0.43849611 0.44729365 0.45641079 0.46585922

0.47565095 0.48579829 0.49631383 0.50721041 0.5185011 0.90659377
0.92796805 0.94962936]

1st ratio: [2.47185312 2.39197553 2.31699165 2.24630243 2.17941339 2.11591207

2.05545128 1.99773643 1.94251589 1.88957344 1.8387224 1.04904071
1.02983215 1.01292793]

H/W: [1. 1. 1. 1. 1. 1. 1. 1. 1. 1. 1. 1.]

2wE/W: [0.28 0.3 0.32 0.34 0.36 0.38 0.4 0.42 0.44 0.46 0.48 0.94
0.96 0.98]

H/W: shallow, 2wE/W: small

0.95 <= first ratio <= 1.05: [1.00086465 0.99987471 0.99999908 0.9999999

1.00000001 1. 1.

1. 1. 1. 1. 1. 1. 1.
1. 1. 1. 1. 1. 1. 1.
1. 1. 1. 1. 1. 1. 1.
1. 1. 1. 1. 1. 1. 1.
1. 1. 0.99999989 0.99999669 0.99989681 0.99628076

1. 0.99999997 0.99999984 0.99999945 0.99999856 0.99999683
0.99999379 0.99998883 0.99998119 0.99996993 0.99995388 0.99993166
0.99990159 0.9998617 0.99980962 0.99974259 0.99965736 0.99955011
0.99941636 0.99925089 0.99904756 0.9987992 0.99849742 0.99813236
0.99769245 0.99716406 0.99653114 0.99577468 0.99487212 0.9937966
0.992516 0.9909917 0.98917706 0.98701538 0.98443727 0.98135713
0.97766841 0.97323708 0.96789251 0.96141426 0.95351265]

krho '2: [2.71140512e-66 7.22163073e-65 1.71965216e-63 4.00303667e-62

9.27470780e-61 2.14678050e-59 4.96806284e-58 1.14965685e-56
2.66039170e-55 6.15633361e-54 1.42461838e-52 3.29666567e-51
7.62871273e-50 1.76533697e-48 4.08511201e-47 9.45323215e-46
2.18754340e-44 5.06212693e-43 1.17141123e-41 2.71072673e-40
6.27280941e-39 1.45157155e-37 3.35903710e-36 7.77304450e-35
1.79873634e-33 4.16240047e-32 9.63208298e-31 2.22893072e-29
5.15790006e-28 1.19357380e-26 2.76201244e-25 6.39148810e-24
1.47903462e-22 3.42258854e-21 7.92010695e-20 1.83276761e-18
4.24115118e-17 9.81431759e-16 2.27110107e-14 5.25548518e-13
1.21615567e-11 2.81426846e-10 6.51241214e-09 1.50701728e-07
3.48734236e-06 8.06995176e-05 1.86744273e-03 4.32139183e-02
5.91055407e-08 9.46664673e-07 4.80073984e-06 1.52093102e-05
3.72474076e-05 7.75297599e-05 1.44279607e-04 2.47414567e-04
3.98650641e-04 6.11625725e-04 9.02044199e-04 1.28784453e-03
1.78939212e-03 2.42969993e-03 3.23468005e-03 4.23342948e-03
5.45855441e-03 6.94653734e-03 8.73815269e-03 1.08789368e-02
1.34197196e-02 1.64172259e-02 1.99347562e-02 2.40429572e-02
2.88206955e-02 3.43560481e-02 4.07474272e-02 4.81048598e-02
5.65514426e-02 6.62250015e-02 7.72799856e-02 8.98896312e-02
1.04248441e-01 1.20575027e-01 1.39115374e-01 1.60146601e-01
1.83981292e-01 2.10972506e-01 2.41519569e-01 2.76074802e-01
3.15151338e-01]

H/W: [0.02 0.02 0.02 0.02 0.02 0.02 0.02 0.02 0.02 0.02 0.02 0.02 0.02

```

0.02 0.02 0.02 0.02 0.02 0.02 0.02 0.02 0.02 0.02 0.02 0.02
0.02 0.02 0.02 0.02 0.02 0.02 0.02 0.02 0.02 0.02 0.02 0.02
0.02 0.02 0.02 0.02 0.02 0.02 0.02 0.02 0.02 0.02 0.02 0.02
1. 1. 1. 1. 1. 1. 1. 1. 1. 1. 1. 1. 1.
1. 1. 1. 1. 1. 1. 1. 1. 1. 1. 1. 1. 1.
1. 1. 1. 1. 1. 1. 1. 1. 1. 1. 1. 1. 1.
1. 1. ]
2wE/W: [ 0.04 0.06 0.08 0.1 0.12 0.14 0.16 0.18 0.2 0.22 0.24 0.26
0.28 0.3 0.32 0.34 0.36 0.38 0.4 0.42 0.44 0.46 0.48 0.5
0.52 0.54 0.56 0.58 0.6 0.62 0.64 0.66 0.68 0.7 0.72 0.74
0.76 0.78 0.8 0.82 0.84 0.86 0.88 0.9 0.92 0.94 0.96 0.98
0.02 0.04 0.06 0.08 0.1 0.12 0.14 0.16 0.18 0.2 0.22 0.24
0.26 0.28 0.3 0.32 0.34 0.36 0.38 0.4 0.42 0.44 0.46 0.48
0.5 0.52 0.54 0.56 0.58 0.6 0.62 0.64 0.66 0.68 0.7 0.72
0.74 0.76 0.78 0.8 0.82]

0.95 <= total ratio <= 1.05: [ 1.00086465 0.99987471 0.99999908 0.9999999
1.00000001 1. 1.
1. 1. 1. 1. 1. 1. 1.
1. 1. 1. 1. 1. 1. 1.
1. 1. 1. 1. 1. 1. 1.
1. 1. 1. 1. 1. 1. 1.
1. 1. 0.99999989 0.99999669 0.99989681 0.99628076
0.9828279 0.97999218 0.97781992 0.97593282 0.97419415 0.97253545
0.97091575 0.96930742 0.96769003 0.96604731 0.96436554 0.9626325
0.96083687 0.95896775 0.95701439 0.95496591 0.95281109 0.9505382 ]
2nd ratio: [ 1. 1. 1. 1. 1. 1. 1.
1.
1. 1. 1. 1. 1. 1. 1.
1. 1. 1. 1. 1. 1. 1.
1. 1. 1. 1. 1. 1. 1.
1. 1. 1. 1. 1. 1. 1.
1. 1. 1. 1. 1. 1. 0.9828279
0.97999221 0.97782008 0.97593336 0.97419555 0.97253853 0.97092178
0.96931825 0.96770823 0.96607636 0.96441002 0.96269829 0.96093143
0.95910039 0.95719662 0.95521179 0.95313767 0.95096603]
1st ratio: [ 1.00086465 0.99987471 0.99999908 0.9999999 1.00000001 1.
1.
1. 1. 1. 1. 1. 1. 1.
1. 1. 1. 1. 1. 1. 1.
1. 1. 1. 1. 1. 1. 1.
1. 1. 1. 1. 1. 1. 1.
1. 1. 0.99999989 0.99999669 0.99989681 0.99628076
1. 0.99999997 0.99999984 0.99999945 0.99999856 0.99999683
0.99999379 0.99998883 0.99998119 0.99996993 0.99995388 0.99993166
0.99990159 0.9998617 0.99980962 0.99974259 0.99965736 0.99955011]
H/W: [ 0.02 0.02 0.02 0.02 0.02 0.02 0.02 0.02 0.02 0.02 0.02 0.02 0.02
0.02 0.02 0.02 0.02 0.02 0.02 0.02 0.02 0.02 0.02 0.02 0.02
0.02 0.02 0.02 0.02 0.02 0.02 0.02 0.02 0.02 0.02 0.02 0.02
1. 1. 1. 1. 1. 1. 1. 1. 1. 1. 1. 1. 1.
1. 1. 1. 1. 1. ]
2wE/W: [ 0.04 0.06 0.08 0.1 0.12 0.14 0.16 0.18 0.2 0.22 0.24 0.26
0.28 0.3 0.32 0.34 0.36 0.38 0.4 0.42 0.44 0.46 0.48 0.5
0.52 0.54 0.56 0.58 0.6 0.62 0.64 0.66 0.68 0.7 0.72 0.74
0.76 0.78 0.8 0.82 0.84 0.86 0.88 0.9 0.92 0.94 0.96 0.98
0.02 0.04 0.06 0.08 0.1 0.12 0.14 0.16 0.18 0.2 0.22 0.24
0.26 0.28 0.3 0.32 0.34 0.36]

```